Small-scale analysis for mechanical behavior of individual austenite in Fe-C steels

満, 廷慧

https://doi.org/10.15017/2534433

出版情報：Kyushu University, 2019, 博士（工学）, 課程博士
バージョン：
権利関係：

Small-scale analysis for mechanical behavior of individual austenite in Fe-C steels

DISSERTATION

Presented in Partial Fulfillment of the Requirements for the Degree Doctor of Philosophy in the Graduate School of Kyushu University

By
Tinghui Man

Department of Materials Physics and Chemistry
Graduate School of Engineering
Kyushu University

2019

ABSTRACT

A new method to evaluate a resistance in plastic deformation during nanoindentation is described to analyze the deformation modes including dislocation glide motion and martensitic transformation in Fe alloys. The slope a of load/ penetration depth versus penetration depth (P/h versus h) plot has been found as a suitable parameter to evaluate mechanical behaviors.

The P/h versus h plots of three typical microstructures (*i.e.* stable austenite, ferrite, and tempered martensite) in the Fe alloys (*i.e.* SUS 316, Fe-30Ni, IF, and Fe-0.4C) show that the values of the slope a increase proportionally as the nanohardness H_n. This result indicates that the slope a can correspond to a plastic deformation resistance associated with deformation mechanisms. The slope a in the stable Fe alloys holds almost constant during the loading segment after onset of plasticity, which indicates that single deformation mode like dislocation glide motion dominates the behavior during the plastic deformation. In addition, the effects of grain boundary for ferrite in the IF and stable austenite in the Fe-30Ni are investigated. The difference in the slope a values between the vicinity of grain boundary and grain interior is not remarkable in ferrite and stable austenite.

The nanoindentation behaviors of metastable austenite, stable austenite, and martensite are demonstrated in the Fe-Ni steels. The influential factor, austenite grain boundary (austenite grain size), on the mechanical stability is characterized. The P/h versus h plots suggest that slip deformation of dislocations exhibits for the stable austenite and martensite, while stress-induced martensitic transformation is detected in the metastable austenite. The indentation-transformed martensite in the austenite grains is confirmed by TEM observations in the region right beneath the indenter. The slope a changes during deformation, which suggests a change in the dominant deformation mode from martensitic transformation (stage I) to dislocation glide (stage II) in the metastable austenite. The slope a in the stage I corresponds to a mechanical stability of austenite. The load P_t at the transition from stage I to II can also evaluate the austenite

mechanical stability. Both the slope a in stage I and the transition load P_t increase in the vicinity of austenite grain boundary and the γ/α' interface compared with austenite grain interior. Furthermore, the transition load P_t increases with decreasing the distance from the austenite grain boundary. It suggests that the austenite grain boundary actively suppresses the stress-induced martensitic transformation, in which it is in concordance with the microstructural characterizations underneath indentation marks in the vicinity of grain boundary.

In addition, the deformation behavior of metastable retained austenite in the Fe-1.4C-12Cr steel is investigated to determine the effect of the austenite grain size on the mechanical stability. The results by nanoindentation have also demonstrated that martensite exhibits a single deformation stage during the plastic deformation, while metastable retained austenite shows double stages. TEM observations on an indentation mark inside the austenite grain suggest that stress-induced martensitic transformation occurred in stage I. Furthermore, both the slope a in stage I and the transition load P_t increase with decreasing the austenite grain size, which indicates that the fine grains are mechanically more stable than the coarse grains.

ACKNOWLEDGEMENT

First and foremost, I would like to express my deepest and sincere gratitude to my supervisor, Prof. Takahito Ohmura for his guidance, support and sharing his knowledge in this field. Thanks for his incredible patience and abundant discussion that allow me to survive after a long incubation time in my learning curve in this field.

I would also like to thank Prof. Yo Tomota and Dr. Dehai Ping. Many fruitful discussions and insightful comments with them contribute a lot to the work done in my thesis. I also want to thank Dr. Yanxu Wang, Dr. Jovana Ruzic and all members of High Strength Materials Group at NIMS, for sharing their experience in the labs and helping me with the instruments.

I would like to greatly appreciate the constructive comments, abundant discussion and thoughtful guidance provided by Prof. Masaki Tanaka and Prof. Toshihiro Tsuchiyama in improving my thesis. I am really grateful for their expert comments and excellent advice.

I would like to specially thank my friends Dr. Yang Yang, Yan Di, Dr. Xiaojiang Wang, Min Liu, Dr. Xin Ji, Dr. Jian Qiang, Xuan Liu, Lingjiang Meng, who have encouraged, supported and entertained me through the dark times and celebrated with me through the good.

Last but not least, I would like to express my gratitude to my parents for providing me with support, inspiration, and motivation that give me the strength to overcome all obstacles in my life.

Table of Contents

Chapter 1 Introduction

1.1 Background

The development of automotive industries brings the fact that global warming and natural resource depletion become the most critical environmental issues. Several studies indicate that vehicle traffic causes nearly 23% of carbon dioxide emissions. This amount will be likely increased to double by 2050 [1-2]. Besides, according to the International Energy Outlook report [3], natural fuel consumption will grow from 3% in 2012 to 11% in 2040. Therefore, lowering the rate of carbon dioxide emissions and fuel consumption is seen as the most significant trend and challenge for automotive industries. One of the most important ways to achieve this is by reducing the structural weight of vehicles. Therefore, lighter, safer, environmentally sustainable, and more fuel efficient vehicles are a priority for future automotive industries.

The steel for the requirements of the vehicle structures must satisfy some parameters regarding both heightened strength and excellent formability, however, a trade-off relationship exists between the two. The advanced high strength steels (AHSS) [4-10] have attracted considerable interest as the excellent formability, thereby reducing the overall weight of steel is used during manufacture. The AHSS family includes dual phase (DP) steels, transformation-induced plasticity (TRIP) steels, martensitic steels, *etc*. Figure 1.1 [11] shows the relative tensile strength and formability (measured by total elongation) of conventional high strength steels (HSS) and AHSS. TRIP steels provide the best balance between the strength and elongation concerns.

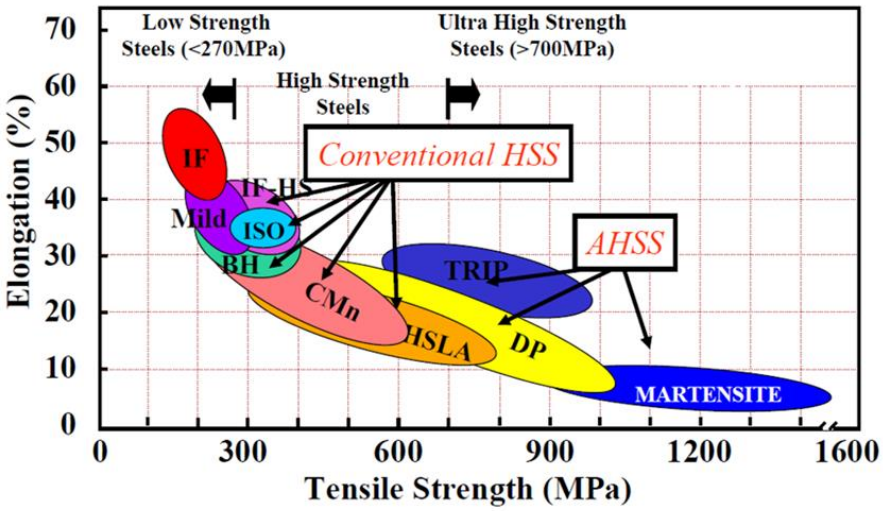

Figure 1.1 Tensile strength and total elongation combinations for various classes of conventional HSS and AHSS [11].

A schematic stress-strain curves for TRIP steels and conventional steels are shown in Fig. 1.2. The black curve describes the mechanical behavior of the conventional steels. The blue curve illustrates the mechanical behavior of the steels with TRIP effect. As can be seen, TRIP effect brings large additional elongation and strength when the retained austenite transformed into the martensite during the plastic deformation process, and thus postpones the onset of local necking.

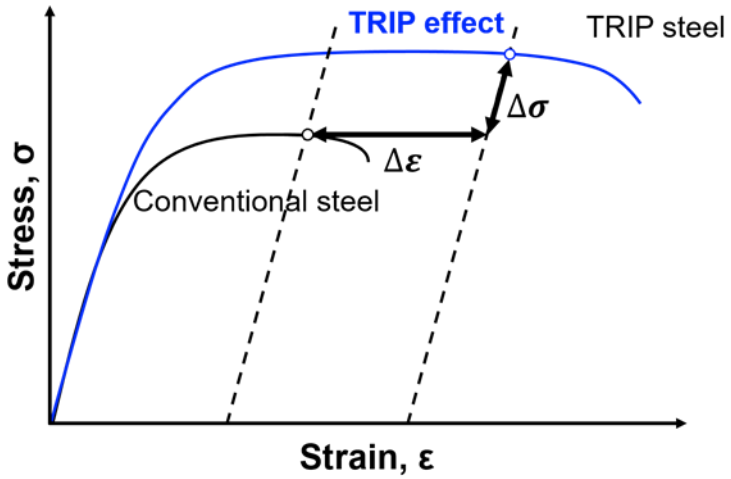

Figure 1.2 The typical stress-strain curves for the TRIP steels (blue curve) and the conventional steels (black curve).

For having the enhanced strength and excellent formability of steels in the lightweight automotive application, fundamental knowledge in mechanically-induced martensitic transformation is necessary to understand the mechanical mechanisms of the austenite phase in Fe-C steels. Furthermore, the previous studies on the factors affecting mechanical stability of the austenite phase are described.

1.2 Martensite and martensitic transformation

The word “martensite” that describes a very fine and sharp microstructure of hardened but untempered steels during the quenched process from a high temperature is named after Professor A. Martens, the famous German metallurgist [12]. Martensite holds the greatest technological importance in steels, in which it can provide the outstanding strength.

1.2.1 Morphology of martensite

Martensite exhibits various morphologies which can be divided into four types, for instance, lath martensite, butterfly martensite, lenticular martensite, and thin plate martensite [12-19]. In iron-based alloys, the morphologies of martensite are mainly determined by the chemical composition and martensitic transformation start temperature (M_s). Lath martensite usually forms in low carbon and/or nickel steels, as well as at the high M_s temperature range. In contrast to that, with increasing carbon and/or nickel content and decreasing the M_s temperature, the martensite morphology shifts to butterfly martensite, lenticular martensite and thin plate martensite. Figure 1.3 shows the four significant morphologies of martensite in the iron-based alloys [20-22]. These martensite are distinguished not only morphologically but also crystallographically [14, 15, 18]. Lath martensite in Fig. 1.3(a) exhibits a $\{1\ 1\ 1\}_{fcc}$ habit plane and contains a high density of dislocations. Butterfly martensite in Fig. 1.3(b), named from its appearance, exhibits a particular $\{2\ 2\ 5\}_{fcc}$ habit plane and

consists of twins and dislocations. Lenticular martensite in Fig. 1.3(c) exhibits a {2 5 9}$_{fcc}$ or {3 10 15}$_{fcc}$ habit plane and partially twinned with a midrib. Thin plate martensite in Fig. 1.3(d) exhibits a {3 10 15}$_{fcc}$ habit plane and is completely twinned without a midrib.

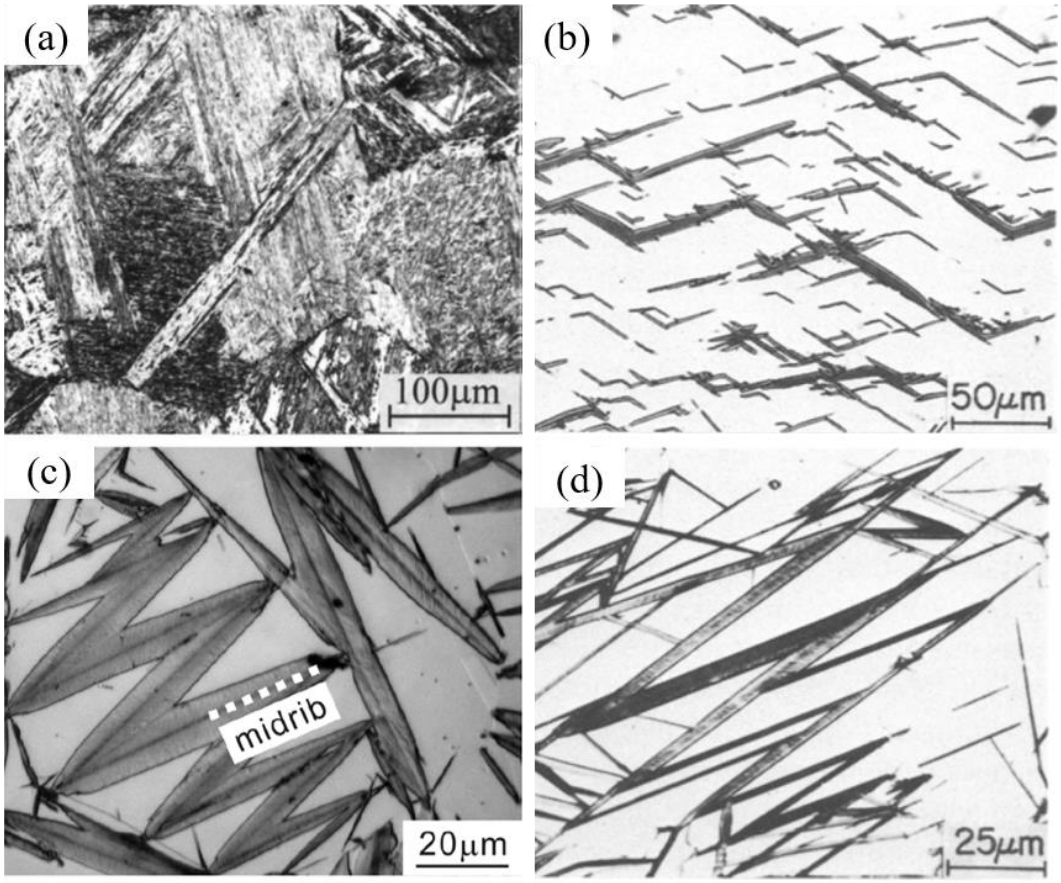

Figure 1.3 Optical micrographs of (a) lath martensite in Fe-0.18C alloy [20], (b) butterfly martensite in Fe-20Ni-0.73C alloy [21], (c) lenticular martensite in Fe-29Ni-0.2C alloy [22], and (d) thin plate martensite in Fe-31Ni-0.29C alloy [21].

1.2.2 Orientation relationships of martensitic transformation

The strengthening of steel through quenching has been used for thousands of years as a practical process. In recent hundreds of years, the result of a structural change is caused by the shear deformation of the martensite from the austenite, in which it is called martensitic transformation. A martensite reaction can be considered to be a first-order solid-state structural change, which is (a) displacive, (b) diffusionless, and (c)

dominated in kinetics and morphologies by the strain energy arising from the shear-like displacements. The series of three characteristics is considered as both necessary and sufficient to define a martensitic transformation.

The orientation relationships between austenite and martensite will have a very significant influence on the characteristics of the martensitic transformation. Bain proposed the simplest mechanism showing how a bcc lattice can be generated from fcc lattice by the compression of one lattice directions and the expansion of two other directions as shown in Fig. 1.4 [23]. The Bain orientation relationship serves as a first approximation or a reference point when martensitic transformation is investigated because it is never observed in iron-carbon and iron-nickel steels. Indeed, the Bain strain leaves no plane undistorted and unrotated, denoted as invariant planes. Thus, a lattice-invariant shear must accompany the Bain distortion. The phenomenological theory states that the martensitic transformation is accomplished by the Bain distortion and a shear deformation at the interface between austenite and martensite. The shear at the austenite/martensite (γ/α') interface occurs by either slip or twinning.

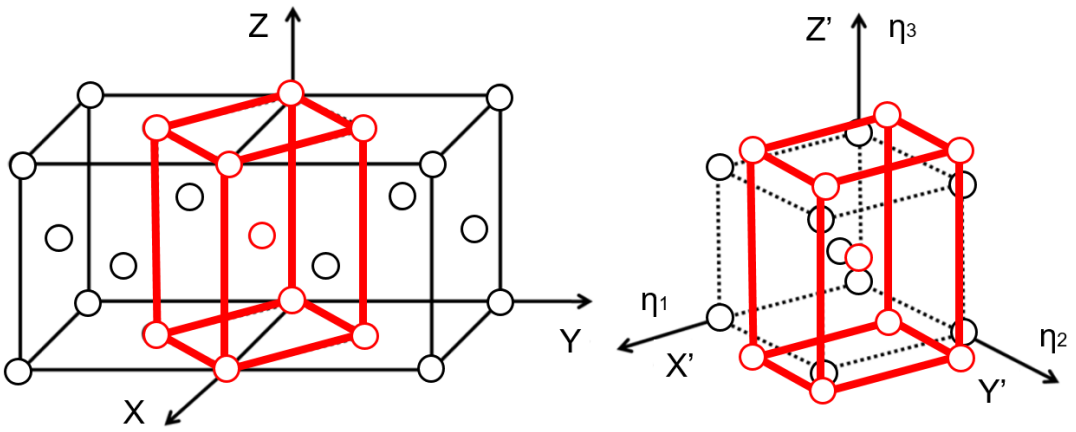

Figure 1.4 Lattice correspondence for Bain distortion, and the movement of crystal lattices along one compression and two expansion axes for the fcc to bcc transformation [23].

Four well-known orientation relationships which include Kurdjumov-Sachs (K-S) [24], Nishiyama-Wassermann (N-W) [25, 26], Greninger-Troiano (G-T) [27], and

Pitsch [28] relationships are typically used for martensite when the transformation of austenite into martensite was studied. Table 1.1 shows the four orientation relationships between the parent austenite phase and product martensitic structure. The number of variants for each orientation relationship is also given in Table 1.1. In the case of the K-S relationship, there are six variants with different direction parallel relationship on a conjugate parallel close-packed plane such as the (111) austenite plane. Thus, K-S relationship holds 24 variants as it has four crystallographically parallel planes in a given austenite grain. Furthermore, three variants evolve on a conjugate parallel close-packed plane for the case of N-W relationship.

Table 1.1 Four orientation relationships between parent austenite and product martensite [24-28].

Name	Orientation relationship	Number of variants
K-S	{111}γ// {110}α', <110>γ// <111>α'	24
N-W	{111}γ// {110}α', <112>γ// <110>α'	12
G-T	{111}γ~ 1° {110}α', <110>γ~ 2.5° <111>α'	24
Pitsch	{110}γ// {112}α', <100>γ// <110>α'	12

1.2.3 Stress- and strain-induced martensitic transformation

The martensitic transformation is responsible for the appearance of specific interactions when external stresses are applied. The martensitic shape change itself contributes a mode of deformation. Transformation induced plasticity (TRIP) is a phenomenon highlighted by Zackay et al. in 1976 [29], in which stress- and strain-induced martensitic transformation causes and promotes plastic deformation. It enhances both the strength and ductility of steels, therefore, the phenomenon is of great importance.

The martensitic transformation starts at the M_s temperature which is determined by the chemical composition [30-33] but also is induced with the aid of deformation at

higher temperatures. The applied stress will generate a positive contribution to the driving force for martensitic transformation, and thus elastic deformation will generate martensitic transformation at temperatures above M_s but below a proper temperature M_s^σ. This is called stress-induced martensitic transformation because the martensite nucleation is considered to start at the simply same sites, *i.e.* nucleation can occur at the grain boundary, aided mechanically by the thermodynamic contribution of the applied stress, which is lower than the austenite yield stress. Further, martensitic transformation can also take place above the proper temperature M_s^σ, and then it is defined as strain-induced martensitic transformation. Significant plastic flow precedes the martensitic transformation, and hence an additional contribution to martensitic transformation can arise from the production of new and more potent nucleating sites generated by the plastic deformation, such as twins, stacking faults and ε-martensite. The upper limit for the strain-induced martensitic transformation is M_d, and thus no martensite will form above this temperature. However, this temperature is hard to measure and hence another parameter, M_{d30}, is established by T. J. Angel [34], which is the temperature at which 50% of the martensite is produced at 30% true strain under tensile condition. The temperatures M_s and M_{d30} are given in Eq. 1.1 [32] and 1.2 [34] as follows:

$$M_s(℃) = 539 - 423C - 30.4Mn - 17.7Ni - 12.1Cr - 7.5Mo \quad (1.1)$$

$$M_{d30}(℃) = 413 - 13.7Cr - 9.5Ni - 8.1Mn - 18.5Mo - 9.2Si - 462(C + N) \quad (1.2)$$

The fractions of elements are in mass%, and the equations are stating that more alloying additives enhance the stability of the austenite.

The above-mentioned martensitic transformation mechanisms are distinguished by G. B. Olson and M. Cohen [35, 36]. Figure 1.5 is a schematic illustration of the interrelationships between stress-induced martensitic transformation and strain-induced martensitic transformation in Fe-Ni-C alloys. In Fig. 1.5, the types of martensitic transformation mechanisms are dependent on the imposed condition of

stress and resultant thermodynamics, and the sites of the martensite nucleation. For either of the two mechanisms to take place, the temperature must be above the M_s. The proper temperature M_s^σ lying above the M_s is defined below which the onset of martensite formation initiates yielding under applied stress, and above which

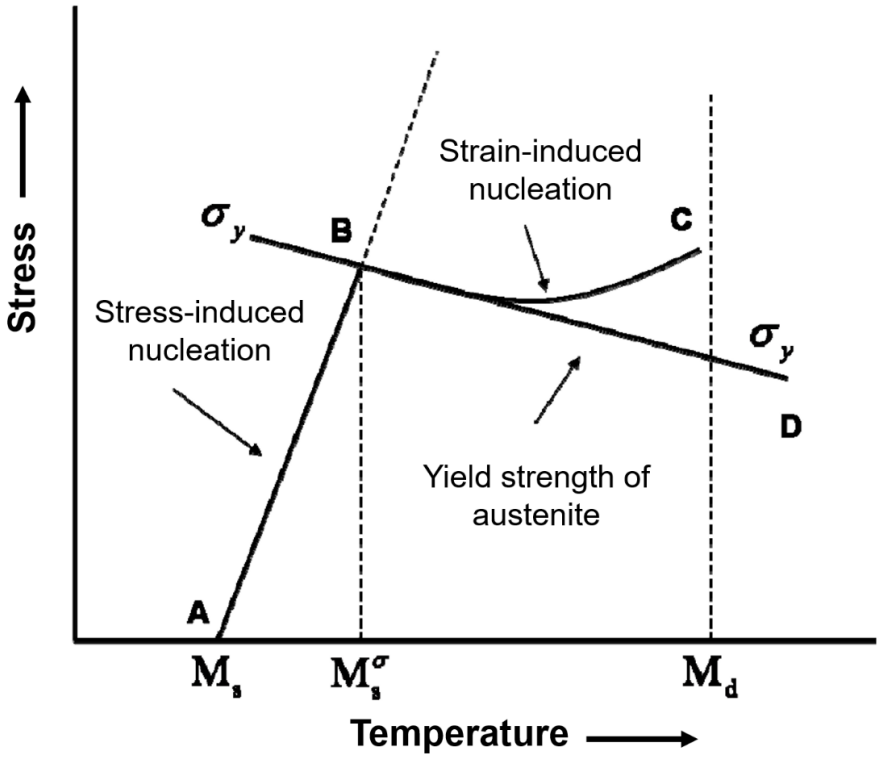

conventional slip processes in the parent phase initiate yielding under applied stress.

Figure 1.5 Schematic illustration of the interrelationships between stress-induced martensitic transformation (below M_s^σ) and strain-induced martensitic transformation (above M_s^σ) in Fe-Ni-C alloys [35].

1.3 Factors affecting austenite mechanical stability in TRIP-aided steels

As mentioned in the background section, a combination of excellent elongation and enhanced strength can be obtained by the TRIP effect. The essential constituent of the TRIP effect is the presence of the retained austenite phase, which is a metastable phase at room temperature. Therefore, the stability of the austenite phase is crucial to

the mechanical properties of steels. When the retained austenite phase is overstabilized, the TRIP effect is inhibited entirely, which makes no contribution to improve mechanical properties, by contrast, when the retained austenite phase is unstable, and the martensitic transformation early occurs at a low strain during the plastic deformation, resulting in small contribution to ductility of TRIP steels. The stability of the austenite phase is classified into thermal stability and mechanical stability. The former indicates the stability of the austenite phase against martensitic transformation during heat treatment, while the latter represents the stability of the austenite phase during deformation.

In general, the mechanical stability is affected by the chemical composition, the grain size of austenite, the morphology of austenite, the constraint effect by the phase surrounding austenite, and the crystallographic orientation of austenite. The chemical stabilization is that the concentration of elements stabilizes in the austenite phase, for instance, carbon, manganese, silicon, aluminum, chromium, and nickel [37-57]. Among them, carbon is the most crucial element affecting mechanical stability of the austenite phase [37-43]. The study reported by G. Reisner et al. [37] suggests that the austenite grains with low carbon content (<0.6 mass%) transformed into martensite at a shallow strain value. In this case, it is found that the total elongation of the steel is detrimentally affected by the early transformation as the martensitic transformation from the austenite phase occurs too early so that the hardening supplied by the TRIP effect is used up before failure begins when it is needed most. This suggests that higher carbon content in the austenite phase leads to higher mechanical stability. However, the opposite problem has also been reported in steels with the high carbon concentration of austenite phase. A further increase in the carbon content in the austenite phase leads to a decrease in the volume fraction of martensite, thereby increasing its stability too much [39, 40, 43]. It has been suggested that the volume fraction of retained austenite can be influenced by an optimum carbon content in the retained austenite phase. Therefore, it indicates that it exists optimal stability of the retained austenite phase depending on carbon concentration. The effect of the other alloying elements has also been widely

investigated, and the details are described in the following. Manganese is one of austenite stabilizing elements and also improves hardenability [44-46]. In Fe-0.3C-1.6Si mass% TRIP steels, increasing manganese content in the retained austenite leads to a decrease in the volume fraction of retained austenite, improving the mechanical stability [46]. Silicon is an effective element to suppress cementite precipitation [47-49]. As shown in the results [49] of the volume fraction of retained austenite for Fe-0.15C-1.4Mn mass% TRIP steel with different silicon content, the 0.24 mass% silicon sample contains small amount of retained austenite phase which suggests that austenite transforms completely to martensite at an early stage of straining. With increasing silicon content, the amount of retained austenite phase is increased, suggesting higher mechanical stability which means that higher strain is required for the martensitic transformation. When the silicon content is above 1.44 mass%, some retained austenite is still present and undergoing the transformation even after necking starts. Aluminum is also an element for improving the austenite stability similar to Si [50-55]. The replacement of Si by aluminum content leads to a much lower rate of transformation with strain, resulting in higher stability of the retained austenite phase [50]. Chromium plays an active role in improving austenite stability because it delays the pearlite transformation and carbide precipitation [56, 57]. The results obtained from Fe-1 mass% C steels with different chromium content [57] indicate that in a higher chromium sample (1.8-2.5 mass% Cr), a more gradual decrease in the austenite volume fraction occurred in response to compressive stress when compared to lower chromium samples. The higher chromium sample has larger barrier energy for transformation so greater compression is needed to trigger the martensite transformation. By increasing the compression, the volume fraction of retained austenite in the higher chromium sample decreases, but at a slower rate when compared to the lower chromium samples. Nickel is also an element of austenite stabilizer [58]. The amount of retained austenite is found almost to zero in the Fe-0.2C-1.4Mn-1.4Si mass% steel without nickel after the tensile deformation. Whereas, the 1 mass% nickel sample still remains about 4.3% of retained austenite. This confirms that the addition of nickel increases the stability of the retained austenite phase and makes it more difficult for the martensitic

transformation. Figure 1.6 is the mechanical stability of austenite dependent on elements mentioned above.

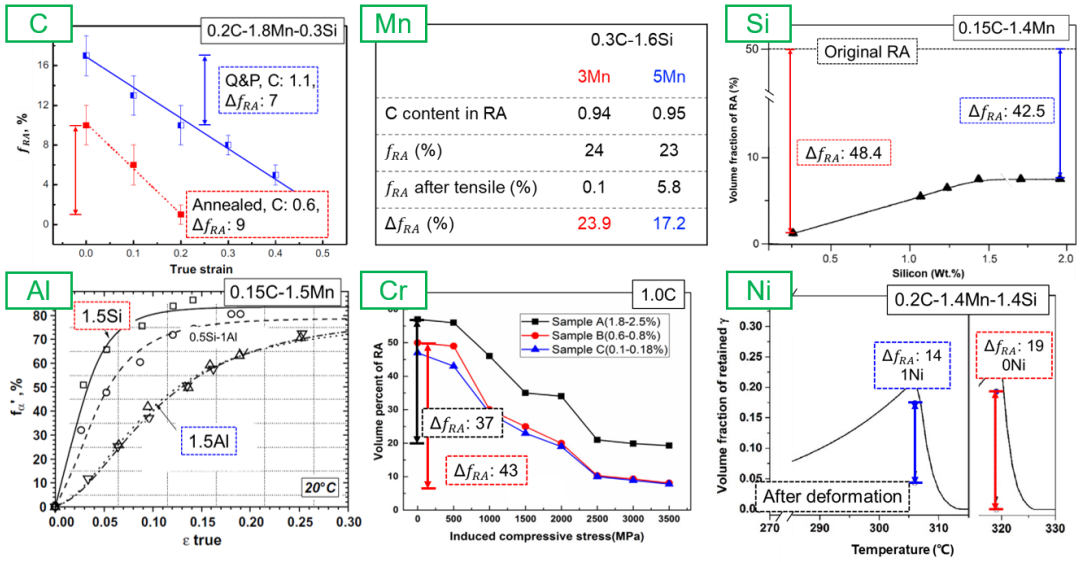

Figure 1.6 The mechanical stability of austenite dependent on elements, such as carbon [43], manganese [46], silicon [49], aluminum [50], chromium [57], and nickel [58].

The grain shape of retained austenite affects its mechanical stability. A study on the austenite grain morphology in Fe-0.17C-2.2Mn-1.6Al mass% steel that is reported by J. Chiang et al. [59] shows that the retained austenite in the equiaxed microstructure transforms faster with strain as shown in Fig. 1.7(a). By contrast, the retained austenite in the lamellar microstructure transforms more slowly and ceases to transform at about 80% transformation. In the optical microscope images (Fig. 1.7(b)), the equiaxed microstructure is generally “blocky”, and the lamellar microstructure is a mixture of “blocky” and “elongated”. The elongated shape of the retained grains like thin film in the lamellar microstructure results in high mechanical stability of retained austenite.

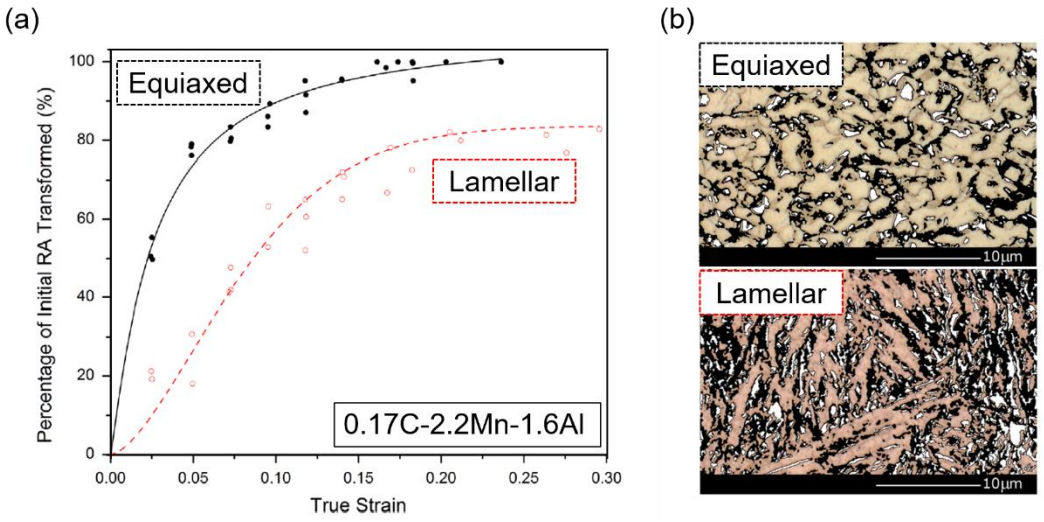

Figure 1.7 (a) The plots of the volume fraction of transformed retained austenite as function of true strain in Fe-0.17C-2.2Mn-1.6Al mass% steel and (b) the optical images of retained austenite in the equiaxed and lamellar microstructures [59].

Also, the retained austenite orientation with respect to the load direction affects the mechanical stability [37, 60-63]. Figure 1.8 shows the microstructures consisting of ferrite, transformed martensite and retained austenite in the Mn-Al type TRIP steel (Fe-0.2C-5.0Mn-0.5Si-1.5Al-0.05V mass%). The gray grains represent ferrite and transformed martensite, and the others are retained austenite. Figures 1.8(a), (d) show IPF maps of the retained austenite grains, (b), (e) represent Schmid factor distribution maps of retained austenite with the color scale of Schmid factor inserted in (e), and (c), (f) show the histogram of Schmid factor of retained austenite. (a), (b), (c) and (d), (e), (f) correspond to the true strains of 0.03 for 0.3, respectively [62]. The histograms show that most of retained austenite have Schmid factor around 0.43 at the true strain of 0.03, whereas, the Schmid factor shifts to smaller around 0.36 when the true strain increased to 0.3. It suggests that retained austenite grains with small Schmid factor exhibit high mechanical stability. That's to say, when the retained austenite exhibits an orientation which helps the retained austenite deform, it will lead to a larger driving force for martensitic transformation and in turn the earlier transformation.

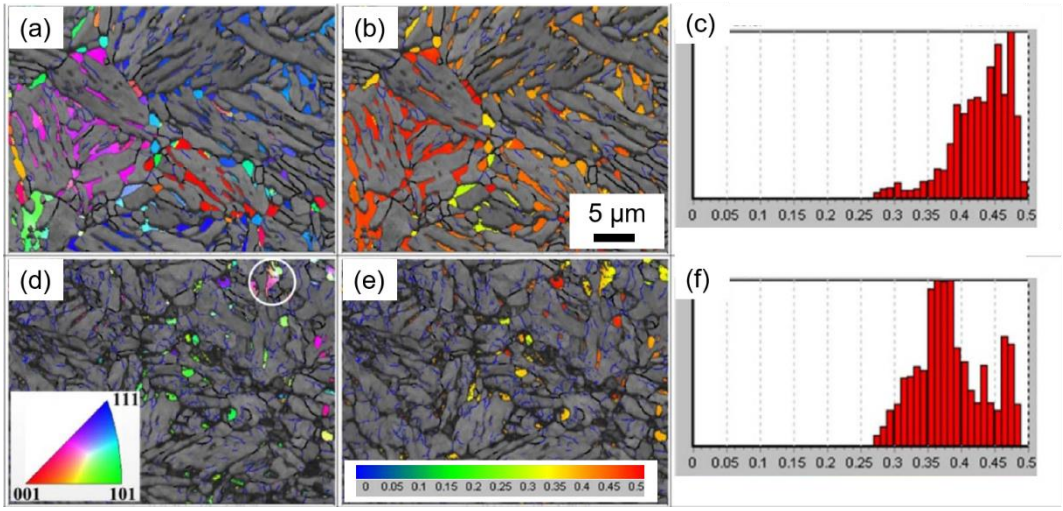

Figure 1.8 The microstructures consisting of ferrite, transformed martensite and retained austenite in the Mn-Al type TRIP steel (Fe-0.2C-5.0Mn-0.5Si-1.5Al-0.05V mass%). The gray grains represent ferrite and transformed martensite, and the others are retained austenite. (a) and (d) show IPF maps of the retained austenite grains, (b), (e) represent Schmid factor distribution maps of retained austenite with the color scale of Schmid factor inserted in (e), and (c), (f) show the histogram of Schmid factor of retained austenite. (a), (b), (c) and (d), (e), (f) correspond to the true strains of 0.03 for 0.3, respectively [62].

Furthermore, the mechanical stability against martensitic transformation is influenced by the neighboring phases around the retained austenite phase due to the load transfer [64-71]. On the microscale, the plastic deformation in multiphase TRIP steel is a complex process. Figure 1.9 is the volume fraction of retained austenite versus true strain plot for different surrounding phases in Fe-0.17C-1.41Si-2Mn mass% steel [70]. When the retained austenite located among the softer ferrite, the ferrite plastically deforms first, transferring the load to the retained austenite which bears more strain and stress, resulting in the transformation to martensite at the early stage of straining. Contrarily, when the retained austenite surrounded by the harder phase, such as martensite or bainite, which helps reduce strain and stress partitioned to the retained austenite, resulting in a lower transformation rate, thus, the martensitic transformation is delayed and mechanical stability is improved.

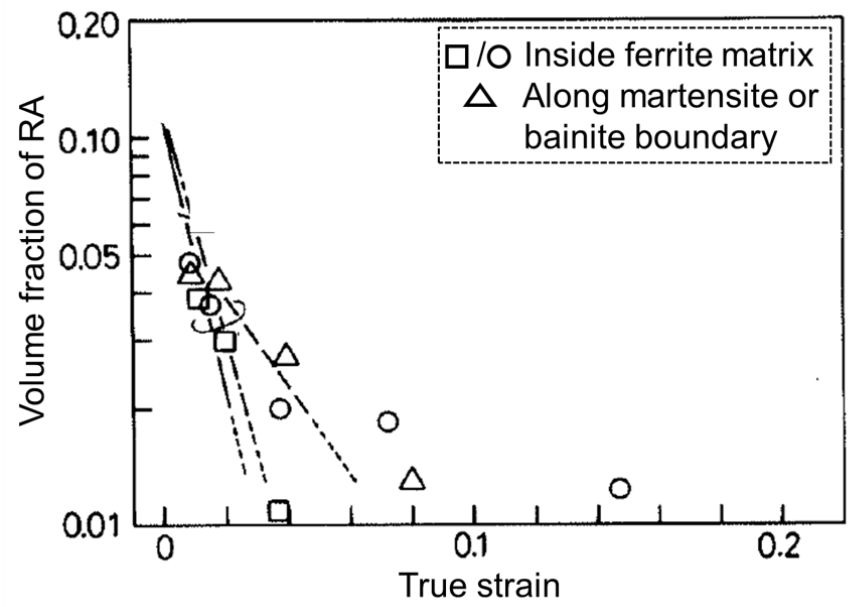

Figure 1.9 The volume fraction of retained austenite versus true strain plots for different surrounding phase in Fe-0.17C-1.41Si-2Mn mass% steel [70].

Also equally important, the grain size of retained austenite is particularly crucial in determining its mechanical stability [66, 72-74]. The plot of the transformation rate as a function of austenite grain size in Fe-0.25C-3Mn-1.5Si TRIP steel [72] have shown that the larger grains exhibit higher transformation rate, rapidly transformed to martensite at the early stage of plastic straining, whereas, smaller grains require larger macro-stresses to get the needed strain for austenite to martensite transformation. It suggests that the retained austenite grains with larger size hold the lower mechanical stability.

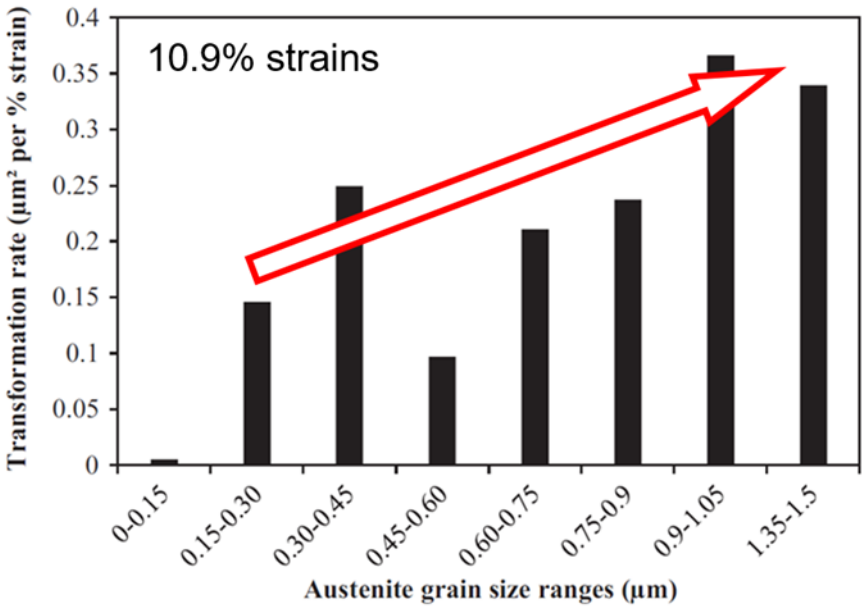

Figure 1.10 The transformation rate versus austenite grain size plot in Fe-0.25C-3Mn-1.5Si TRIP steel [72].

However, Matsuoka et al. [75] have reported that the mechanical stability under tensile deformation is not influenced by grain size. In the Fe-16Cr-10Ni mass% austenitic steel, the plot of the volume fraction of martensite as function of austenite grain size (Fig. 1.11) shows that the volume fraction of martensite is not changed for different grain size even though under different tensile deformation. In this study, some special variants are selected so that the anisotropic transformation strain can be released by the tensile strain in deformation-induced martensitic transformation, thus the suppression of martensitic transformation by grain refinement becomes invalid. This suggests that the mechanical stability of austenite independent on grain size.

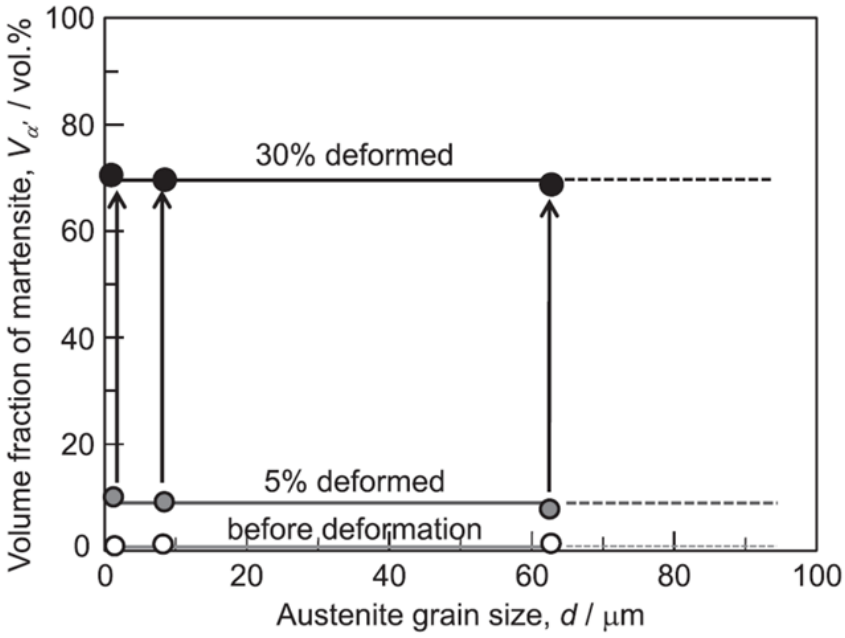

Figure 1.11 The plot of the volume fraction of martensite as function of austenite grain size [75].

There are a few studies on the mechanical stability of retained austenite, however, most of them deal with multiple factors, such as carbon content and grain size. In addition, the current state of knowledge regarding the individual effect of grain size of retained austenite on the mechanical stability has not been sufficiently understood, because the grain size of retained austenite is too small, generally at several micrometers, and dispersive to be characterized in the mechanical behavior of individual austenite grain by the conventional analytical techniques. In order to resolve this issue, nanoindentation is employed in the present study to determine austenite mechanical stability, in which it allows hardness measurements at nanoscale.

1.4 Nanoindentation on mechanically induced martensitic transformation

Nanoindentation measurement is the most suitable to investigate the mechanical behavior of the individual austenite grains in such small-scale. A study [76] is reported that nanoindentation is carried out to confirm the appearance of martensitic transformation underneath the indentation mark combined with the TEM observation on cross-sectioned microstructure in multiphase TRIP steel. The experimental data are shown in Fig. 1.12, where (a) is the load-displacement curve of austenite grain indicated by the black dotted line with Hertz fit to identify the onset of plastic deformation indicated by the blue dashed line, and (b) is bright-field image of a cross-sectional view of the microstructure underneath the indentation mark and the diffraction patterns from the selected regions. The analysis of the diffraction patterns indicates that the region closest to the indentation mark is identified to be the transformed martensite and the adjacent region is the original austenite grain, in which martensitic transformation is related to the intermittent displacement bursts in the loading segment of the load-displacement curve of metastable austenite. In the additional study [77], the ε-martensite transformation occurs during nanoindentation in high nitrogen stainless steel, in which it also leads to the intermittent displacement bursts in the plastic deformation stage of the load-displacement curve.

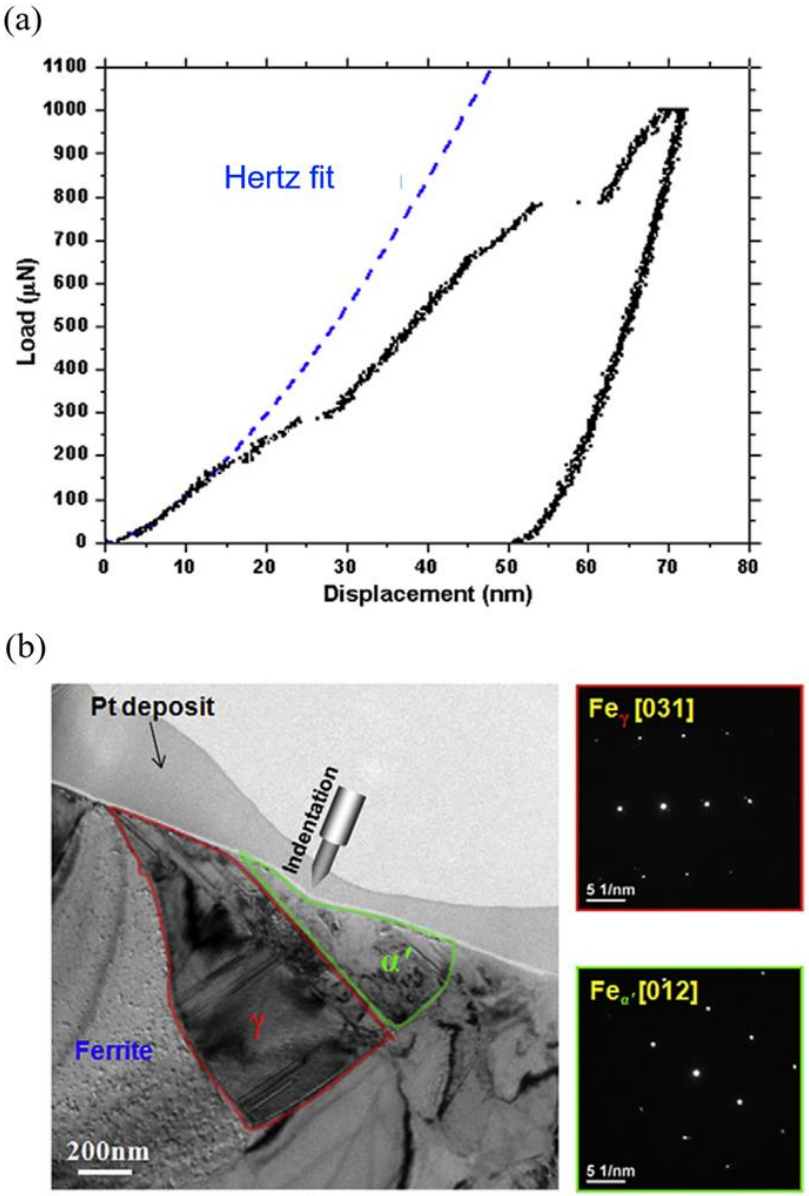

Figure 1.12 (a) The load-displacement curve of austenite grain indicated by the black dotted line, and Hertz fit to identify the onset of plastic deformation indicated by the blue dashed line, and (b) bright-field image of a cross-sectional view of the microstructure underneath the indentation mark and the diffraction patterns from the selected regions [76].

Mechanical stability of retained austenite in nanoscale is similarly investigated in high carbon martensitic steel using nanoindentation which is combined with EBSD measurements carried out before and after nanoindentation test [78]. Figures 1.13(a) and (b) are phase maps of austenite in blue and martensite in red obtained from EBSD measurements before and after nanoindentation, respectively. Figure 1.13(c) is the

corresponding load-displacement curve, where the blue arrows indicate the displacement bursts during nanoindentation, and the red dashed line represents the calculated Hertz elastic contact solution. The microstructure at the indented region demonstrates that the appearance of the martensite is presumably the consequence of the nanoindentation, leading to the displacement bursts in the load-displacement curve. The curve deviated from the Hertz fit line marks as an initiation of plastic deformation. The following bursts in displacement should be associated with dislocation movement and martensitic transformation.

As described above, nanoindentation is a powerful technique to examine the mechanical behavior of austenite phase. However, it cannot be identified which burst is correlated to martensitic transformation through the load-displacement curve. What's more, no detail interpretations on mechanical stability of austenite is described. Therefore, it is essential to develop a new analytical method to better understand the deformation behaviors in Fe alloys using nanoindentation.

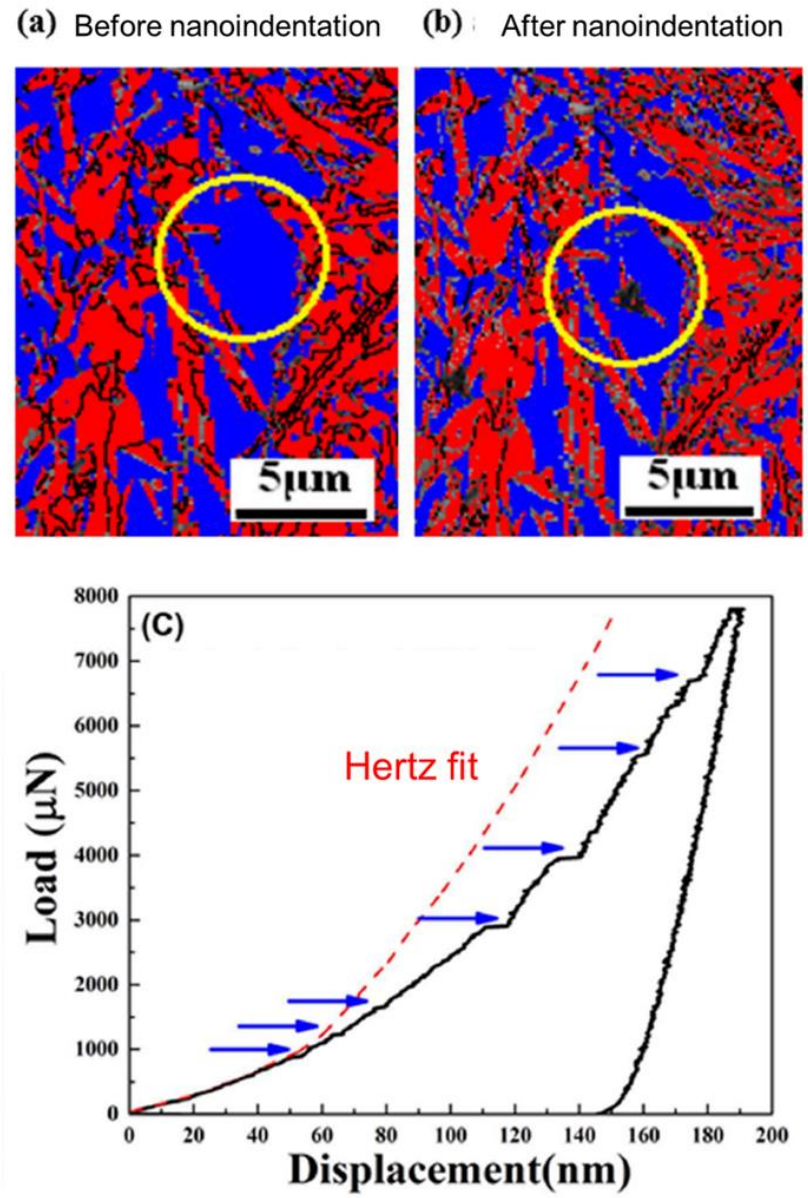

Figure 1.13 (a) and (b) Phase maps of austenite in blue and martensite in red obtained from EBSD measurements before and after nanoindentation, respectively. (c) The corresponding load-displacement curve, where the blue arrows indicate the displacement bursts during nanoindentation, and the red dashed line represents the calculated Hertz elastic contact solution [78].

1.5 Aim and objective of the research

Although there is a large number of published studies, to the authors' knowledge, the dependency of grain size on the mechanical stability of austenite has not been made clear yet. The present research aims to investigate the individual effect of grain size of retained austenite on the mechanical stability, and have better knowledge on the deformation mechanism of austenite.

The scope of this thesis includes five chapters that background in chapter 1, the primary investigations in chapters 2, 3, and 4, and summary and conclusion in chapter 5. The objectives of the thesis are described as follows:

(1) In chapter 2, a new evaluation method using the slope *a* of the *P/h* versus *h* plot obtained from nanoindentation is proposed to visually and quantitatively identify the plastic deformation modes. The mechanical behaviors of the SUS 316, Fe-30Ni, IF, and Fe-0.4C steels are respectively characterized by nanoindentation to corroborate the relationship between the slope *a* value of the *P/h* versus *h* plot and the nanohardness H_n. The grain boundary effect in the IF (ferrite phase) and the Fe-30Ni (stable austenite phase) steels is also investigated.

(2) In chapter 3, the mechanical behaviors of the martensite in the Fe-27Ni steel and the stable austenite in the Fe-30Ni steel are studied to compare the plastic deformation mode with the metastable austenite in the Fe-27Ni steel. The effects of austenite grain boundary and γ/α' interface on the mechanical stability of individual austenite grain are investigated to make clear the boundary effect on the resistance to nanoindentation-induced martensitic transformation.

(3) In chapter 4, the mechanical behavior of individual retained austenite grains in the Fe-1.4C-12Cr steel is described to understand the plastic deformation mechanism. Moreover, the effect of grain size on the mechanical stability of

individual retained austenite phase is shown.

References

[1] L. Fulton, O. Lah, F. Cuenot, Transport pathways for light duty vehicles: Towards a 2° scenario, Sustainability, 5 (2013) 1863-1874.

[2] C. Yuce, F. Karpat, N. Yavuz, G. Sendeniz, A case study: Designing for sustainability and reliability in an automotive seat structure, Sustainability, 6 (2014) 4608-4631.

[3] U.S. Energy Information Administration, International Energy Outlook 2016. Available online: http://www.eia.gov/forecasts/ieo/pdf/0484(2016).pdf

[4] D. K. Matlock, J. G. Speer, E. De Moor, P. J. Gibbs, Recent developments in advanced high strength sheet steels for automotive applications: An overview, Jestech, 15 (2012) 1 1-12.

[5] M. W. Andure, S. C. Jirapure, L. P. Dhamande, Advance automobile material for light weight future - A review. Proc. on International Conference on Benchmarks in Engineering Science and Technology 2012 ICBEST 1, 2012, 15-22.

[6] Steel definitions: Today's AHSS for automotive, WorldAutoSteel. Available online: https://www.worldautosteel.org

[7] M. Y. Demeri, Advanced high-strength steels- Science, technology, and application, ASM International, 2013.

[8] D. Bhattacharya, Developments in advanced high strength steels, Advanced High Strength Steel Workshop, Arlington, Virginia, 2006.

[9] N. Baluch, Z. M. Udim, C. S. Abdullah, Advanced high strength steel in auto industry: An overview, Eng. Tech. Appl. Sci. Res., 4 (2014) 4 686-689.

[10] C. M. Tamarelli, AHSS 101- The evolving use of AHSS for automotive

applications, Steel Market Development Institute, Washington, D. C., 2012.

[11] J. Shaw, B. Engl, C. Espina, E. Oren, ULSAB-Advanced vehicle concepts-Materials, SAE technical paper, 2002-01-0044.

[12] Z. Nishiyama, Martensitic transformation, New York, Academic Press, 1978.

[13] G. Krauss, A. Marder, The morphology of martensite in iron alloys, Metall. Mater. Trans. B, 2 (1971) 2343-2357.

[14] M. Umemoto, T. Hyodo, T. Maeda, I. Tamura, Electron microscopy studies of butterfly martensite, Acta Metall., 32 (1984) 1191-1203.

[15] M. Umemoto, I. Tamura, The morphology and substructure of butterfly martensite in ferrous alloys, J. de Phys. Colloques, 43 (1982) 523-528.

[16] G. Krauss, Steels: Processing, structure and performance, Second Edition, Materials Park, Ohio, ASM International, 2005.

[17] T. Maki, Microstructure and mechanical behavior of ferrous martensite, Mater. Sci. Forum, 56-58 (1990) 157-168.

[18] T. Maki, Recent advance in understanding martensite in steels, Proc. of the 1st International Symposium on Steel Science (IS3-2007), ISIJ, Kyoto, 2007, 1-10.

[19] D. H. Huang, G. Thomas, Structure and mechanical properties of tempered martensite and lower bainite in Fe-Ni-Mn-C steels, Metall. Trans., 2 (1971) 1587-1598.

[20] S. Morito, H. Tanaka, R. Konishi, T. Furuhara, T. Maki, The morphology and crystallography of lath martensite in Fe-C alloys, Acta Mater., 51 (2003) 1789-1799.

[21] M. Umemoto, E. Yoshitake, I. Tamura, The morphology of martensite in Fe-C, Fe-Ni-C and Fe-Cr-C alloys, J. Mater. Sci., 18 (1983) 2893-2904.

[22] A. Shibata, S. Morito, T. Furuhara, T. Maki, Characterization of substructure evolution in ferrous lenticular martensite, Mater. Sci. Forum, 654-656 (2010) 1-6.

[23] E. C. Bain, The nature of martensite, Trans. AIME, 70 (1924) 25-46.

[24] G. Kurdjumov, G. Sachs, Uber den mechanismus det stahlhartung, Z. Phys., 64 (1930) 325-343.

[25] Z. Nishimiya, On the transformation gamma-alpha of stainless invar caused by stress and the mechanism of the transformation, Sci. Rep. Tohoku Imperial University, 25 (1936) 94-103.

[26] G. Wassermann, Einfluβ der α-γ-umwandlung eines irreversiblen nickelstahls auf krystallorientierung und zugfestigkeit. Archiv fur das Eisenhuttenwesen, 6 (1933) 347-351.

[27] A. B. Greninger, A. R. Troiano, The mechanism of martensite formation, Trans. AIME, 140 (1940) 307-336.

[28] W. Pitsch, Der Orientierungszusammenhang zwischen Zementit und Austenit, Acta Metall., 10 (1962) 897-900.

[29] V. F. Zackay, E.R. Parker, D. Fahr, R. Busch, The enhancement of ductility in high-strength steels, Trans. ASM, 60 (1976) 252-259.

[30] P. Payson, C. H. Savage, Martensite reactions in alloy steels, Trans. ASM, 33 (1944) 261-275.

[31] R. A. Grange, H. M. Stewart, The temperature range of martensite formation, Trans. AIME, 167 (1946) 467-490.

[32] K. W. Andrews, Empirical formulae for the calculation of some transformation temperatures, J. of Iron Steel Ins., 203 (1965) 721-727.

[33] J. Wang, P. J. V. D. Wolk, S. V. D. Zwaag, Determination of martensite start temperature in engineering steels: Part I. Empirical relations describing the effect of steel chemistry, Mater. Trans. JIM, 41 (2000) 761-768.

[34] T. J. Angel, Formation of martensite in austenitic stainless steels, J. Iron Steel Ins., 177 (1954) 165-174.

[35] G. B. Olson, M. Cohen, A mechanism for the strain-induced nucleation of martensitic transformations, J. Less Common Metals, 28 (1972) 107-118.

[36] G. B. Olson, M. Cohen, Stress-assisted isothermal martensitic transformation: Application to TRIP steels, Metall. and Mater. Trans. A, 13 (1982) 1907-1914.

[37] G. Reisner, E. A. Werner, P. Kerschbaummayr, I. Papst, F. D. Fischer, The modeling of retained austenite in low-alloyed TRIP steels, JOM, 49 (1997) 62-65.

[38] R. M. Wu, W. Li, C. L. Wang, Y. Xiao, L. Wang, X. J. Jin, Stability of retained austenite through a combined intercritical annealing and quenching and partitioning (IAQP) treatment, Acta Metall. Sin. (Engl. Lett.), 28 (2015) 386-393.

[39] G. B. Olson, Transformation plasticity and the stability of plastic flow, ASM, (1984) 391-424.

[40] M. L. Brandt, G. B. Olson, Bainitic stabilization of austenite in low alloy sheet steels, Iron and steelmaker, 20 (1993) 55-60.

[41] E. Jimenez-Melero, N. H. V. Dijk, L. Zhao, J.Sietsma, S. E. Offerman, J. P. Wright, S. V. D. Zwaag, Characterization of individual retained austenite grains and their stability in low-alloyed TRIP steels, Acta Mater., 55 (2007) 6713-6723.

[42] R. Blonde, E. Jimenez-Melero, L.Zhao, J. P. Wright, E. Bruck, S.V. D. Zwaag, N. H. V. Dijk, High-energy X-ray diffraction study on the temperature-dependent mechanical stability of retained austenite in low-alloyed TRIP steels, Acta Mater., 60 (2012) 565-577.

[43] Y. F. Shen, L. N. Qiu, X. Sun, L. Zuo, P. K. Liaw, D. Raabe, Effects of retained austenite volume fraction, morphology, and carbon content on strength and ductility of nanostructured TRIP-assisted steels, Mater. Sci. Eng. A 638 (2015) 551-564.

[44] B. Demir, M. Erdogan, The hardenability of austenite with different alloy content and dispersion in dual-phase steels, J. Mater. Pro. Tech., 208 (2008) 75-84.

[45] S. J. Kim, Effects of manganese content and heat treatment condition on mechanical properties and microstructures of fine-grained low carbon TRIP-aided steels, Mater. Sci. Forum 638-642 (2010) 3313-3318.

[46] E. D. Moor, J. G. Speer, D. K. Matlock, J. H. Kwak, S. B. Lee, Effect of carbon and manganese on the quenching and partitioning response of CMnSi steels, ISIJ Int., 51 (2011) 137-144.

[47] J. Tobata, K. L. Ngo-Huynh, N. Nakada, T. Tsuchiyama, S. Takaki, Role of silicon in quenching and partitioning treatment of low-carbon martensitic stainless steel, ISIJ Int., 52 (2012) 1377-1382.

[48] B. Sun, F. Fazeli, C. Scott, N. Brodusch, R. Gauvin, S. Yue, The influence of silicon additions on the deformation behavior of austenite-ferrite duplex medium manganese steels, Acta Mater., 148 (2018) 249-262.

[49] M. H. Saleh, R. Priestner, Retained austenite in dual-phase silicon steels and its effect on mechanical properties, J. of Mater. Proc. Tech., 113 (2001) 587-593.

[50] B. C. De Cooman, Structure-properties relationship in TRIP steels containing carbide-free bainite, Curr. Opin. Solid State Mater. Sci., 8 (2004) 285-303.

[51] S. Chatterjee, M. Murugananth, H. K. D. H. Bhadeshia, δ TRIP steel, Mater. Sci. Tech., 23 (2007) 819-827.

[52] M. De Meyer, D. Vanderschueren, B. C. De Cooman, The influence of the substitution of Si by Al on the properties of cold rolled C-Mn-Si TRIP steels, ISIJ Int., 39 (1999) 813-822.

[53] J. Y. Kang, H. C. Lee, S. H. Han, Effect of Al and Mo on the textures and microstructures of dual phase steels, Mater. Sci. Eng. A 530 (2011) 183-190.

[54] E. Jimenez-Melero, N. H. V. Dijk, L. Zhao, J.Sietsma, S. E. Offerman, J. P. Wright, S. V. D. Zwaag, The effect of aluminum and phosphorus on the stability of individual austenite grains in TRIP steels, Acta Mater., 57 (2009) 533-543.

[55] K. Sugimoto, B. Yu, Y. Mukai, S. Ikeda, Microstructure and formability of aluminum bearing TRIP-aided steels with annealed martensite matrix, ISIJ Int., 45 (2005) 1194-1200.

[56] H. Jirkova, L. Kucerova, B. Masek, The effect of chromium on microstructure development during Q-P process, Mater. Today: Proc. 2 S (2015) 627-630.

[57] R. Hossain, F. Pahlevani, V. Sahajwalla, Effect of small addition of Cr on stability of retained austenite in high carbon steel, Mater. Char., 125 (2017) 114-122.

[58] J. Kobayashi, D. Ina, N. Yoshikawa, K. Sugimoto, Effects of the addition of Cr, Mo and Ni on the microstructure and retained austenite characteristics of 0.2% C-Si-Mn-Nb ultrahigh-strength TRIP-aided bainitic Ferrite Steels, ISIJ Int., 52 (2012) 1894-1901.

[59] J. Chiang, J. D. Boyd, A. K. Pilkey, Effect of microstructure on retained austenite stability and tensile behavior in an aluminum-alloyed TRIP steel, Mater. Sci. Eng. A, 638 (2015) 132-142.

[60] T. Chen, L. Tan, Z. Lu, H. Xu, The effect of grain orientation on nanoindentation behavior of model austenitic alloy Fe-20Cr-25Ni, Acta Mater., 138 (2017) 83-91.

[61] C. H. Seo, K. H. Kwon, K. Choi, K. H. Kim, J. H. Kwak, S. Lee, Nack J. Kim, Deformation behavior of ferrite–austenite duplex lightweight Fe-Mn-Al-C steel, Scripta Mater., 66 (2012) 519-522.

[62] Y. B. Xu, Y. Zou, Z. P. Hu, D. T. Han, S. Q. Chen, R. D. K. Misra, Correlation between deformation behavior and austenite characteristics in a Mn-Al type TRIP steel, Mater. Sci. Eng. A, 698 (2017) 126-135.

[63] J. H. Ryu, D. I. Kim, H. S. Kim, H. K. D. H. Bhadeshia, D. W. Suh, Strain partitioning and mechanical stability of retained austenite, Scripta Mater., 63 (2010) 297-299.

[64] P. J. Jacques, Q. Furnemont, F. Lani, T. Pardoen, F. Delannay, Multiscale mechanics of TRIP-assisted multiphase steels: I. Characterization and mechanical

testing, Acta Mater., 55 (2007) 3681-3693.

[65] K. Sugimoto, A. Kanda, R. Kikuchi, S. Hashimoto, T. Kashima, S. Ikeda, Ductility and formability of newly developed high strength low alloy TRIP-aided sheet steels with annealed martensite matrix, ISIJ Int., 42 (2002) 910-915.

[66] R. Blonde, E. Jimenez-Melero, L. Zhao, J. P. Wright, E. Bruck, S. V. D. Zwaag, N. H. V. Dijk, High-energy X-ray diffraction study on the temperature-dependent mechanical stability of retained austenite in low-alloyed TRIP steels, Acta Mater., 60 (2012) 565-577.

[67] S. Cheng, X. Wang, Z. Feng, B. Clausen, H. Choo, P. K. Liaw, Probing the characteristic deformation behaviors of transformation-induced plasticity steels, Metall. Mater. Trans. A, 39 (2008) 3105-3112.

[68] D. D. Knijf, R. Petrov, C. Fojer, L. A. I. Kestens, Effect of fresh martensite on the stability of retained austenite in quenching and partitioning steel, Mater. Sci. Eng. A, 615 (2014), 107-115.

[69] P. J. Jacques, F. Delannay, J. Ladriere, On the influence of interactions between phases on the mechanical stability of retained austenite in transformation-induced plasticity multiphase steels, Metall. Mater. Trans. A, 32 (2001) 2759-2768.

[70] K. Sugimoto, M. Misu, M. Kobayashi, H. Shirasawa, Effects of second phase morphology on retained austenite morphology and tensile properties in a TRIP-aided dual-phase steel sheet, ISIJ Int., 33 (1993) 775-782.

[71] K. Sugimoto, T. IIDA, J. Sakaguchi, T. Kashima, Retained austenite characteristics and tensile properties in a TRIP type bainitic sheet steel, ISIJ Int., 40 (2000) 902-908.

[72] D. D. Knijf, C. Fojer, L. A. I. Kestens, R. Petrov, Factors influencing the austenite stability during tensile testing of quenching and partitioning steel determined via *in situ* electron backscatter diffraction, Mater. Sci. Eng. A, 638 (2015), 219-227.

[73] A. Z. Hanzaki, P. D. Hodgson, S. Yue, Retained austenite characteristics in thermomechanically processed Si-Mn transformation-induced plasticity steels,

Metall. Mater. Trans. A, 28 (1997) 2405-2414.

[74] D. Q. Bai, A. Di Chiro, S. Yue, Stability of retained austenite in a Nb microalloyed Mn-Si TRIP steel, Mater. Sci. Forum, 284-286 (1998) 253-262.

[75] Y. Matsuoka, T. Iwasaki, N. Nakada, T. Tsuchiyama, S. Takaki, Effect of grain size on thermal and mechanical stability of austenite in metastable austenitic stainless steel, ISIJ Int., 53 (2013) 1224-1230.

[76] T. H. Ahn, C. S. Oh, D. H. Kim, K. H. Oh, H. Bei, E. P. George, H. N. Han, Investigation of strain-induced martensitic transformation in metastable austenite using nanoindentation, Scripta Mater., 63 (2010) 540-543.

[77] T. H. Ahn, S. B. Lee, K. T. Park, K. H. Oh, H. N. Han, Strain-induced ε-martensite transformation during nanoindentation of high-nitrogen steel, Mater. Sci. Eng. A, 598 (2014) 56-61.

[78] R. Hossain, F. Pahlevani, M. Z. Quadir, V. Sahajwalla, Stability of retained austenite in high carbon steel under compressive stress: an investigation from macro to nano scale, Sci. Reports, 6 (2016) 34958.

Chapter 2 A new evaluation method for nanoindentation behaviors

2.1 Introduction

A requirement for developing a micromechanical model of TRIP-aided steels is the knowledge of the flow properties of each of the phases in the microstructure, especially retained austenite. The microstructure of retained austenite in TRIP-aided steels is too small and dispersive to be characterized in the mechanical behavior by the conventional analytical technique [1-4]. Nanoindentation is a compelling technique used for assessing the local mechanical properties of the microscale and nanoscale materials such as thin films, specific phases, and microelectronics that traditional hardness tests are not able to probe. The principle of nanoindentation, like other hardness measurement techniques, consists of applying a prescribed load to an indenter in contact with the specimen. The advantage of this technique is that a very small material volume is used and some mechanical properties can be assessed from the same indentation test [5-11]. The fundamental aspects in nanoindentation including Hertz contact theory, pop-in phenomenon, and Oliver-Pharr analysis method are described in sections 2.1.1 and 2.1.2.

In recent years, there are a few studies focused on the mechanically induced martensitic transformation in retained austenite which is the crucial nature for TRIP effect using nanoindentation technique, however, most of these results are regarded as the overall nanohardness and mechanism of this phenomenon [12-19]. However, the typical analytical method, the load versus penetration depth (P versus h) curve, used in the previous studies cannot directly and quantitatively demonstrate the deformation behaviors during loading, for example, when the martensitic transformation starts or completes during the plastic deformation in metastable austenite. Therefore, the new evaluation method using the load/penetration depth versus penetration depth (P/h versus h) plot is purposed to characterize the deformation modes in section 2.1.4. A study [20] in Fe-28Mn-6Si-5Cr shape memory alloy has shown that the plots of P/h

versus *h* converted from the typical *P* versus *h* curves exhibit two slope values during the plastic deformation, which presumably corresponds to the martensitic transformation and slip deformation. It indicates that the change in the slope of the *P/h* versus *h* plot is believed to be a change in the deformation modes.

In section 2.3, the three typical microstructures in the Fe alloys are employed to demonstrate deformation behaviors through the new evaluation method of the slope of the *P/h* versus *h* plot and corroborate the relationship between the slope of the *P/h* versus *h* plot and the nanohardness H_n. The effects of grain boundary in ferrite and stable austenite phases are also described using the values of the slope.

2.1.1 Hertz contact theory

H. Hertz first studied the nature of the stresses arising from the contact between two elastic bodies in 1881 [21]. His theory is found to be very accurately describing the contact between a rigid spherical indenter and a flat elastic half-space as shown in Fig. 2.1. Besides, it allows the quantification of the resulting contact area, contact pressure, compression of the bodies, and the induced stress and strain in the bodies.

The radius of the circular contact area r_c could be computed by H. Hertz as Eq. 2.1

$$r_c{}^3 = \frac{3}{4}\frac{PR_i}{E^*} \tag{2.1}$$

where *P* is the load, R_i is the radius of the indenter tip, and E^* is called reduced modulus which is a combination of the indentation modulus of the sample and indenter. The reduced modulus can be expressed by the following equation

$$\frac{1}{E^*} = \frac{1-v_s^2}{E_s} + \frac{1-v_i^2}{E_i} \tag{2.2}$$

where *E* and *v* are the elastic modulus and Poisson's ratio of the sample (s) and indenter (i), respectively.

The load P can be represented as a function of the penetration depth h on the axis during pure elastic deformation as Eq. 2.3

$$P = \frac{4}{3} E^* \sqrt{R_i} h^{\frac{3}{2}}. \quad (2.3)$$

Here, some assumptions are required for Hertz contact theory, such as continuous surface, pure elastic deformation, and small strains.

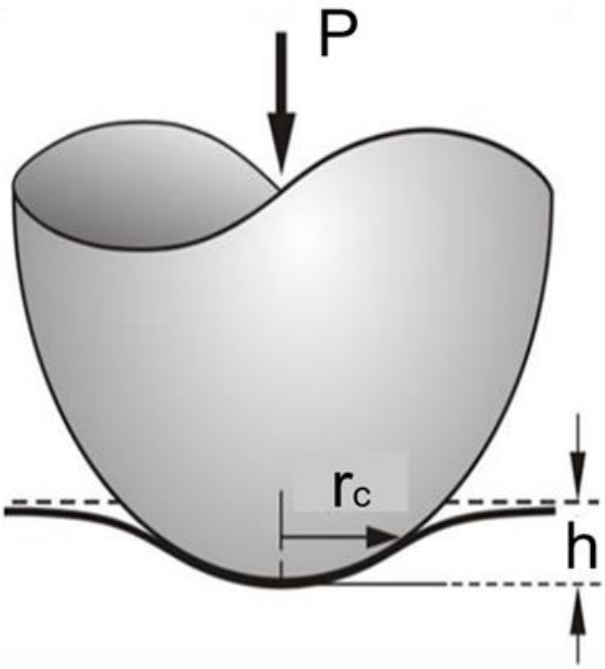

Figure 2.1 Schematic illustration of Hertz for contact between a rigid spherical indenter and an elastic half-space.

Over the last several decades, many studies have indicated that a displacement burst under load controlled mode or load drop under displacement controlled mode is observed in a loading segment, referred to pop-in [22-31], for single crystal and polycrystalline materials. Several mechanisms are reported to interpret the pop-in phenomenon. The first pop-in has been believed to be a process correlated with dislocation nucleation [24, 31]. The following pop-ins are associated with dislocation avalanche with fractal behavior [32, 33] or mechanically-induced phase transformation

[12-14]. Hertz contact theory (Eqs. 2.2 and 2.3) is used for identifying elastic and plastic deformation through fitting well to a load-displacement curve during nanoindentation where the first pop-in is considered as an initial of plastic deformation. This fitting method is employed to analyze the nanoindentation results in this study.

2.1.2 Oliver-Pharr analysis method

The hardness H of materials has been defined as the materials' resistance to plastic flow and is calculated by the indentation load P divided by the contact area A, namely as Eq. 2.4

$$H = \frac{P}{A}. \tag{2.4}$$

In the conventional indentation tests, the contact area is directly measured from the residual impression area. The material's hardness could then be easily calculated. However, in the nanoindentation tests, the residual impression area is too small to be directly measured by optical microscope. Therefore, the most notable and vital method is Oliver and Pharr analysis method in which the contact area is determined by the measured penetration depth along with the prescribed load [34]. In this method, the contact area under the load is acquired by measuring the slope of the unloading portion of the P versus h curve during the nanoindentation process, showing an elastic-plastic loading followed by elastic unloading. Figure 2.2 is a schematic P versus h curve showing loading and unloading during the nanoindentation process.

The slope S during the unloading segment of the P versus h curve in Fig. 2.2 is defined as the measured stiffness of materials. This value can be represented as the rate of change of the load over the rate of change of the penetrated depth, which can be related to the contact area and reduced modulus.

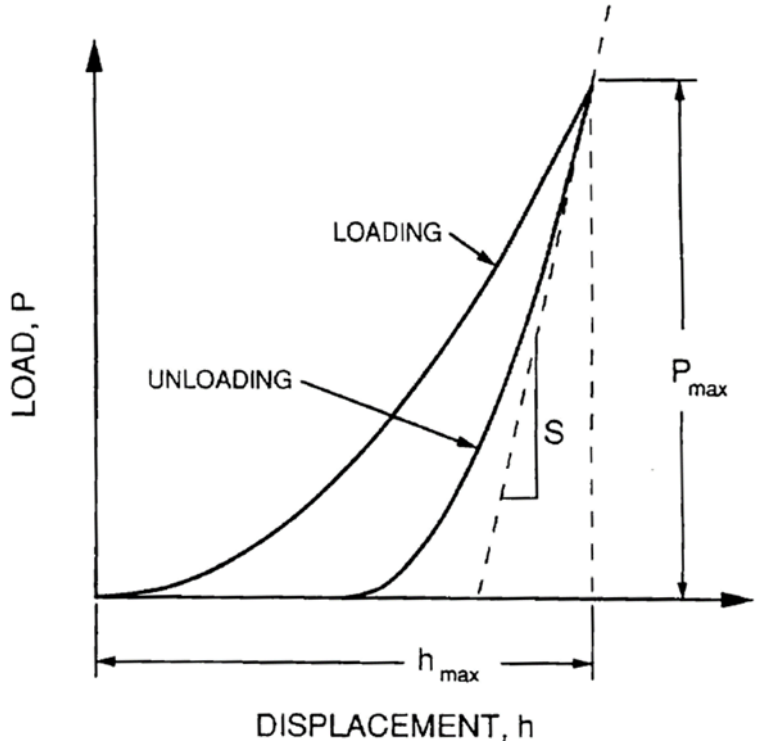

Figure 2.2 Schematic illustration of a typical *P* versus *h* curve showing loading and unloading during the nanoindentation process [34].

To calculate the elastic modulus and hardness of materials, the A should be first determined. The area under load during nanoindentation as a function of contact depth h_c is created and fitted by Eq. 2.5

$$A = C_0 h_c^2 + C_1 h_c + C_2 h_c^{1/2} + C_3 h_c^{1/4} + C_4 h_c^{1/8} + C_5 h_c^{1/16} \quad (2.5)$$

where C is the load frame compliance and C_0 through C_5 are constants. The lead term describes a perfect Berkovich indenter, C_0 =24.5. Unfortunately, a perfect Berkovich indenter is a utopia. Even if it is carefully manufactured, the indenter tip is usually blunted and/or have other defects, or it becomes imperfect after few nanoindentation tests. The Oliver and Pharr analysis method also evaluates the other fitting parameters to describe deviations from the perfect Berkovich geometry. At the shallower depths, the radius of curvature becomes the dominating effect in the area function, thus, allowing C_0 to vary will help take the non-perfect probe shape into account at shallower depth. As h_c increases, C_1 through C_5 of the area function polynomial fit become

negligible and the lead term becomes the most important term. When finding the coefficients for the area function, it is also best to use as few coefficients as possible.

The contact depth h_c can be determined from the experimental data, given by Eq. 2.6 and 2.7

$$h_c = h_{max} - h_s \tag{2.6}$$

$$h_s = k\ \frac{P_{max}}{S} \tag{2.7}$$

where h_{max} is the maximum penetration depth at peak load, h_s is the depth of the surface at a perimeter of the contact, and k is a geometric constant for conical indenters. A cross-sectional view of an indentation mark during the unloading process with the above-mentioned contact geometry parameters is shown in Fig. 2.3.

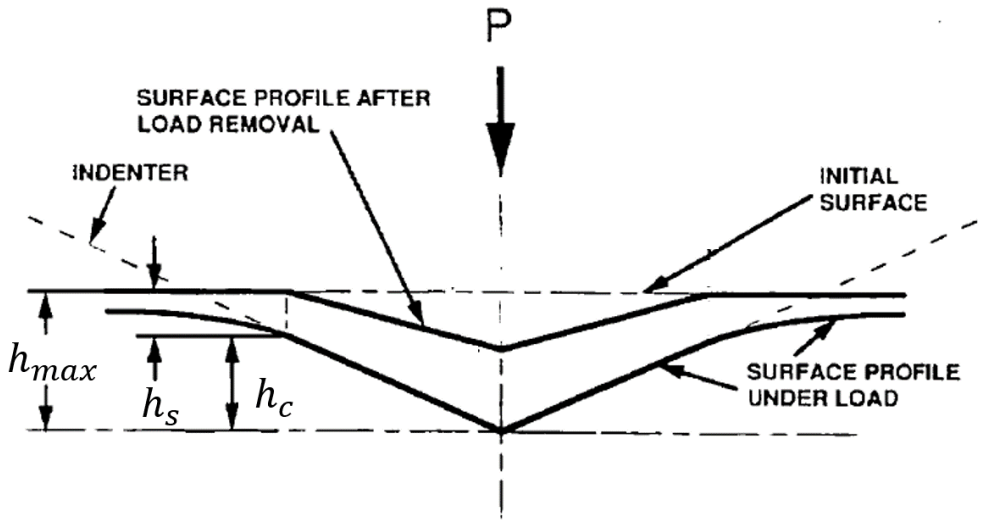

Figure 2.3 Schematic illustration of a cross-sectional view of an indentation mark during the unloading process [34].

2.1.3 Evaluation of hardness in a loading segment

Oliver-Pharr method is based on an analysis in unloading curve, as described in the previous section, and hence the hardness can be evaluated at peak load only. We sometimes need to evaluate hardness in a loading segment during increasing applied load, for example depth profile of hardness in layered structure materials. Therefore, another evaluation model is described as follows.

The theoretical load P creating an elastoplastic deformation in a loading segment can be given approximately as a function of penetration depth h [35]

$$P = ah^2 \tag{2.8}$$

where the parameter a is a constant.

The theoretical load P can also be expressed as

$$P_e = a_e h_e^2 \tag{2.9-1}$$

$$P_p = a_p h_p^2 \tag{2.9-2}$$

where the parameters a_e and a_p are constants for elastic and plastic deformation, and h_e and h_p are elastic and plastic penetration depth, respectively. It should be noted that $h_e \sim h_s$ and $h_p \sim h_c$ as shown in Fig. 2.3, respectively, therefore, the penetration depth h consists of elastic and plastic displacements, given by $h = h_e + h_p$ under a condition of load $P = P_e = P_p$. Therefore, the parameter a is written as

$$a^{-1/2} = a_e^{-1/2} + a_p^{-1/2}. \tag{2.10}$$

The parameters a_e and a_p respectively depend on the material constants, Young's modulus and the hardness. When the h_p is much larger than the h_e, only the parameter a_p is the controlling factor for the parameter a.

Nevertheless, in real case, the influences of tip truncation and the stiffness of load frame should be considered. Thus, the measured load P is given by

$$P = ah^2 + bh \tag{2.11}$$

where the parameter b is a constant. The parameter b corresponds to the shape of the indenter tip and the stiffness of the load frame.

Besides, as described in Eq. 2.4, the hardness H can be calculated by the indentation load P divided by the contact area A which is proportional to the square of the penetration depth h. Therefore, the hardness H is expressed as

$$H = P/A \propto P/h^2 = a. \tag{2.12}$$

That's to say, the parameter a is correlated to the hardness of materials, associated with the plastic deformation mechanisms.

Since the hardness consists of an integration of strength in each strain, which distributes in the strain field underneath the indenter. An example [36] shows the strain distribution for a Berkovich indenter. In Fig. 2.4, a high strain zone (strain > 20%) exists at the region close to the indenter, and the strain inversely decreases as the depth. The region at strain > 0.2% corresponds to the yield stress point. The higher strain region may include a strain hardening effect, but the strain distribution has similarity in any P (or h), independent on the indentation size, therefore, the hardness doesn't depend on the penetration depth when the deformed volume is homogeneous.

The parameter a changes if different deformation modes operate during plastic deformation. Hence the parameter a is the key factor in Eq. 2.11. The evaluation of the parameter a is of great importance in this study, which is described in the subsequent section 2.1.4.

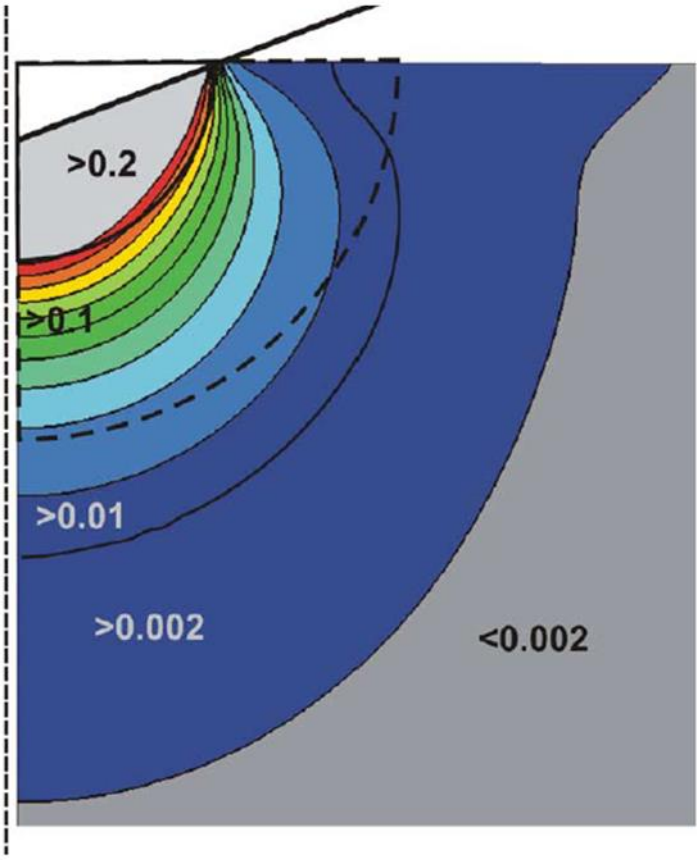

Figure 2.4 Axisymmetric geometry of a Berkovich indenter contacting an elastic-plastic material [36], showing the equivalent plastic strain ranging from 0.2% and 20%.

2.1.4 A new evaluation method of the parameter *a*

As described in the previous section, the parameter *a* is one of the key parameters to determine a deformation mechanism, hence it is applied to evaluate the mechanical stability of metastable austenite in the present study. The parameter *a* changes if different deformation modes operate during plastic deformation because the parameter *a* is correlated to the hardness, which is associated with the deformation mechanisms. There are three options to estimate the parameter *a* in experimental approaches.

One is that the parameter *a* is calculated by a differential *dP/dh* at a depth of a quadratic function of Eq. 2.11 fitted with the *P* versus *h* curve. Figure 2.5(a) is a typical *P* versus *h* curve of metastable austenite with the quadratic fitting line indicated by the red solid line. The function is apparent to include single *a* value even though the

deformation consists of two stages with different a as described later. Therefore, this method has poor accuracy to sense a a value, and hence is not good enough to find a change in a value, which corresponds to a transition of deformation mechanism when different deformation modes operate during the plastic deformation process. In other words, the transition point must be determined a priori for using this method to estimate multiple a values, which is significantly difficult experimental and almost impossible.

Another is making a plot of an incremental difference $\Delta P/\Delta h$ as a function of h for the experimental data. Figure 2.5(b) shows $\Delta P/\Delta h$ versus h plot in each incremental step with 5 ms interval time of data recording for the same data in Fig. 2.5(a). The plot is badly scattered and it is absolutely difficult to estimate a value and transition point as well.

The other is that the typical equation Eq. 2.11 is converted to a linear equation, written as

$$P/h = ah + b. \tag{2.14}$$

Figure 2.5(c) shows the loading segment of P/h versus h plot for the same data in Fig. 2.5(a). The parameter a can be visually and quantitatively evaluated through the slope of the P/h versus h plot, which is given by the linear least squares fitting on plenty of experimental data points in a loading segment. Furthermore, the transition point P_t is clearly determined on the plot, which is another advantage in this method. This evaluation method is much easier to determine the a, and also the P_t can be measured without any assumption for the P-h data. Besides, one of the advantages of using this evaluation method is to visually show the elastic and plastic deformation stages even though the first pop-in is much smaller.

As described above, the P/h versus h plot is the best method to evaluate the values of the slope a that is associated with the plastic deformation mechanisms and the transition load P_t, which is carried out to assess the mechanical stability of metastable austenite in chapters 3 and 4.

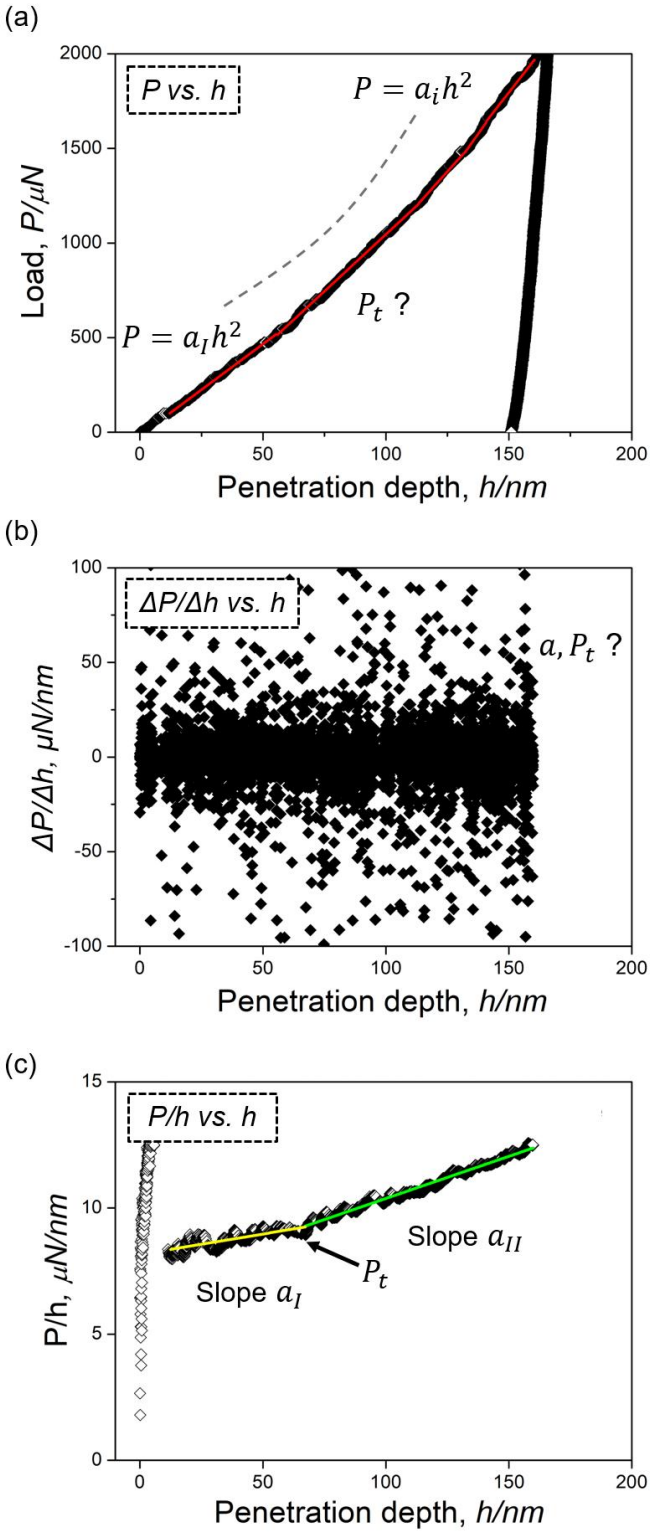

Figure 2.5 The nanoindentation behavior of metastable austenite in Fe-27Ni-H: (a) the typical *P* versus *h* curve, (b) the converted *ΔP/Δh* versus *h* plot, and (c) the converted loading segment of *P/h* versus *h* plot.

2.2 Experimental procedures

The SUS 316, Fe-30Ni, IF, and Fe-0.4C steels were chosen to investigate the mechanical behaviors of three typical microstructures, such as austenite, ferrite, and tempered martensite, and the chemical compositions were listed in Table 2.1. Among them, the Fe-30Ni and IF steels were also used to study the effect of grain boundary in the single phase.

Table 2.1 Chemical composition in mass%.

Noted	Fe	C	Cr	Ni	Mn	Si
SUS 316	Balanced	0.05	17.60	11.19	1.74	0.74
Fe-30Ni	Balanced	-	0.01	29.39	0.80	-
IF	Balanced	0.0017	-	-	0.147	0.022
Fe-0.4C	Balanced	0.40	-	<0.01	<0.01	<0.01

The SUS 316 steel was solution-treated at 1323 K for 4.8 ks followed by water cooling (virgin state), and then annealed at 973 K for 0.36 ks in an argon gas atmosphere then quenched in room temperature (293 K) to fix the aged microstructure. The Fe-30Ni steel was solution-treated at 1473 K for 10.8 ks followed by cooling down to 293 K in Ar gas flow. Subsequently, the Fe-30Ni sample was cold-rolled with a reduction of 68% and then annealed at 1073 K for 1.8 ks under vacuum to obtain the stable austenite phase. The IF steel was hot-rolled at 1213 K and then cooled in a furnace. The Fe-0.4C steel was austenitized at 1323 K for 0.9 ks, followed by ice-brine quenched, and then tempered at 473 K for 5.4 ks. The surfaces of SUS 316, IF, and Fe-0.4C samples for nanoindentation tests were finished by mechanically grinded, and subsequently electrolytic polished in a solution of 8 vol% perchloric acid, 60 vol% ethyl alcohol, 10 vol% butyl cellosolve, and 22 vol% distilled water under a voltage of 40 V to remove the damaged layer. Also, the surface of Fe-30Ni sample was polished in a

solution of 8 vol% perchloric acid, 73 vol% ethyl alcohol, 10 vol% butyl cellosolve, and 9 vol% distilled water under a voltage of 50 V.

Nanoindentation tests were carried out using a Hysitron TI 950 Triboindenter equipped with a Berkovich indenter, and the tip truncation was calibrated using a reference specimen of fused silica. All the nanoindentation tests were performed under a load-control condition with constant loading and unloading rate of the indenter, set at 50 μN/s with a holding segment of 10 s. The Oliver and Pharr method [34] was performed to analyze for the tip calibration and the hardness calculation. The probed sites and the indenter configurations on the sample surfaces were observed by the scanning probe microscopy (SPM) before and after the nanoindentation tests.

2.3 Results and discussion

2.3.1 Nanoindentation behaviors in Fe alloys

The nanoindentation tests were respectively carried out for stable austenite in the SUS 316 and the Fe-30Ni, ferrite in the IF, and tempered martensite in the Fe-0.4C to measure the nanohardness and examine the mechanical behaviors. The P versus h curves and the corresponding loading segment of P/h versus h plots are shown in Fig. 2.6. The P/h versus h plots of the four samples show almost constant values of the slope a in the plastic deformation stage for each plot, which suggests that a single deformation mode dominates the behavior during the plastic deformation. The data obtained from the Fe-0.4C indicate that the nanoindentation curve is sensitive for fine and complicated microstructure of tempered lath martensite, such as inside lath, lath boundary, and block boundary. Furthermore, the results of the nanohardness H_n of the three typical microstructures show a decreasing trend: tempered martensite> stable austenite> ferrite.

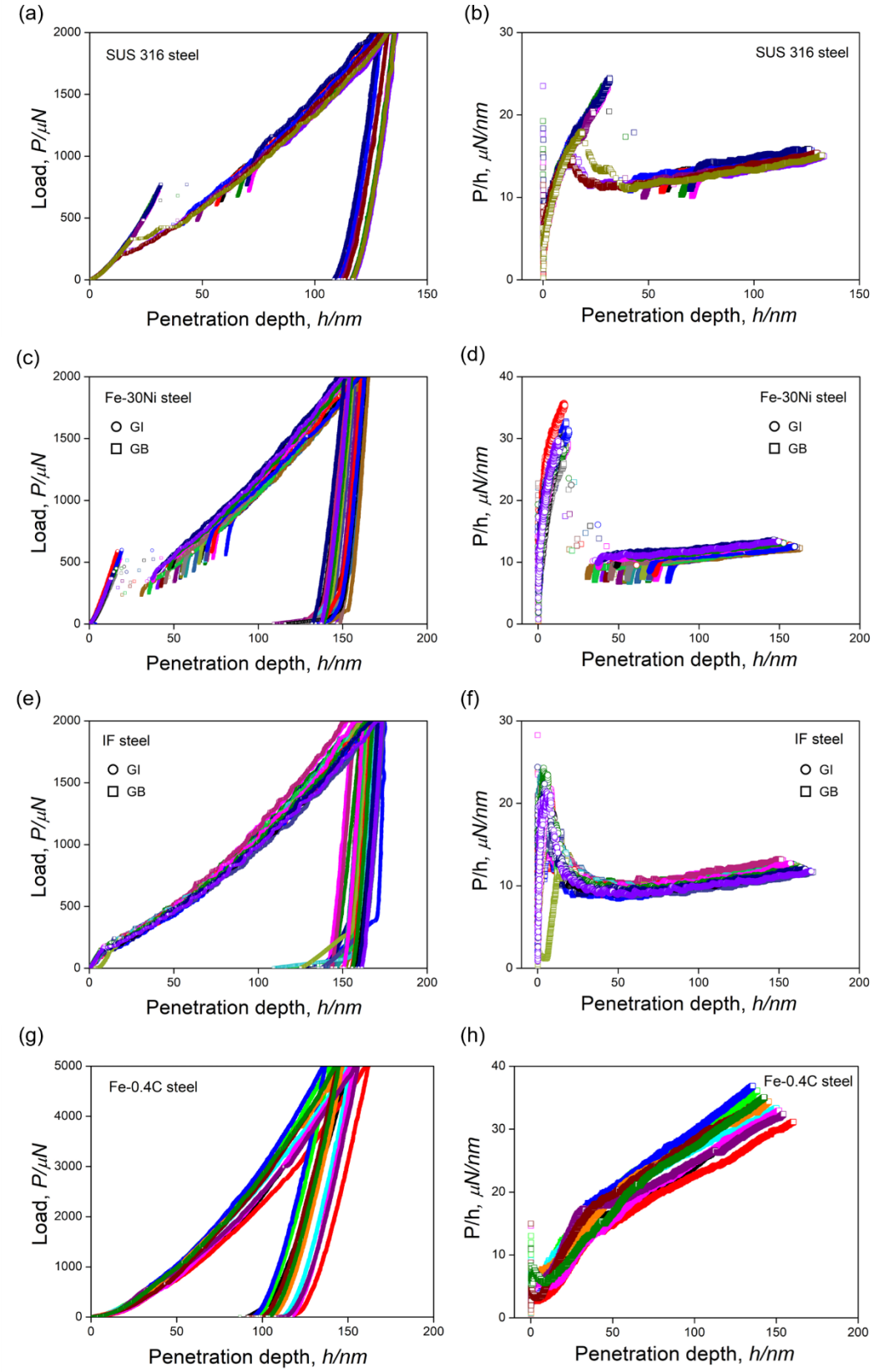

Figure 2.6 The *P* versus *h* curves and the corresponding loading segment of *P/h* versus *h* plots of (a), (b) SUS 316, (c), (d) Fe-30Ni, (e), (f) IF, and (g), (h) Fe-0.4C samples.

2.3.2 A relation between the slope *a* and the nanohardness H_n

Figure 2.7 is the relation between the slope *a* of the loading segment of the *P/h* versus *h* plot and the nanohardness H_n for stable austenite in the SUS 316 and the Fe-30Ni, ferrite in the IF, and tempered martensite in the Fe-0.4C. The data show that the slope *a* proportionally increases as the nanohardness H_n for the four Fe alloys, which is in concordance with the derived equation. This relation has also been substantiated in other alloys [37]. Although the scattering data are shown in the Fe-0.4C, it is presumably due to the fine and complicated microstructure of tempered lath martensite. As the nanohardness of materials is associated with the deformation mechanisms, the slope *a* should be forcefully affected by the plastic deformation mechanisms. The slope *a* values for stable austenite, ferrite, and tempered martensite hold almost constant, which indicates the single deformation mechanism, which is presumably corresponding to dislocation glide motion in this case, dominates the plastic behavior during loading. In addition, the austenite phase in the SUS 316 and the Fe-30Ni is speculated to be more stable against the indentation-induced martensitic transformation.

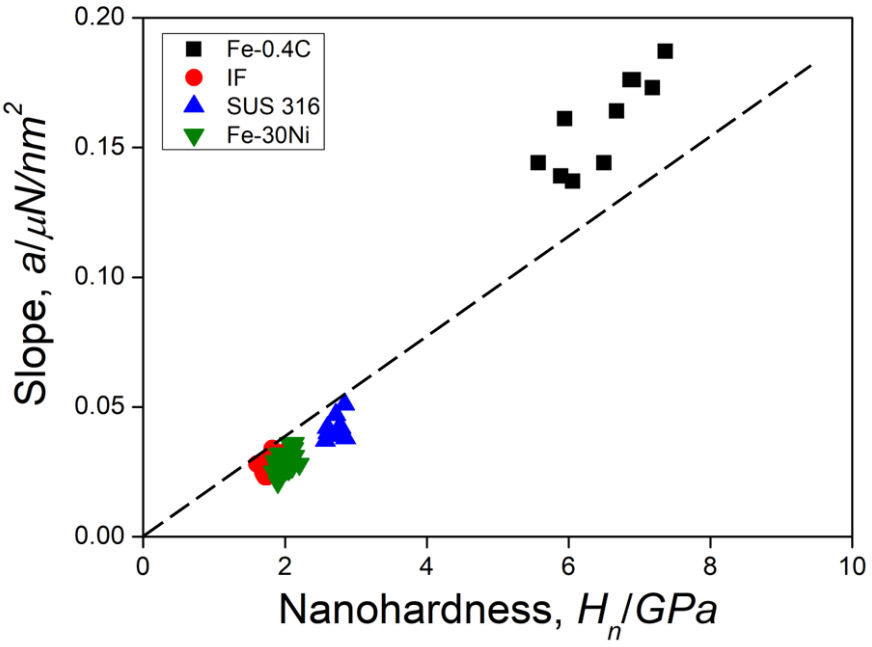

Figure 2.7 The relation between the slope *a* values of the loading segment of the *P/h* versus *h* plots and the nanohardness H_n.

As mentioned above, the slope a in a loading segment of the P/h versus h plot exhibits a proportional relation with the nanohardness H_n. It is believed that the slope a changes when different deformation modes operate during the plastic deformation. The new evaluation method using the P/h versus h plot is suitable and powerful to assess the mechanical stability of metastable austenite in chapters 3 and 4.

2.3.3 Effect of grain boundary on mechanical behaviors of ferrite and stable austenite

In order to confirm the effects of grain boundary of ferrite and stable austenite on their mechanical behaviors, nanoindentation tests were performed at grain interior and in the vicinity of grain boundary of ferrite phase in the IF and stable austenite phase in the Fe-30Ni, respectively, in which about 15 data points were collected for each position. Figure 2.8 shows SPM images taken after the nanoindentation tests showing the indentation marks at grain interior (GI) and in the vicinity of grain boundary (GB), where Figs. 2.8(a) and 2.8(b) are for the IF, and Figs. 2.8(c) and 2.8(d) are for the Fe-30Ni.

Figure 2.9 shows the average values of the slope a at grain interior and the vicinity of grain boundary for the IF and the Fe-30Ni samples. The difference in the average values of the slope a between the vicinity of grain boundary and the grain interior, referred to Δa ($\Delta a = a_{GBaverage} - a_{GIaverage}$), is 0.002 μN/nm^2 for ferrite and 0.004 μN/nm^2 for stable austenite, respectively. In the plot, the error bars are calculated by the standard deviation for total data. Interestingly, the Δa value is not remarkable for ferrite and stable austenite. As mentioned in section 2.3.2, the slope a value strongly corresponds to the nanohardness, which is associated with deformation mechanisms. It suggests that the deformation behavior for grain interior and the vicinity of grain boundary is presumably to be similar. That's to say, the grain boundary has comparatively lower resistance to the dislocation-grain boundary interaction for ferrite and stable austenite. The effect of grain boundary on the mechanical behavior of stable austenite will be

compared with that of metastable austenite in the Fe-27Ni described in section 3.3.2.

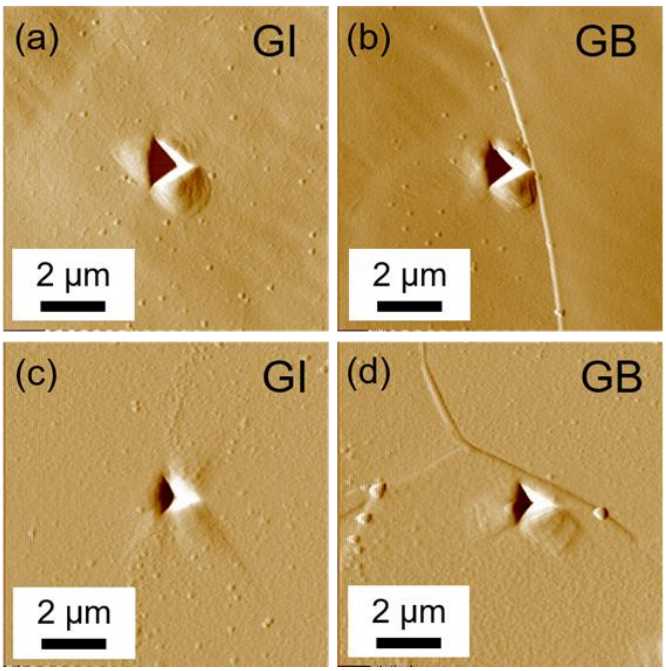

Figure 2.8 SPM images taken after the nanoindentation tests showing the indentation marks at grain interior and the vicinity of grain boundary. (a), (b) The IF sample, and (c), (d) the Fe-30Ni sample. Here, GI indicates grain interior, and GB indicates the vicinity of grain boundary.

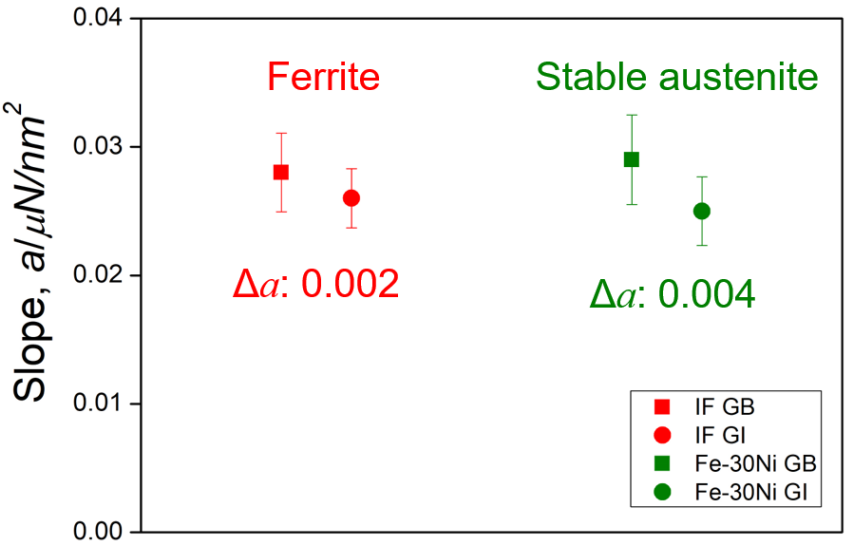

Figure 2.9 The average values of the slope *a* at grain interior and the vicinity of grain boundary for the IF and the Fe-30Ni samples.

2.4 Conclusions

The three typical microstructures in the Fe alloys (SUS 316, Fe-30Ni, IF, and Fe-0.4C) were carried out to investigate the deformation behaviors using nanoindentation.

(1) An effective and powerful evaluation method using the *P/h* versus *h* plot is described to characterize the mechanical behaviors in Fe alloys.

(2) The linear relation between the slope *a* of the loading segment of the *P/h* versus *h* plot and the nanohardness H_n is estimated. The slope *a* increases proportionally as the nanohardness H_n, which is strongly affected by the plastic deformation mechanisms.

(3) The constraint by grain boundary to the dislocation-grain boundary interaction is not remarkable for ferrite and stable austenite phases.

References

[1] J. H. Ryu, D. Kim, H. S. Kim, H. K. D. H. Bhadeshia, D. Suh, Strain partitioning and mechanical stability of retained austenite, Scripta Mater., 63 (2010) 297-299.

[2] R. Hossain, F. Pahlevani, V. Sahajwalla, Effect of small addition of Cr on stability of retained austenite in high carbon steel, Mater. Char., 125 (2017) 114-122.

[3] R. Ding, D. Tang, A. Zhao, A novel design to enhance the amount of retained austenite and mechanical properties in low-alloyed steel, Scripta Mater., 88 (2014) 21-24.

[4] D. D. Knijf, R. Petrov, C. Fojer, L. A. I. Kestens, Effect of fresh martensite on the stability of retained austenite in quenching and partitioning steel, Mater. Sci. Eng. A, 615 (2014) 107-115.

[5] T. Ohmura, T. Hara, K. Tsuzaki, Relationship between nanohardness and microstructures in high-purity Fe-C as-quenched and quench-tempered martensite,

J. Mater. Res., 6 (2003) 1465-1470.

[6] T. Ohmura, K. Tsuzaki, Plasticity initiation and subsequent deformation behavior in the vicinity of single grain boundary investigated through nanoindentation technique, J. Mater. Sci., 42 (2007) 1728-1732.

[7] T. Ohmura, K. Tsuzaki, S. Matsuoka, Nanohardness measurement of high-purity Fe-C martensite, Scripta Mater., 45 (2001) 889-894.

[8] T. Ohmura, K. Tsuzaki, F. Yin, Nanoindentation-induced deformation behavior in the vicinity of single grain boundary of Interstitial-Free steel, Mater. Trans., 46 (2005) 2026-2029.

[9] T. Ohmura, K. Sawada, K. Kimura, K. Tsuzaki, Alteration in nanohardness of matrix phase associated with precipitation during long-term aging of type 316 stainless steel, Mater. Sci. Eng. A, 489 (2008) 85-92.

[10] K. Miyahara, N. Nagashima, T. Ohmura, S. Matsuoka, Evaluation of mechanical properties in nanometer scale using AFM-based nanoindentation tester, Nanostructured Mater., 12 (1999) 1049-1052.

[11] Q. Furnemont, M. Kempf, P. J. Jacques, M.Goken, F. Delannay, On the measurement of the nanohardness of the constitutive phases of TRIP-assisted multiphase steels, Mater. Sci. Eng. A, 328 (2002) 26-32.

[12] T. H. Ahn, C. S. Oh, D. H. Kim, K. H. Oh, H. Bei, E. P. George, H. N. Han, Investigation of strain-induced martensitic transformation in metastable austenite using nanoindentation, Scripta Mater., 63 (2010) 540-543.

[13] T. H. Ahn, S. B. Lee, K. T. Park, K. H. Oh, H. N. Han, Strain-induced ε-martensite transformation during nanoindentation of high-nitrogen steel, Mater. Sci. Eng. A, 598 (2014) 56-61.

[14] R. Hossain, F. Pahlevani, M. Z. Quadir, V. Sahajwalla, Stability of retained austenite in high carbon steel under compressive stress: an investigation from macro to nano scale, Sci. Reports, 6 (2016) 34958.

[15] G. Cheng, K. S. Choi, X. Hu, X. Sun, Determining individual phase properties in a multi-phase Q&P steel using multi-scale indentation tests, Mater. Sci. Eng. A, 652 (2016) 384-395.

[16] J. J. Roa, G. Fargas, A. Mateo, E. Jimenez-Pique, Dependence of nanoindentation hardness with crystallographic orientation of austenite grains in metastable stainless steels, Mater. Sci. Eng. A, 645 (2015) 188-195.

[17] Y. Kim, T. Ahn, D. Suh, H. N. Han, Variant selection during mechanically induced martensitic transformation of metastable austenite by nanoindentation, Scripta Mater., 104 (2015) 13-16.

[18] T. Chen, L. Tan, Z. Lu, H. Xu, The effect of grain orientation on nanoindentation behavior of model austenitic alloy Fe-20Cr-25Ni, Acta Mater., 138 (2017) 83-91.

[19] B. B. He, M. X. Huang, Z. Y. Liang, A. H. W. Ngan, H. W. Luo, J. Shi, W.Q. Cao, H. Dong, Nanoindentation investigation on the mechanical stability of individual austenite grains in a medium-Mn transformation-induced plasticity steel, Scripta Mater., 69 (2013) 215-218.

[20] K. Sekido, T. Ohmura, T. Sawaguchi, M. Koyama, H.W. Park, K. Tsuzaki, Nanoindentation/atomic force microscopy analyses of ε-martensitic transformation and shape memory effect in Fe-28Mn-6Si-5Cr alloy, Scripta Mater., 65 (2011) 942-945.

[21] H. Hertz, Uber die beruhrung fester elastischer korper, J. Reine und Angew. Meth., 92 (1881) 156-171.

[22] W. W. Gerberich, J. C. Nelson, E. T. Lilleodden, P. Anderson, J. T. Wyrobek, Indentation induced dislocation nucleation: The initial yield point, Acta Mater., 44 (1996) 3585-3598.

[23] D. Lorenz, A. Zeckzer, U. Hilpert, P. Grau, Pop-in effect as homogeneous nucleation of dislocations during nanoindentation, Phys. Rev. B, 67 (2013) 172101.

[24] L. Zhang, T. Ohmura, Plasticity initiation and evolution during nanoindentation of

an iron-3% silicon crystal, Phys. Rev. Lett., 112 (2014) 145504.

[25] T. Ohmura, L. Zhang, K. Sekido, K. Tsuzaki, Effects of lattice defects on indentation-induced plasticity initiation behavior in metals, J. Mater. Res., 27 (2012) 13 1742-1749.

[26] W. W. Gerberich, S. K. Venkataraman, H.Huang, S. E. Harvey, D. L. Kohlstedt, The injection of plasticity by millinewton contacts, Acta Metall. Mater., 43 (1995) 1569-1576.

[27] S. G. Corcoran, R. J. Colton, E. T. Lilleodden, W. W. Gerberich, Anomalous plastic deformation at surfaces: Nanoindentation of gold single crystals, Phys. Rev. B, 55 (1997) R16057.

[28] S. Suresh, T. -G. Nieh, B. W. Choi, Nano-indentation of copper thin films on silicon substrates, Scripta Mater., 41 (1999) 951-957.

[29] A. Gouldstone, H. -J. Koh, K. -Y. Zeng, A. E. Giannakopoulos, S. Suresh, Discrete and continuous deformation during nanoindentation of thin films, Acta Mater., 48 (2000) 2277-2295.

[30] A. Gouldstone, K. J. V. Vliet, S. Suresh, Nanoindentation: Simulation of defect nucleation in a crystal, Nature, 411 (2001) 656.

[31] A. Gouldstone, N. Chollacoop, M. Dao, J. Li, A. M. Minor, Y. -L. Shen, Indentation across size scales and disciplines: Recent developments in experimentation and modeling, Acta Mater., 55 (2007) 4015-4039.

[32] B. Gutenberg, C. F. Richter, Magnitude and energy of earthquakes, Ann. Geofis., 9 (1956) 1-15.

[33] T. Ohmura, Collective motion of dislocation associated with local plasticity initiation and subsequent behavior in bcc metals, MS&T18, Columbus OH, 2018.

[34] W. C. Oliver, G. M. Pharr, An improved technique for determining hardness and elastic modulus using load and displacement sensing indentation experiments, J.

Mater. Res., 7 (1992) 1564-1583.

[35] K. Sekido, T. Ohmura, L. Zhang, T. Hara, K. Tsuzaki, The effect of interstitial carbon on the initiation of plastic deformation of steels, Mater. Sci. Eng. A, 530 (2011) 396-401.

[36] K. Durst, B. Backes, M. Goken, Indentation size effect in metallic materials: Correcting for the size of the plastic zone, Scripta Mater., 52 (2005) 1093-1097.

[37] M. Inamura, T. Suzuki, Evaluation of materials strength by ultra-micro-indentation, Seisan-Kenkyu, 42 (1990) 257-260.

Chapter 3 Effect of grain boundary on mechanical stability of metastable austenite

3.1 Introduction

As mentioned in chapter 1, austenite phase possesses higher mechanical stability with higher carbon content [1-4]. In TRIP-aided steels, the carbon atoms diffuse to austenite phase from the adjacent martensite during the quenching and tempering or partitioning treatments [5-7]. Moreover, the carbon atoms should be trapped by the dislocations near grain boundary inside the austenite grain. Thus, the carbon content decreases with increasing the distance from the grain boundary in a retained austenite grain resulting from an inhomogeneous distribution of carbon. There are a few reports on the mechanical stability of austenite phase; however, most of them deal with multiphase (including austenite, and martensite or ferrite) steels. In this sense of the complex effects of grain boundary constraint and carbon content, it is essential to study the mechanical behavior of single austenite phase without carbon, and understand the dependence of grain boundary on the mechanical stability since the grain size plays a crucial role [8-12].

The position of the indentation marks in the vicinity of grain boundary should be considered based on plastic zone. The size of plastic zone underneath an indentation mark is expectation that the strain field should be reflected by the contact area. Johnson spherical cavity model gives a direct relationship between the plastic zone radius r_{pz}, and the contact radius r_c [13], expressed as

$$\frac{r_{pz}}{r_c} = \left[\frac{E^* \tan\beta}{6\sigma_y(1-\nu)} + \frac{2}{3}\left(\frac{1-2\nu}{1-\nu}\right)\right]^{\frac{1}{3}} \tag{3.1}$$

where σ_y is the uniaxial yield strength, and the angle β is that between the indenter flank and the surface. The r_{pz} /r_c ratio, referred to the factor f, is implied within the limits of the analysis for a given indenter shape and material [14-17]. The plastic zone radius r_{pz} is larger than the contact radius r_c and the factor $f > 1$ for most metallic materials [18].

Figure 3.1 is a schematic illustration of the plastic zone around an indentation mark. Furthermore, the experiments and finite element simulations of the indentation process were performed using a Berkovich indenter, showing a reasonably good fit given by f =2.2 [19]. Here, it should be noted that the actual size of the plastic zone varies for different materials.

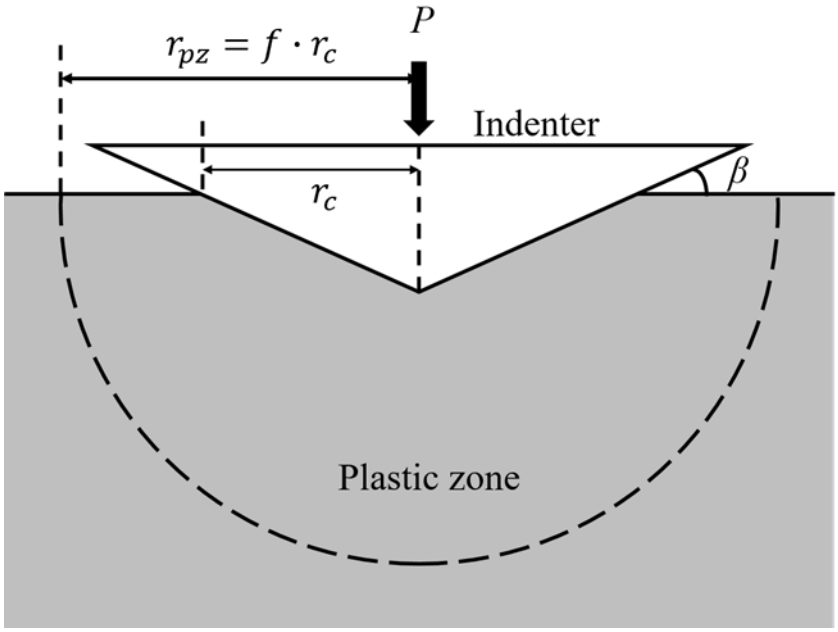

Figure 3.1 Schematic illustration showing the relationship between the radii of the plastic zone and the contact area.

To address these questions, nanoindentation combined with microstructural characterization using electron backscattered diffraction (EBSD) and transmission electron microscopy (TEM) is employed to investigate the effect of the austenite grain boundary, as well as the γ/α' interface, on the mechanical stability of austenite phase. The constraint by the austenite grain boundary on stress-induced martensitic transformation is discussed.

3.2 Experimental procedures

Fe-27Ni and Fe-30Ni steels were used in this chapter, and the chemical composition was presented in Table 3.1.

Table 3.1 Chemical composition in mass%.

Noted	Fe	C	Cr	Ni	Mn	Si
Fe-27Ni	Balanced	0.07	0.01	27.41	0.79	-
Fe-30Ni	Balanced	-	0.01	29.39	0.80	-

The Fe-27Ni and Fe-30Ni samples were solution-treated at 1473 K for 10.8 ks followed by cooling down to room temperature (293 K) in Ar gas flow. The Fe-27Ni samples consisted of above 98% austenite phase at room temperature, hereafter noted as sample Fe-27Ni-H. The M_s of the Fe-27Ni is approximately 272 K, which is calculated by Eq. 1.1 [20]. A portion of the Fe-27Ni samples was subjected to be subzero-treated at 243 K for 0.18 ks in the ethanol solution, using liquid nitrogen to keep temperature. Butterfly and lenticular martensite with a straight γ/α' interface were formed in the subzero-treated samples, referred to sample Fe-27Ni-S. The Fe-30Ni samples were cold-rolled with a reduction of 68% and then annealed at 1073 K for 1.8 ks under vacuum to obtain the stable austenite phase. The sample surfaces were prepared by mechanical grinding and finished by electrolytic polishing using the solution of 8 vol% perchloric acid, 73 vol% ethyl alcohol, 10 vol% butyl cellosolve, and 9 vol% distilled water under a voltage of 45 V at external cooling to remove the damaged layer. The microstructure characterization was conducted before nanoindentation tests, and the positions of indentation marks were confirmed after nanoindentation tests using a JEOL JSM-7000F field emission scanning electron microscopy (FESEM) equipped with a TSL detector for electron backscattered diffraction (EBSD) mapping, which was operated at an accelerating voltage of 20 kV

with a tilt angle of 70°. The scanning step size of 0.2~10 μm was used for EBSD mapping. Nanoindentation tests were carried out using a Hysitron TI 950 Triboindenter equipped with a Berkovich indenter, and the tip truncation was calibrated using a reference specimen of fused silica. Nanoindentation tests were performed at different positions of austenite and martensite in the mapped area. All the nanoindentation tests were set at a constant loading and unloading rate of 50 μN/s with a holding segment of 10 s under a load-control condition. Analyses for the tip calibration and the calculation of hardness were conducted using the Oliver and Pharr method [21]. The sample preparation for TEM observations of the cross-sectional view containing the indentation marks was carried out using a focused ion beam (FIB) milling. FIB milling was carried out using JEOL JEM-9320FIB and JIB-4000 with bulk-specimen holder and TEM-compatible holder, respectively operating at accelerating voltage of 5 kV, 10 kV, 30 kV. The surface was protected by carbon deposition to avoid any damage of the indentation mark area. After lift-out the sliced sample, it was fixed to a nano mesh in such a way. Then, the TEM sample was thinned from both sides to be ~100 nm in thickness. TEM observations were performed using a JEOL JEM-2100, which was operated at 200 kV.

3.3 Results

3.3.1 Mechanical behaviors of austenite and martensite

Figure 3.2(a) is phase map of the Fe-27Ni-S sample consisting of austenite and martensite that includes lenticular and butterfly martensite, presented in red and green, and the corresponding IQ map is shown in Fig. 3.2(b), respectively. Figs. 3.2(c), (d) and (e), (f) similarly show the microstructures in the Fe-30Ni and Fe-27Ni-H samples consisting of above 98% austenite, respectively.

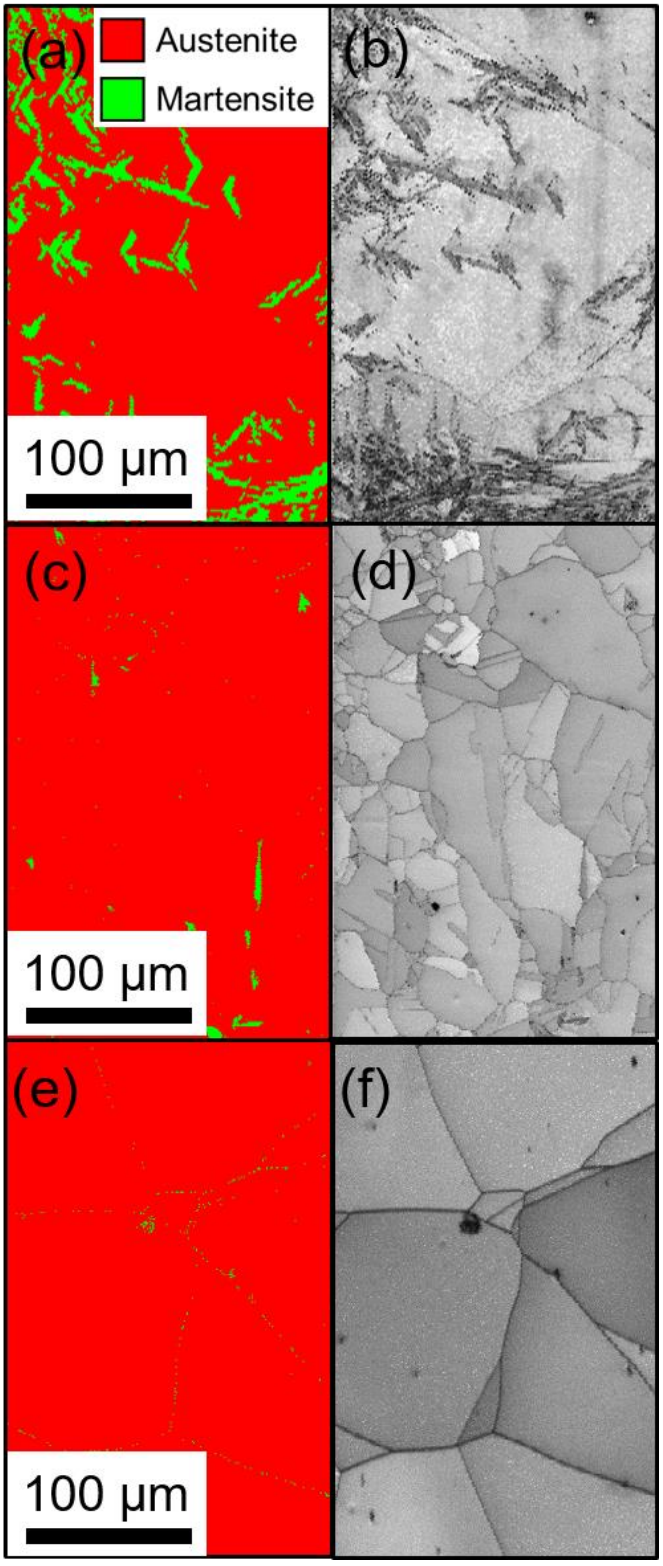

Figure 3.2 (a), (c), (e) Phase maps and (b), (d), (f) IQ maps showing the microstructures in the (a), (b) Fe-27Ni-S, (c), (d) Fe-30Ni, and (e), (f) Fe-27Ni-H samples.

Figure 3.3(a) shows the typical *P* versus *h* curves that obtained individually for butterfly martensite in the Fe-27Ni-S, stable austenite in the Fe-30Ni and metastable austenite in the Fe-27Ni-H by nanoindentation tests with a peak load of 2000 μN. It is noted that the nanohardness is significantly higher for the martensite than that for the austenite. As mentioned in chapter 2, the *P* versus *h* curve is converted to the *P/h* versus *h* plot to quantitatively evaluate the value of key parameter *a* in the loading process. Figures 3.3(b), 3.3(c) and 3.3(d) show the corresponding loading segment of *P/h* versus *h* plots for butterfly martensite, stable austenite, and metastable austenite, respectively. The slope values for the martensite in the Fe-27Ni-S and the stable austenite in the Fe-30Ni hold almost constant suggesting a single deformation mode during the plastic deformation, whereas the metastable austenite phase in the Fe-27Ni-H shows a knick at a middle of loading segment around $h \sim 70$ nm, suggesting double stages with a low value of the slope *a* in stage I and a higher value in stage II. It should be noted that the slope *a* value of stage II (0.035 μN/nm^2) in the Fe-27Ni-H is relatively close to that of the martensite (0.041 μN/nm^2). As described above, the slope *a* is associated with plastic deformation mechanisms, thus, the change in slope *a* should be the consequence of a change in the dominant deformation mode. For metastable austenite in the Fe-27Ni-H, stage I is presumably governed by indentation-induced martensitic transformation, and then followed by dislocation motion in the transformed martensite in stage II.

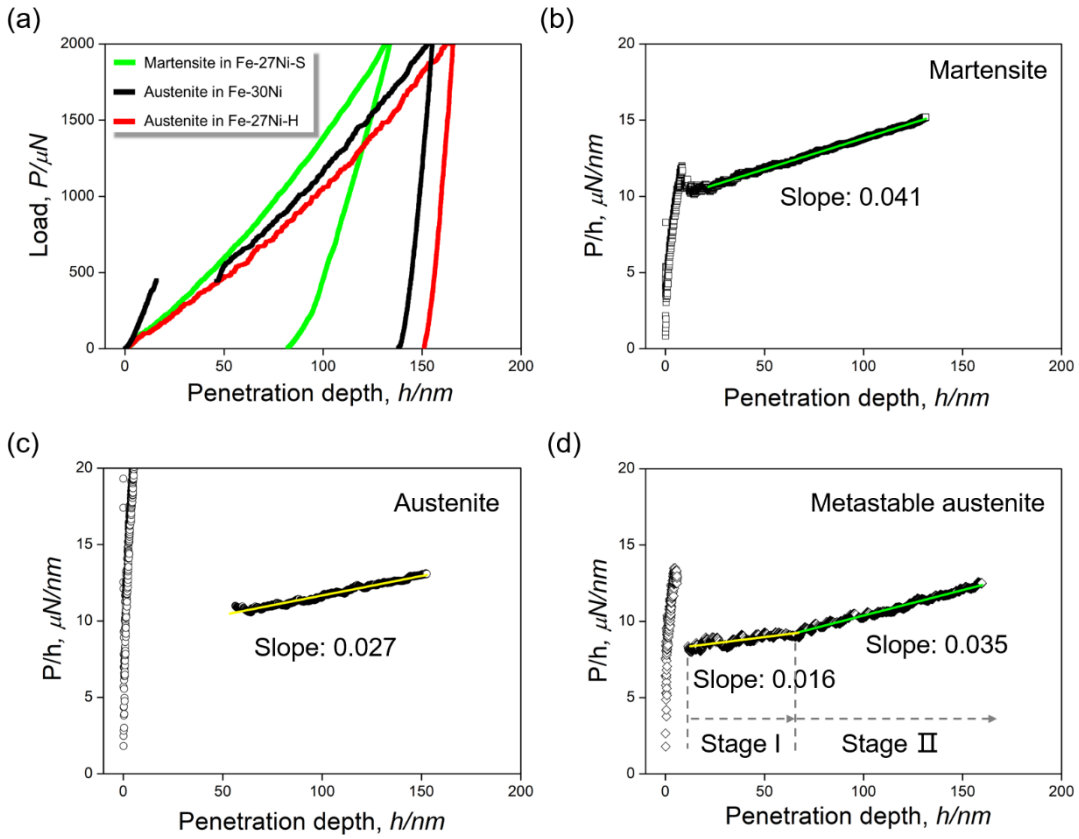

Figure 3.3 (a) Typical *P* versus *h* curves for martensite (green) in the Fe-27Ni-S, stable austenite (black) in the Fe-30Ni, and metastable austenite (red) in the Fe-27Ni-H. The corresponding loading segment of *P/h* versus *h* plots for (b) the martensite in the Fe-27Ni-S, (c) the austenite phase in the Fe-30Ni, and (d) the metastable austenite phase in the Fe-27Ni-H.

3.3.2 Effect of grain boundary and γ/α' interface on mechanical stability of metastable austenite

Nanoindentation tests were respectively performed at the different positions in the austenite grains, such as grain interior and the vicinity of grain boundary in the Fe-27Ni-H and the vicinity of γ/α' interface in the Fe-27Ni-S with a peak load of 2000 μN. EBSD measurements were taken after the nanoindentation tests. Figures 3.4(a) and 3.4(c) are phase maps respectively obtained from the Fe-27Ni-H and Fe-27Ni-S, here, red indicates austenite and green indicates martensite. Figures 3.4(b) and 3.4(d) are the corresponding IQ maps. The phase and IQ maps show the indentation marks penetrated respectively at grain interior, the vicinity of grain boundary, and γ/α' interface that are

outlined by the pink, orange, and blue circles and arrows in the IQ maps. The distance of all indentation marks from grain boundary and γ/α' interface are smaller than 2 μm, in which the boundaries are presumably within the plastic zone. Besides, the indentation-transformed martensite cannot be detected in the regions surrounding the indentation marks in the phase maps even though under high magnification. Therefore, the observations on the microstructure around the indentation marks will be carried out using TEM in a cross-sectional view, which are shown in section 3.3.3.

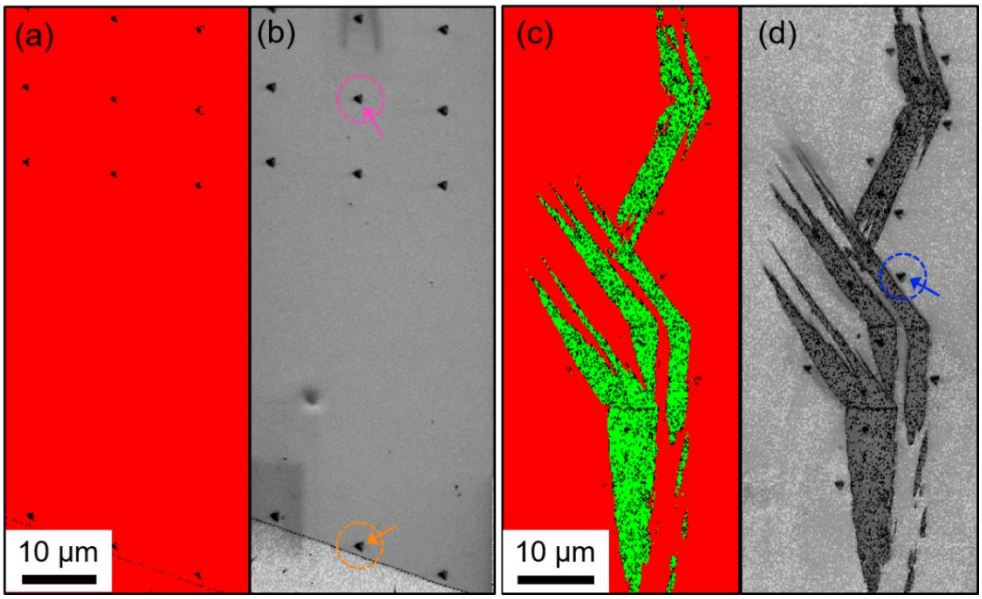

Figure 3.4 Phase and IQ maps obtained after the nanoindentation tests for the different positions. (a), (b) Grain interior and the vicinity of grain boundary respectively outlined by the pink and orange circles and arrows in the Fe-27Ni-H, and (c), (d) the vicinity of the γ/α' interface outlined by the blue circle and arrow in the Fe-27Ni-S. Austenite and martensite respectively presented in red and green.

The converted loading segment of *P/h* versus *h* plots for the grain interior, the vicinity of grain boundary in the Fe-27Ni-H and the vicinity of γ/α' interface in the Fe-27Ni-S are demonstrated in Fig. 3.5. All the three *P/h* versus *h* plots show a knick point in the middle of the plastic deformation, suggesting double stages with a low value of the slope *a* in stage I and a higher value in stage II. The knick point during the plastic deformation can be defined as the transition load P_t or depth h_t. Compared to the three plots, it is found that the values of the slope *a* in stage I and the transition load P_t are highest in the vicinity of the γ/α' interface.

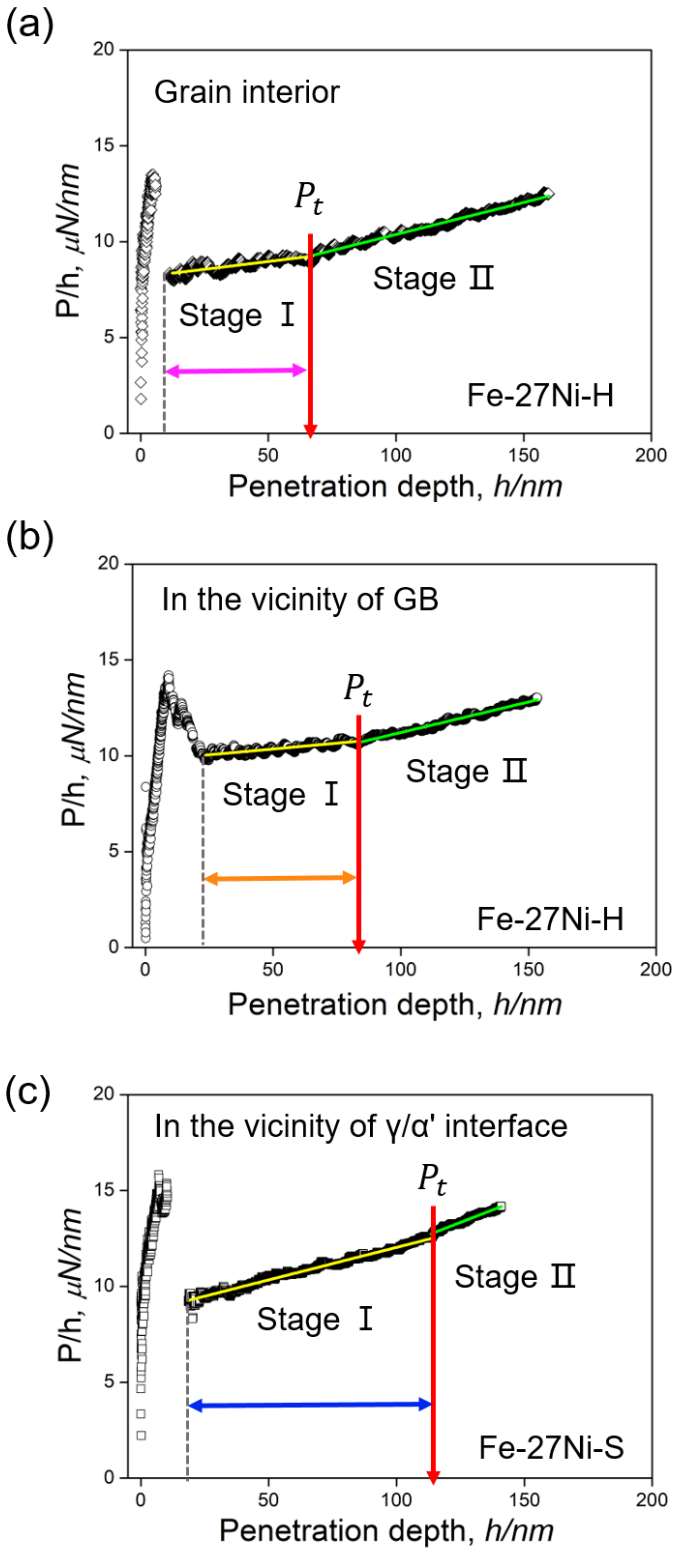

Figure 3.5 The loading segment of *P/h* versus *h* plots for the different positions. (a) Austenite grain interior in the Fe-27Ni-H, (b) the vicinity of austenite grain boundary in the Fe-27Ni-H, (c) the vicinity of γ/α' interface in the Fe-27Ni-S. All the plots exhibit the two stages of I (yellow) and II (green).

To reach a reliable conclusion, about 50 data points were obtained for each position. Figure 3.6(a) is the average values of the slope a in stage I and the transition load P_t for the three different positions, respectively. The results show a tendency that the average values of the slope a in stage I and the transition load P_t become lower at the vicinity of the γ/α' interface, the austenite grain boundary, and the austenite grain interior in turn. In addition, the difference in the average slope a value between the vicinity of grain boundary and the grain interior is 0.012 μN/nm^2 for metastable austenite in the Fe-27Ni-H, which is much higher than ferrite (Δa: 0.002 μN/nm^2) and stable austenite (Δa: 0.004 μN/nm^2) as shown in Fig. 2.9. Moreover, the difference in the average slope a value is relatively higher for the γ/α' interface. Figures 3.6(b) and 3.6(c) are the plots of the slope a in stage I and the transition load P_t as a function of the distance D_{GB} of the center of the indentation mark from the austenite grain boundary. The values of the slope a in stage I and the transition load P_t decrease with increasing the distance D_{GB}. More specially in Fig. 3.6(c), the extrapolation of the three fitting lines for the transition load P_t crosses at the same D_{GB}, which is equal to the average value of the transition load P_t for the austenite grain interior (the black solid diamond in Fig. 3.6(c), which is obtained from Fig. 3.6(a)). The results suggest that the closer to the austenite grain boundary exhibits higher resistance to stress-induced martensitic transformation. Although the scattering data are shown in the plot of the slope a in stage I, it is presumably due to different angle of grain boundary and orientation of the neighboring grains.

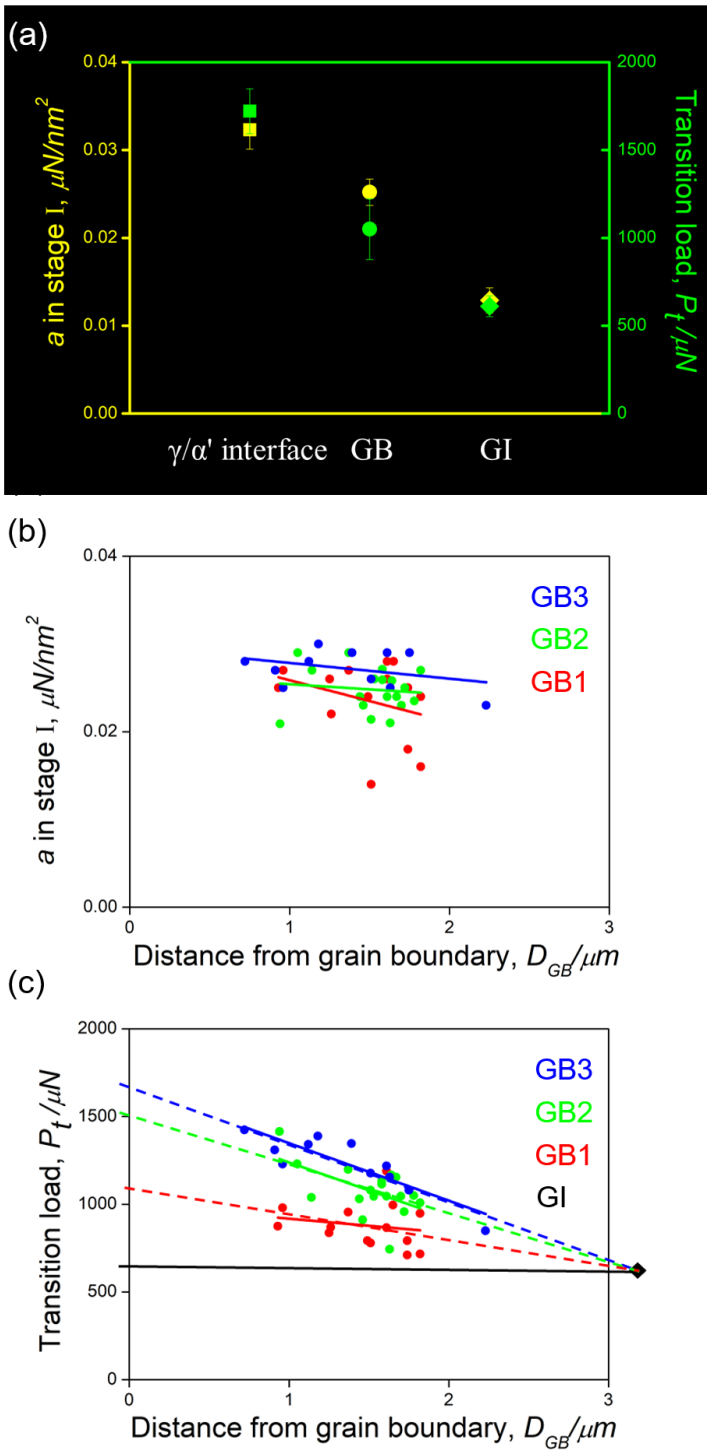

Figure 3.6 (a) The average values of the slope *a* in stage I and the transition load P_t at the different positions. (b) The slope *a* in stage I and (c) the transition load P_t plotted as a function of the distance of the indentation marks from austenite grain boundary D_{GB}.

The average value of the slope *a* in stage II, which corresponds to the indentation-transformed martensite in the Fe-27Ni-H, is lower than that of the subzero-quenched martensite (butterfly martensite) in the Fe-27Ni-S as shown in Fig. 3.7(a). Furthermore, the slope *a* values of butterfly martensite in the Fe-27Ni-S tend to two different values. One is around 0.04 μN/nm^2, which is believed to be the untwinned region of the butterfly martensite. The other is a range approximately from 0.06 to 0.09 μN/nm^2, which should be the twinned region. Besides, the average nanohardness of the twinned region ($\overline{H_n}$=3.90 GPa) is higher than that of the untwinned region ($\overline{H_n}$=3.01 GPa) due to the different substructures, which is the same with the previous paper reported in the lenticular martensite in Fe-33Ni [22]. Figure 3.7(b) is SPM image showing the indentation marks in the untwinned and twinned regions respectively outlined by the blue and pink dashed circles penetrated inside the butterfly martensite in the Fe-27Ni-S. The schematic illustration in Fig. 3.7(c) shows the substructures of the butterfly martensite in the Fe-27Ni-S, which include twinned region (the region normally near the outer surface), and the untwined region (the region normally near the inner surface) consisting of a high density of dislocations. Sometimes, the indentation mark at the region near the outer surface indicated by the blue arrow in Fig. 3.7(b) is distinguished as one in the untwined region, which is dependent on the nanohardness H_n. It is presumably due to the density of twins at the outer surface, however, it is difficult to check through the SPM image.

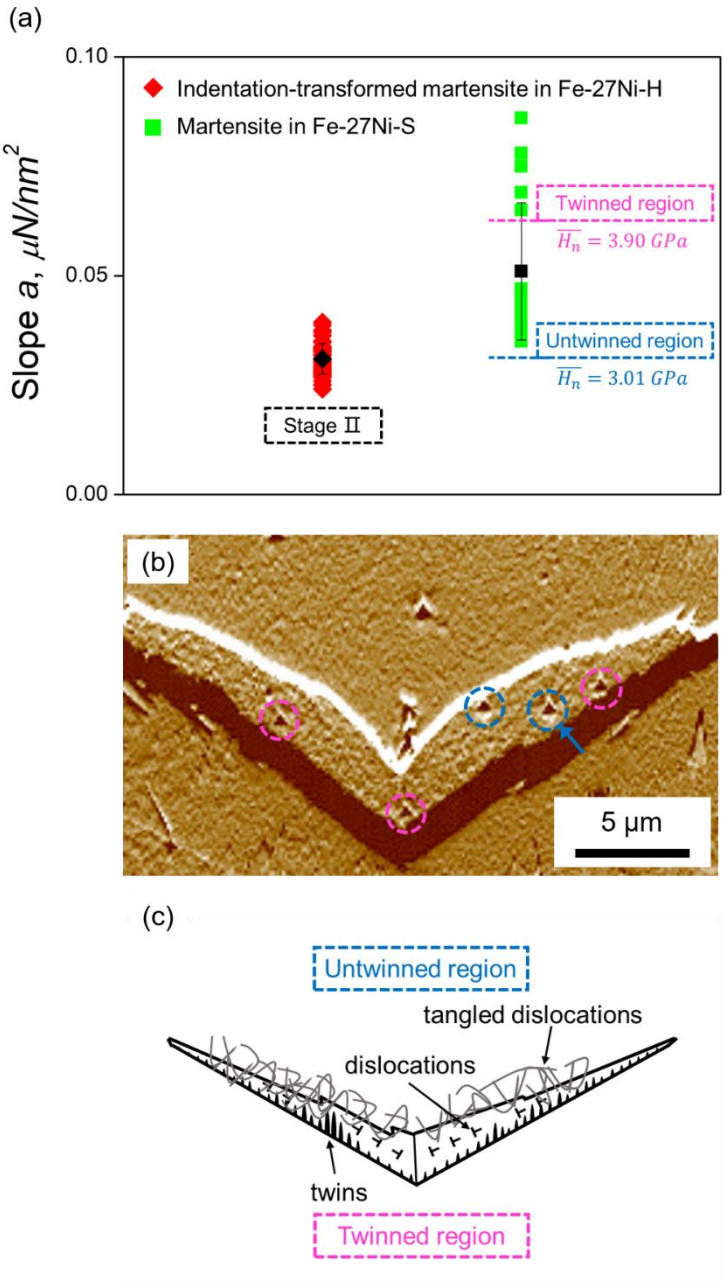

Figure 3.7 (a) The plot of the slope *a* values for the indentation-transformed martensite in the Fe-27Ni-H and the subzero-quenched martensite (butterfly martensite) in the Fe-27Ni-S; (b) SPM image of the indentation marks in the untwinned and twinned regions respectively outlined by the blue and pink dashed circles penetrated inside the butterfly martensite; (c) schematic illustration of the substructures of the butterfly martensite.

3.3.3 TEM observation of the microstructures underneath the indentation marks

The internal stresses are induced by martensitic transformation during the subzero treatment, and then high local internal stresses are relaxed by the generation of dislocations in the austenite phase, and dislocation density is believed to be higher in the vicinity of the γ/α' interface than grain interior. Therefore, the dislocation density may bring the additional influential factor in this study. This is why the austenite grain boundary is firstly chosen for subsequent TEM observations to make clear the boundary effect on the mechanical stability of austenite phase although the highest resistance to stress-induced martensitic transformation exists in the vicinity of the γ/α' interface.

Figures 3.8(a) and (b) show the phase and IQ maps of an austenite grain in the Fe-27Ni-H sample, in which the austenite and martensite are respectively shown in red and green. Figure 3.8(c) is the frame of the SEM image corresponding the region of the black dashed rectangle shown in Fig. 3.8(b), which is taken after the nanoindentation test with a peak load of 1000 μN, showing the indentation mark penetrated in the vicinity of the austenite grain boundary. Figure 3.8(d) is the SPM image of the indentation mark. It is subsequently employed for TEM observation of the microstructure underneath the indentation mark. The position of the sliced sample and the plastic zone are respectively indicated by the black dashed rectangle and the green dashed circle in Fig. 3.8(d). The radius of plastic zone r_{pz} highlighted by a green dashed arrow is evaluated by the relationship [13-17] of the factor f times the contact radius r_c highlighted by the red solid arrow, herein, the f=2.2 for a Berkovich indenter [19] employed in this work. The corresponding P versus h curve and converted loading segment of P/h versus h plot are shown in Figs. 3.8(e) and 3.8(f), respectively. The P/h versus h plot shows the end of stage I or approximation at the maximum applied load since the slope a value in the plot is nearly equal to the average slope a value in stage I of the austenite grain boundary shown in Fig. 3.6(a).

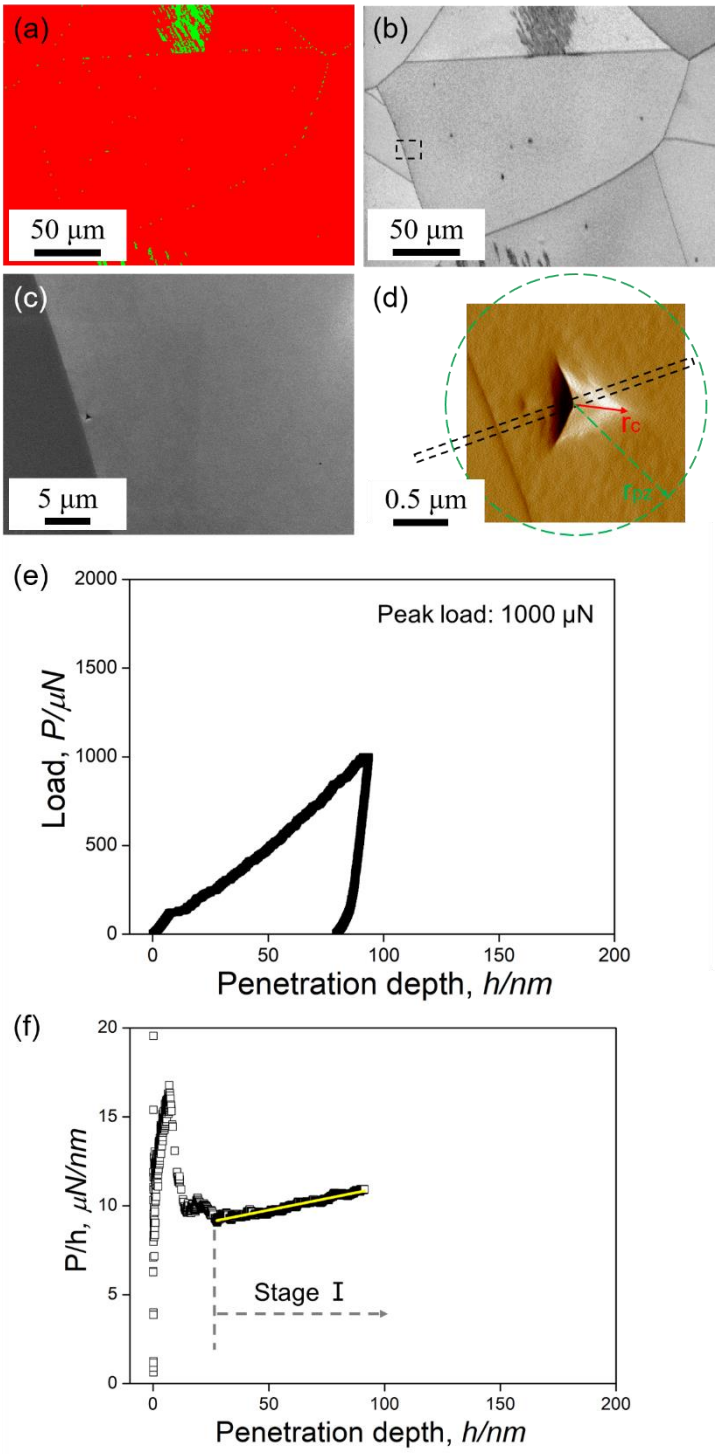

Figure 3.8 (a) Phase and (b) IQ maps of an austenite grain in the Fe-27Ni-H sample, and the austenite and martensite respectively shown in red and green. (c) The frame of SEM image corresponding the region of the black dashed rectangle in (b), taken after the nanoindentation test with a peak load of 1000 μN. (d) SPM image of the indentation mark. The position of FIB milling outlined by the black dashed rectangle, subsequently employed for TEM observations of the microstructures underneath the indentation mark. The plastic zone outlined by the green dashed circle. (e) The corresponding *P* versus *h* curve and (f) loading segment of *P/h* versus *h* plot.

Figure 3.9(a) is TEM bright-field (BF) image of a cross-sectional view of the microstructure underneath the indentation mark, where the austenite grain boundary is evidently shown. Figure 3.9(b) is the selected area electron diffraction (SAED) pattern obtained from the selected region outlined by the white dashed circle shown in Fig. 3.9(a). Figure 3.9(c) is the dark-field (DF) image taken from the bcc (1-10) spot in Fig. 3.9(b). The SAED pattern in Fig. 3.9(b) indicates that the microstructure consists of two different lattice structures of the transformed martensite (bcc) and the original austenite (fcc). Another possibility is that the weak spots are originated from some kinds of iron-nickel oxide like $(FeNi)_xO_x$. For a double-checking, both the cross-sectional surface of this sample was re-polished a little bit by FIB milling. The double-checked result of the diffraction pattern taken from the same selected region is shown in Fig. 3.9(d), which is the same as the previous diffraction pattern as shown in Fig. 3.9(b). Furthermore, the measured d-spacing of bcc {-110} and fcc {220} is nearly equal to the theoretical d-spacing of bcc and fcc structures respectively. Therefore, it can be concluded that the the lattice structures consist of bcc and fcc, which are recognized as α' and γ respectively. Figure 3.9(e) represents schematic illustration of the diffraction pattern for bcc [110] and fcc [111] lattice structures respectively indicated by the green and red spots that corresponds to the SAED pattern in Fig. 3.9(b). The result of analysis in the SAED pattern clarifies that the relation between these two patterns satisfies with the K-S orientation relation. The results suggest that the microstructure underneath the indentation mark is a mixture of the indentation-transformed martensite and the original austenite. Besides, no martensite is found to produce at the left side of grain boundary in the adjacent grain. Figure 3.9(f) is a schematic illustration of the microstructure underneath the indentation mark.

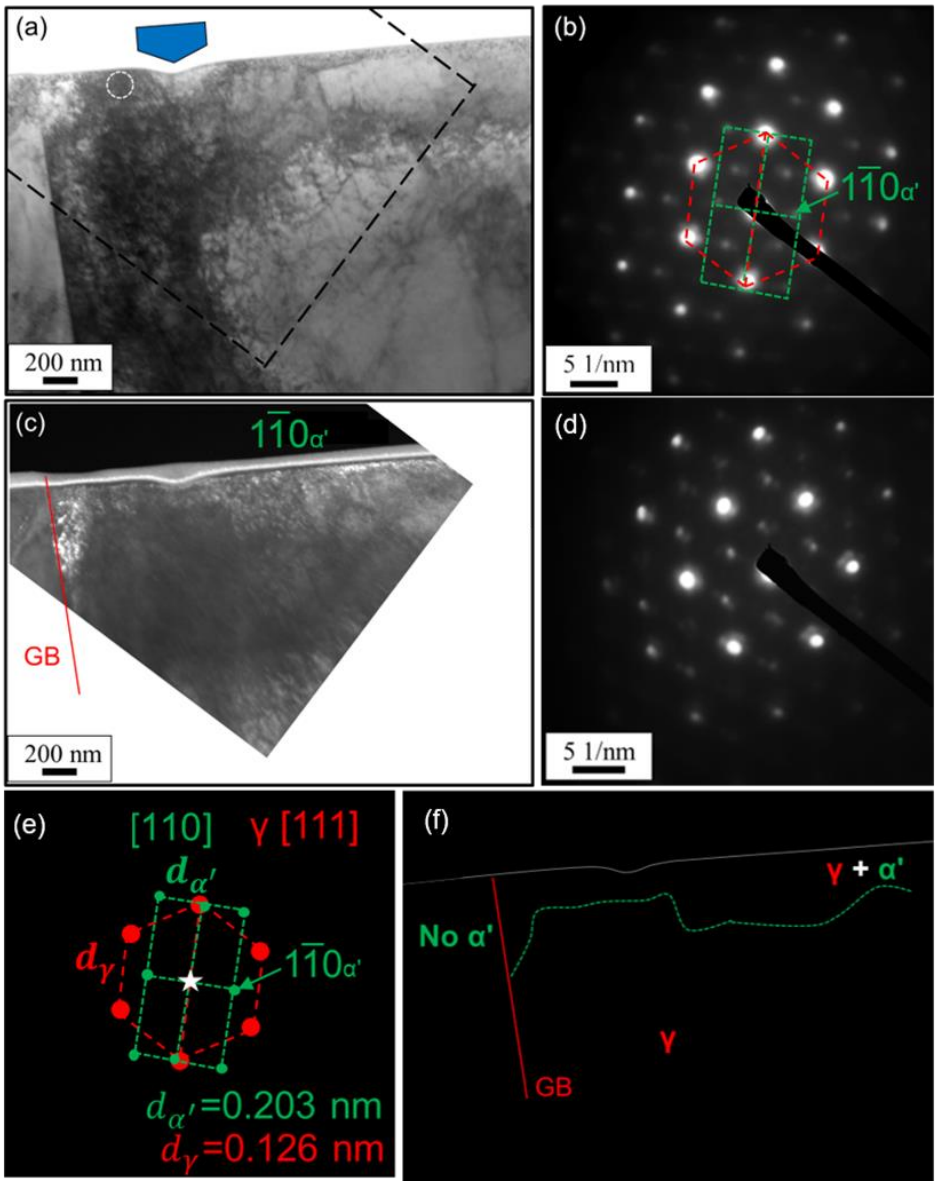

Figure 3.9 (a) TEM bright-field image of a cross-sectional view of the microstructure below the indentation mark. (b) The selected area electron diffraction (SAED) pattern obtained from the region outlined by the white dashed circle as shown in (a). (c) The frame of dark-field image taken from bcc (1-10), corresponding to the region of the black dashed rectangle shown in (a). (d) The double-checked SAED pattern obtained from the same selected region in (a) for the re-polished by FIB. (e) Schematic illustration of the SAED pattern, in which the green and red spots indicate bcc [110] and fcc [111] lattice structures, respectively, and the relation satisfies with the K-S orientation. (f) Schematic illustration of the microstructure underneath the indentation mark.

The microstructural characterization by TEM is also carried out for another indentation mark in the different austenite grain to make sure that the indentation-induced martensitic transformation occurs in stage I during the loading process. Figure 3.10(a) is phase, IQ and IPF maps of austenite grains in the Fe-27Ni-H obtained by SEM-EBSD, where the austenite is shown in red. The nanoindentation position in the vicinity of an austenite grain boundary is indicated by the black arrow in the IPF map. Figures 3.10(b) and 3.10(c) are SPM images taken after the nanoindentation test with a peak load of 500 μN, showing the indentation mark in the vicinity of the austenite grain boundary. The position of FIB milling is outlined by the black dashed rectangle in the SPM images, in which the sliced sample is subsequently employed for TEM observations. Figures 3.10(d) and 3.10(e) are the corresponding P versus h curve and loading segment of P/h versus h plot, respectively. The applied load is ceased at 500 μN, which is lower than the average value of the transition load P_t, therefore the microstructure presumably corresponds to the stage I for metastable austenite.

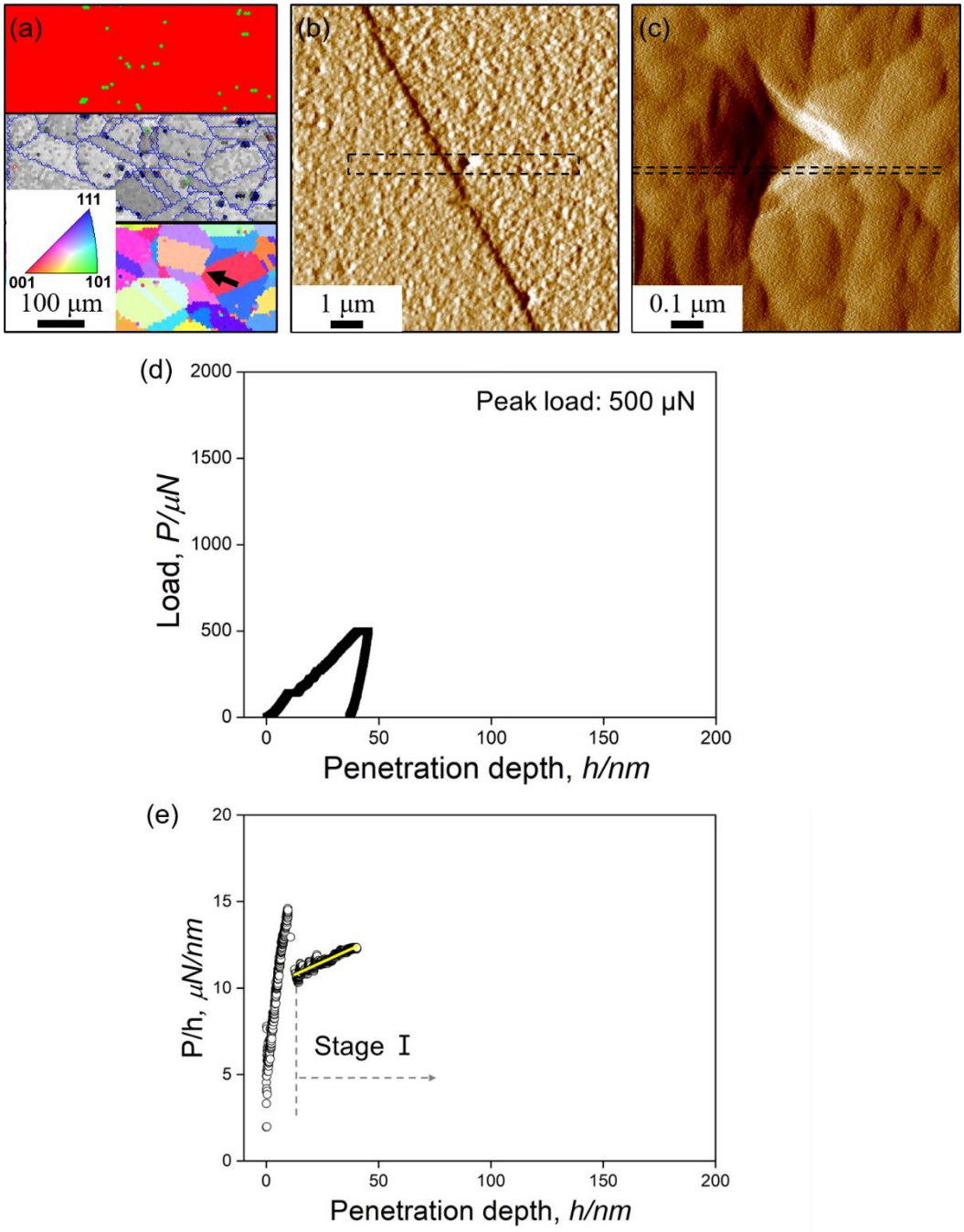

Figure 3.10 (a) Phase, IQ and IPF maps of austenite in the Fe-27Ni-H sample obtained by SEM-EBSD, where the austenite shown in red and the position of the indentation mark penetrated in the vicinity of the austenite grain boundary indicated by the black arrow in the IPF map. (b) and (c) SPM images taken after the nanoindentation test with a peak load of 500 μN, showing the indentation mark penetrated in the vicinity of the austenite grain boundary. The position of FIB milling is outlined by the black dashed rectangle in the SPM images. (d) and (e) The corresponding *P* versus *h* curve and loading segment of *P/h* versus *h* plot.

Figure 3.11(a) shows TEM BF image of a cross-sectional view of the microstructure underneath the indentation mark. Figure 3.11(b) is SAED pattern obtained from the region 1 outlined by the white dashed circle shown in Fig. 3.11(a). The schematic illustration of the SAED pattern is presented in Fig 3.11(c), which is also overlapped on Fig. 3.11(b). The SAED pattern for the region 1 consists of bcc [112] lattice structure (α') and fcc [10-1] lattice structure (γ) which are indicated by the green and red spots, respectively in Fig. 3.11(c), and their orientation relation is in concordance with the N-W orientation relation. Moreover, the measured d-spacing of bcc {-110} and fcc {220} is respectively equivalent to their theoretical d-spacing values. Figure 3.11(d) is DF image taken from the bcc (0-11) spot that is indicated by the green arrow in Fig. 3.11(b). The results suggest that the microstructure of the region 1 is a mixture of the indentation-transformed martensite and the original austenite. Furthermore, Fig. 3.11(e) shows the SAED pattern of fcc [135] zone axis for the region 2 outlined by the white dashed circle in Fig. 3.11(a), and Fig. 3.11(f) represents the corresponding DF image taken from the fcc (2-42) spot, respectively. The region 2 in Fig. 3.11(a) only exhibits the austenite phase. Figure 3.11(g) is a schematic illustration of the microstructure underneath the indentation mark. The indentation-transformed martensite is not detected in the adjacent grain in the right-upper corner on the image.

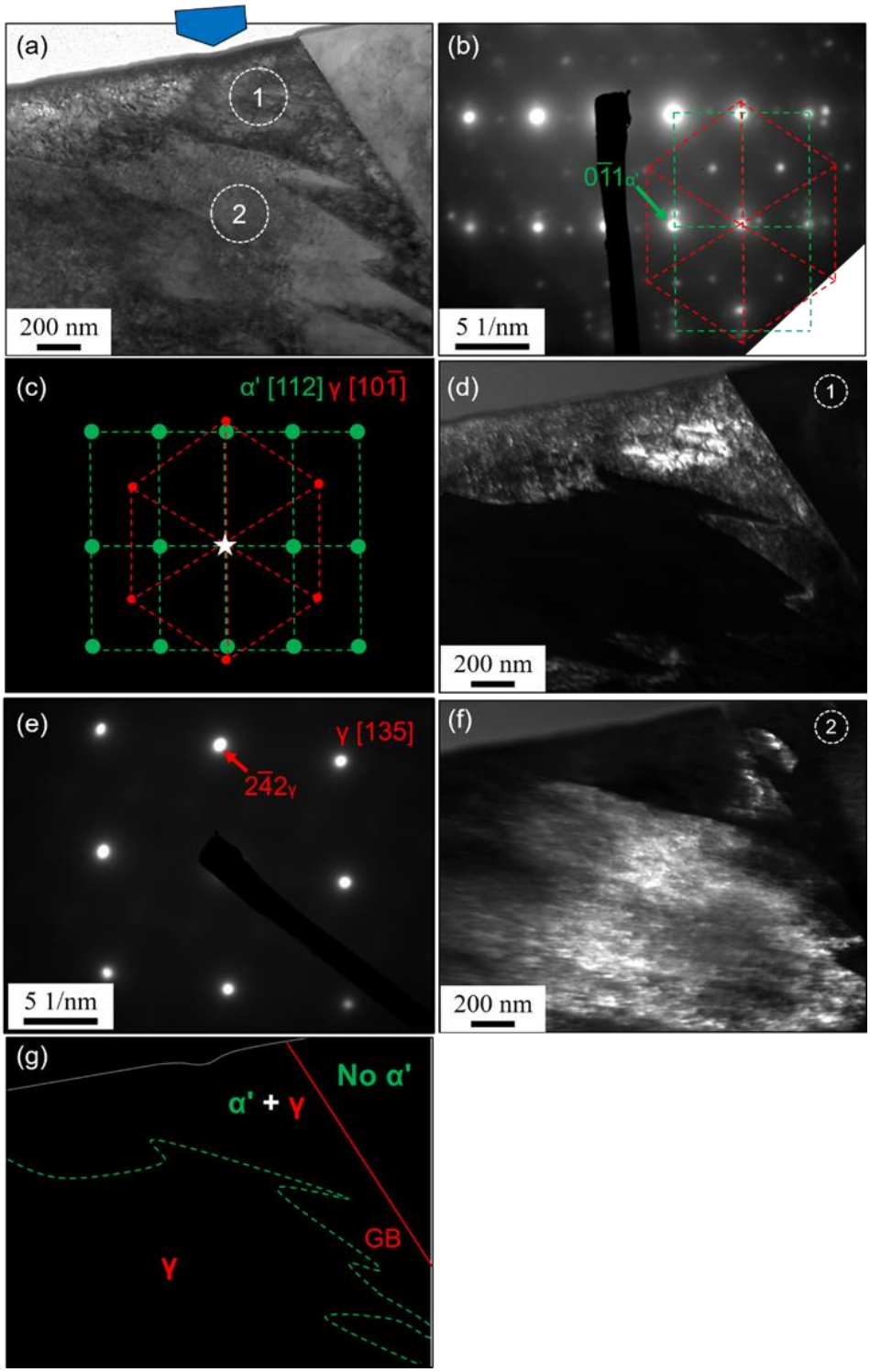

Figure 3.11 (a) TEM BF image showing a cross-sectional view of the microstructure underneath the indentation mark. (b) SAED pattern obtained from the region 1 outlined by the white dashed circle in (a). (c) Schematic illustration of the SAED pattern of (b), where green and red spots respectively indicate bcc [112] and fcc [10-1] lattice structures. (d) DF image taken from bcc (0-11). (e) SAED pattern of fcc [135] for the region 2 outlined by the white dashed circle in (a). (f) DF image taken from fcc (2-42). (g) Schematic illustration of the microstructure underneath the indentation mark.

The presence of the transformed martensite underneath the indentation marks in both austenite grains in Figs. 3.9 and 3.11 suggests that the indentation-induced martensitic transformation occurs in stage I of the *P/h* versus *h* plot during the loading process. Additionally, there is no martensite formed at the region close to grain boundary in the adjacent austenite grain, which indicates that the constraint by austenite grain boundary acts like strong wall to suppress the volume expansion of martensitic transformation during nanoindentation.

3.4 Discussion

As mentioned in chapter 2, the slope *a* in the *P/h* versus *h* plot is correlated to plastic deformation behaviors. For the metastable austenite phase in the Fe-27Ni-H, the presence of the transformed martensite underneath the indentation mark, in which nanoindentation behavior is related to stage I in the *P/h* versus *h* plot, definitively corroborates that stress-induced martensitic transformation occurs in stage I. Therefore, the change in the slope *a* in the plastic deformation segment of the *P/h* versus *h* plot is believed to be the consequence of a change in the dominant deformation mode, where the stage I with the low flow stress is dominated by the stress-induced martensitic transformation and the stage II with higher flow stress is governed by a dislocation glide motion in the transformed martensite. This is presumed based on the nanoindentation behaviors and the microstructural characterizations.

In addition, the nanoindentation result for the martensite in the Fe-27Ni-S demonstrates a single stage during the plastic deformation, which is related to slip deformation of dislocations. Moreover, the austenite phase in the Fe-30Ni is stable against the stress-induced martensitic transformation, and thus merely holds dislocation motion mode during the plastic deformation.

The nanoindentation results indicate that the average values of the slope *a* in stage I and the transition load P_t in the vicinity of the austenite grain boundary and the γ/α'

interface are higher than that at the austenite grain interior, which suggests that the resistance by the austenite grain boundary and γ/α' interface against stress-induced martensitic transformation is higher than grain interior. More specially, in the case of grain boundary, the values of the slope a in stage I and the transition load P_t show a tendency, which decrease with increasing the distance D_{GB}. It suggests that the constraint by the austenite grain boundary against martensitic transformation stabilizes austenite grain, which is in agreement with the TEM observations that stress-induced martensitic transformation with volume expansion is inhibited by the austenite grain boundary.

Grain boundary and γ/α' interface have the constraint effect on martensitic transformation, which may improve macroscopic mechanical properties in another mechanism of strain hardening. One conventional consented mechanism for strain hardening effect in the TRIP-aided steels is caused by the formation of a transformed martensite that is harder than an austenite, which is based on rule of mixture. In addition to the strain hardening effect, another mechanism may take place at the grain boundaries to make strain hardening as well. When the martensitic transformation initiates at a certain stress, the transformation is terminated at a grain boundary due to the constraint effect. At subsequent straining, a higher stress is required for another transformation to happen at a different site. Eventually, the stress gradually increases when the transformation reaches to completion in a whole sample, meaning a significant strain hardening in macroscopic scale. We may have a grain size effect on the strain hardening effect based on the idea. Assuming that there are two samples with the same volume fraction of austenite phase but different grain size, if a first event of transformation occurs at the same stress in the two samples, the volume of the transformed martensite is higher in the coarse grain than in the fine grain because transformation expands easier in the larger grain interior. A subsequent transformation should occur at a higher stress level as described above, and another larger volume of martensite is formed in the larger austenite again. After several steps of the events, whole volume of the austenite transforms into martensite. Since the fine grain has more

grain boundaries than the coarse grain does, the sample with the fine grains goes through several steps to complete the transformation in the whole volume at higher stress level whereas it completes at a lower stress in the coarse grain sample, which leads to increase in flow stress in the fine grain size. Therefore, finer austenite grain size makes presumably a higher effect on strain hardening.

The average value of the slope *a* at grain interior is lower in stage I of the Fe-27Ni-H than that in plastic deformation segment of the Fe-30Ni, suggesting that a critical stress for the martensitic transformation in the Fe-27Ni-H is lower than that for the dislocation glide in the Fe-30Ni. Additionally, the difference in the average values of the slope *a* between the vicinity of grain boundary and grain interior in the Fe-27Ni-H is higher than that in the Fe-30Ni, indicating that the grain boundary has significant resistance to the stress-induced martensitic transformation in the metastable austenite rather than that to the dislocation-grain boundary interaction in the stable austenite.

The TEM observations of the microstructure underneath the indentation marks show a mixture of the indentation-transformed martensite and the original austenite. Therefore, the measured nanohardness in stage II presumably includes the hardness of the two phases. Since the hardness of the austenite phase is lower than the martensite as shown in Fig. 3.3(a), the slope *a* of stage II in the Fe-27Ni-H is slightly lower than that of the untwinned region of butterfly martensite in the Fe-27Ni-S as shown in Fig. 3.7(a).

The autocatalytic effect of martensitic transformation is that a grown martensite can trigger other neighboring unstable martensitic embryos to become stable nuclei for further nucleation and growth during an on-going process. The internal stresses generated by an original martensite are relaxed by the formation of the secondary martensite. However, in the case of the Fe-27Ni-S, the martensite is formed during the subzero-quenched process, the internal stresses have already been relaxed by the generation of dislocations at the γ/α' interface. Therefore, the indentation-induced martensitic transformation in the austenite grain near the pre-transformed martensite is a different case compared with the autocatalysis of martensitic transformation during

an on-going process. In the present study, the values of the slope a in stage I and the transition load P_t are higher for the γ/α' interface than the γ/γ boundary, which means that the mechanical stability is higher for austenite near the γ/α' interface than that near the γ/γ boundary. Since the slope a value of subzero-quenched martensite in the Fe-27Ni-S is relatively higher than that of austenite as shown in Fig. 3.3. The constraint effect which is from the surrounded martensite is stronger than that from the surrounded austenite.

The conflicting effects of grain size on austenite mechanical stability during tensile deformation are described in section 1.3, where one indicates that the mechanical stability increases with decreasing austenite grain size, and another demonstrates that the mechanical stability is independent on austenite grain size. However, the present results of grain boundary on the mechanical stability show a clear decreasing trend inversely as the distance D_{GB}. It is presumably due to different stress distributions existed in nanoindentation and tensile deformation. The distribution of the applied stress during tensile deformation is homogeneous in the austenite grain, thus, the applied stress at grain boundary may initiate martensitic transformation because the grain boundary is one of the favorable and suitable nuclei for martensitic transformation. Sometimes, the competitive mechanisms take place at grain boundary, initiating or retarding the transformation. Whereas, the stress distribution during nanoindentation is different for grain interior and the vicinity of grain boundary. At grain interior, martensitic transformation occurs and grows without limitation. In the vicinity of grain boundary, the transformation also occurs at grain interior, but the volume expansion of the martensite is inhibited by grain boundary, thus, the grain boundary plays a role in suppressing the transformation only. The nanoindentation results in this study individually demonstrate the constraint effect of grain boundary on the mechanical stability, in which the mechanical stability increases inversely as the distance D_{GB}.

3.5 Conclusions

The investigation on the effect of grain boundary on the mechanical stability of individual austenite grains in the Fe-27Ni steel was performed using a combination of nanoindentation, SEM/EBSD, and TEM. From the obtained results, the following conclusions can be drawn.

(1) The martensite in the Fe-27Ni-S and the stable austenite in the Fe-30Ni exhibit a single plastic deformation stage during the loading process in the *P/h* versus *h* plots, corresponding to the slip deformation. Whereas, the metastable austenite in the Fe-27Ni-H shows double plastic deformation stages, where the stage I is dominated by stress-induced martensitic transformation, and the stage II is governed by a dislocation glide motion in the transformed martensite.

(2) The *P/h* versus *h* plots hold higher flow stress in stage I with a higher transition load P_t for the γ/α' interface and the austenite grain boundary than those for the austenite grain interior. Moreover, the transition load P_t increases inversely as the distance from the γ/α' interface_and grain boundary. It suggests that grain boundary actively inhibits stress-induced martensitic transformation, resulting in high mechanical stability of metastable austenite.

(3) The indentation-transformed martensite underneath the indentation mark in austenite grains is observed in TEM micrographs, which confirms that the stress-induced martensitic transformation dominates the behavior in stage I during the loading process. There is no martensite formed at the region close to grain boundary in the adjacent austenite grain, which indicates that the grain boundary suppresses the martensitic transformation. The microstructural characterizations are in agreement with the results of the mechanical behaviors obtained by nanoindentation.

References

[1] R. Blonde, E. Jimenez-Melero, L.Zhao, J. P. Wright, E. Bruck, S.V. D. Zwaag, N.

H. V. Dijk, High-energy X-ray diffraction study on the temperature-dependent mechanical stability of retained austenite in low-alloyed TRIP steels, Acta Mater., 60 (2012) 565-577.

[2] M. De Meyer, D. Vanderschueren, B. C. De Cooman, The influence of the substitution of Si by Al on the properties of cold rolled C-Mn-Si TRIP steels, ISIJ Int., 39 (1999) 813-822.

[3] E. Jimenez-Melero, N. H. V. Dijk, L. Zhao, J.Sietsma, S. E. Offerman, J. P. Wright, S. V. D. Zwaag, Characterization of individual retained austenite grains and their stability in low-alloyed TRIP steels, Acta Mater., 55 (2007) 6713-6723.

[4] G. Reisner, E. A. Werner, P. Kerschbaummayr, I. Papst, F. D. Fischer, The modeling of retained austenite in low-alloyed TRIP steels, JOM, 49 (1997) 62-65.

[5] J. Speer, D. K. Matlock, B. C. De Cooman, J. G. Schroth, Carbon partitioning into austenite after martensite transformation, Acta Mater., 51 (2003) 2611-2622.

[6] A. J. Clarke, J. G. Speer, M. K. Miller, R. E. Hackenberg, D. V. Edmonds, D. K. Matlock, F. C. Rizzo, K. D. Clarke, E. De Moor, Carbon partitioning to austenite from martensite or bainite during the quench and partition (Q&P) process: A critical assessment, Acta Mater., 56 (2008) 16-22.

[7] E. J. Seo, L. Cho, Y. Estrin, B. C. De Cooman, Microstructure-mechanical properties relationships for quenching and partitioning (Q&P) processed steel, Acta Mater., 113 (2016) 124-139.

[8] T. H. Man, T. Ohmura, Y. Tomota, Mechanical behavior of individual retained austenite grains in high carbon quenched-tempered steel, ISIJ Int., (2019) in press.

[9] A. Z. Hanzaki, P. D. Hodgson, S. Yue, Retained austenite characteristics in thermomechanically processed Si-Mn transformation-induced plasticity steels, Metall. Mater. Trans. A, 28 (1997) 2405-2414.

[10] D. Q. Bai, A. Di Chiro, S. Yue, Stability of retained austenite in a Nb microalloyed Mn-Si TRIP steel, Mater. Sci. Forum, 284-286 (1998) 253-262.

[11] P. J. Jacques, Q. Furnemont, F. Lani, T. Pardoen, F. Delannay, Multiscale mechanics of TRIP-assisted multiphase steels: I. Characterization and mechanical testing, Acta Mater., 55 (2007) 3681-3693.

[12] Y. Matsuoka, T. Iwasaki, N. Nakada, T. Tsuchiyama, S. Takaki, Effect of grain size on thermal and mechanical stability of austenite in metastable austenitic stainless steel, ISIJ Int., 53 (2013) 1224-1230.

[13] K. L. Johnson, Contact Mechanics, Cambridge University Press, (1985) 153-179.

[14] R. K. A. Al-Rub, G. Z. Voyiadjis, Analytical and experimental determination of the material intrinsic length scale of strain gradient plasticity theory from micro- and nano-indentation experiments, Int. J. of Plasticity, 20 (2004) 1139-1182.

[15] D. Kramer, H. Huang, M. Kriese, J. Robach, J. Nelson, A. Wright, D. Bahr, W. W. Gerberich, Yield strength predictions from the plastic zone around nanocontacts, Acta Mater., 47 (1999) 333-343.

[16] K. Durst, B. Backes, M. Goken, Indentation size effect in metallic materials: Correcting for the size of the plastic zone, Scripta Mater., 52 (2005) 1093-1097.

[17] C. L. Woodcock, D. F. Bahr, Plastic zone evolution around small scale indentations, Scripta Mater., 43 (2000) 783-788.

[18] K. Durst, B. Backs, O. Franke, M. Goken, Indentation size effect in metallic materials: Modeling strength from pop-in to macroscopic hardness using geometrically necessary dislocations, Acta Mater., 54 (2006) 2547-2555.

[19] K. Durst, B. Backes, M. Goken, Determination of plastic properties of polycrystalline metallic materials by nanoindentation-Experiments and finite element simulation, Mater. Res. Soc. Symp. Proc., 841 (2005) R1141-1146.

[20] K. W. Andrews, Empirical formulae for the calculation of some transformation temperatures, J. of the Iron and Steel Ins., 203 (1965) 721-727.

[21] W. C. Oliver, G. M. Pharr, An improved technique for determining hardness and

elastic modulus using load and displacement sensing indentation experiments, J. Mater. Res., 7 (1992) 6 1564-1583.

[22] L. Zhang, T. Ohmura, A. Shibata, K. Tsuzaki, Characterization of local deformation behavior of Fe-Ni lenticular martensite by nanoindentation, Mater. Sci. Eng. A 527 (2010) 1869-1874.

Chapter 4 Mechanical behavior of individual metastable retained austenite grains

4.1 Introduction

Steel must satisfy certain parameters relating to both strength and formability; however, a trade-off relationship exists between the two. Previous studies [1-6] have suggested that retained austenite transforms into martensite during the plastic deformation, resulting in high strength and large elongation caused by the transformation-induced plasticity (TRIP) effect which is influenced by the stability of austenite phase. In conclusion, the factors, such as the chemical composition, the grain size, the grain geometrical shape, the crystallographic orientation, and the phase surrounding austenite have the effect on the mechanical stability of retained austenite. The contents of elements, such as carbon, silicon, and aluminum, have been corroborated to affect the mechanical stability of retained austenite [7-11]. In addition, a study into the austenite grain morphology has suggested that the mechanical stability of retained austenite is higher for the lamellar microstructure than that for the equiaxed microstructure [12]. Furthermore, other studies [13-15] have reported that the surrounding microstructure influences the mechanical stability against the strain-induced martensitic transformation. In addition to these influential factors, the grain size is particularly important in determining the mechanical stability of retained austenite. The mechanical stability of retained austenite has been found to increases upon decreasing the grain size [16,17], while Matsuoka et al. [18] reported that the mechanical stability under tensile deformation is not influenced by grain size. In our study, the grain boundary has a constraint effect on the mechanical stability of the austenite phase in the Fe-27Ni. But, it is also important and necessary to investigate the mechanical stability of individual retained austenite dependent on grain size in iron-carbon steel. However, small grain sizes have prevented characterization using conventional analytical techniques.

In order to resolve this issue, nanoindentation technique is employed because of

their ability to probe at the nanometer scale [19-22]. Therefore, we herein combine nanoindentation with electron backscattered diffraction (EBSD) and transmission electron microscopy (TEM) for the analysis to study the mechanical stability of individual retained austenite grains. The P/h versus h plots, which are converted from the P versus h curves by nanoindentation, can be measured individually for the retained austenite regions, and the plastic deformation behaviors of the martensite regions are analyzed in addition to signs of stress-induced martensitic transformation. The mechanical behaviors of individual retained austenite grains with different size are investigated to understand the effect of grain size on stress-induced martensitic transformation.

4.2 Experimental procedures

The Fe-1.43C-12.21Cr-0.41Mn-0.19Si-0.42Ni mass% steel was employed herein, referred to Fe-1.4C-12Cr, to study the effect of grain size on mechanical stability of retained austenite in iron-high carbon steels. This steel was hot caliber-rolled to form a rod of 38 mm diameter [23]. The samples were austenitized at 1423 K for 0.6 ks followed by cooled to room temperature (293 K) and then tempered at 573 K for 5.4 ks under vacuum. The surface of samples was mechanically grinded, and then electrolytic polished with a solution of 8 vol% perchloric acid, 73 vol% ethyl alcohol, 10 vol% butyl cellosolve, and 9 vol% distilled water under a voltage of 50 V to remove the damaged layer. Sequential experiments were then carried out; the phase mapping of retained austenite and martensite was achieved using field emission scanning electron microscopy (FESEM) and EBSD, which was followed by nanoindentation tests for individual retained austenite and martensite regions in the mapped area. The positions of the indentation marks were then confirmed using FESEM and EBSD. Finally, the TEM observation on the cross-sectioned view of the microstructures underneath the indentation marks was carried out to identify the phases, where the TEM sample was milled by a focused ion beam (FIB). Here, the austenite grains tended to form triangular,

quadrangular, or polygonal shapes following the quenching and tempering process, and thus circumcircular diameters of the shapes were determined according to Heron's formula [24] and then used to represent the austenite grain size.

The microstructures were characterized using a JEOL JSM-7000F FESEM equipped with a TSL detector for EBSD mapping, which was operated at an accelerating voltage of 20 kV with a tilt angle of 70°. EBSD mapping was conducted using a scanning step size of 0.03 μm. Nanoindentation tests were carried out using a Hysitron TI 950 Triboindenter equipped with a Berkovich indenter, and the tip truncation is calibrated using a reference specimen of fused silica. All the tests were under a load-control condition with a constant loading and unloading rate of the indenter, set at 50 μN/s with a holding segment of 10 s. The Oliver and Pharr method [25] was performed to analyses for the tip calibration and the hardness calculations. The probed sites and the indenter configurations on the sample surfaces were observed by scanning probe microscopy (SPM) before and after the nanoindentation tests. A JEOL JEM-4000 FIB with bulk-specimen and TEM-compatible holders is employed for TEM observations, operated at 5 kV, 10 kV, and 30 kV accelerating voltage, respectively. To avoid damage to the indentation mark area, the surface containing the indentation marks was protected by carbon deposition during FIB milling. In order to view the cross-section of the indentation mark, the sliced sample was fixed to a nano mesh in such a way after lift-out. The TEM sample was then thinned from both sides to give a thickness of ~100 nm, which guaranteed its transparency to the electron beam for imaging. TEM observations were performed using a JEOL JEM-2100, operated at 200 kV.

4.3 Results

4.3.1 Mechanical behaviors of the individual retained austenite and martensite

The microstructure of the sample consists of retained austenite, martensite, and carbide, which are represented by the red, yellow, and green segments, respectively, as shown in a phase map of Fig. 4.1(a), where the black points indicate the points of measurement failure (confidence index < 0.2). Besides, the indentation marks on the martensite are indicated by the dashed circles, as confirmed by the IQ map and the SPM image shown in Figs. 4.1(b) and 4.1(c), respectively. Similarly, the indentation mark positions on the austenite phase are shown in Figs. 4.1(d), 4.1(e) and 4.1(f).

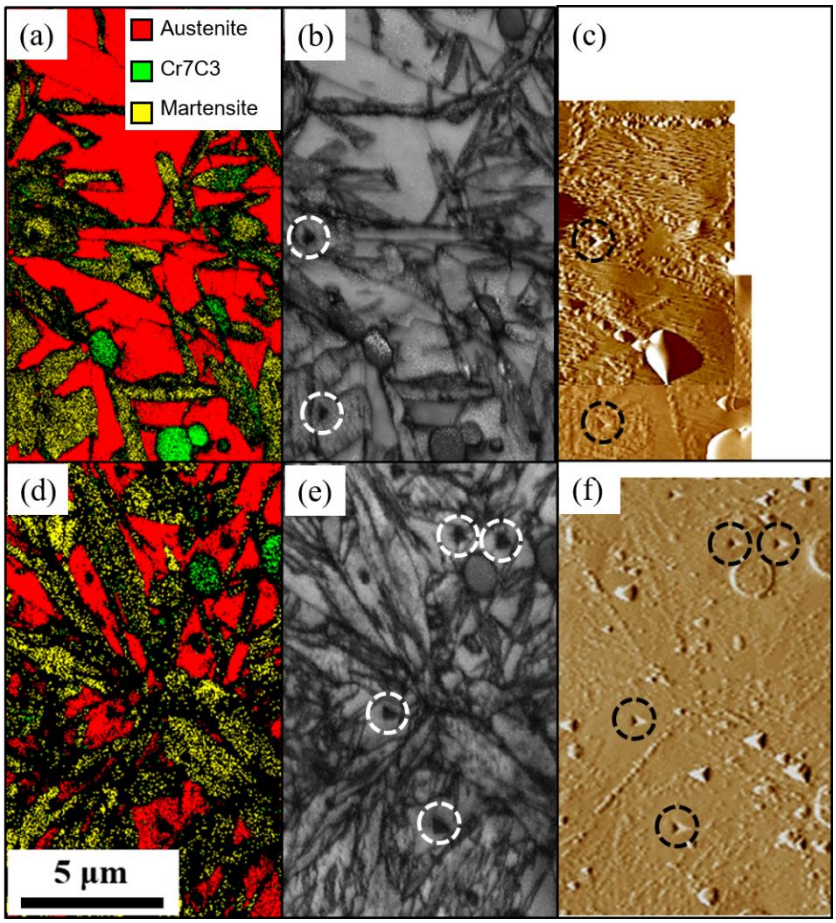

Figure 4.1 (a), (d) Phase maps, (b), (e) IQ maps and (c), (f) SPM images of the sample surface after nanoindentation measurements showing indentation mark positions by dashed circles in the martensite regions on (a)-(c) and retained austenite regions on (d)-(f).

Figure 4.2 demonstrates the typical results of the *P* versus *h* curves which were obtained individually for the martensite and retained austenite phases through nanoindentation tests with a peak load of 1000 μN. The elastic deformation region at the initial stage of the loading curve is identified by fitting with the Hertz contact theory [26], and thus the relationship between *P* and *h* during the pure elastic deformation is given by Eq. (2.2) and (2.3). When a load-displacement data deviates from the Hertz fit curve as shown by the blue dashed circle in Fig. 4.2, it is considered to mark as the initiation of plastic deformation [21,27]. It is found that the nanohardness calculated from the unloading curve is significantly higher for the martensite than that for the retained austenite.

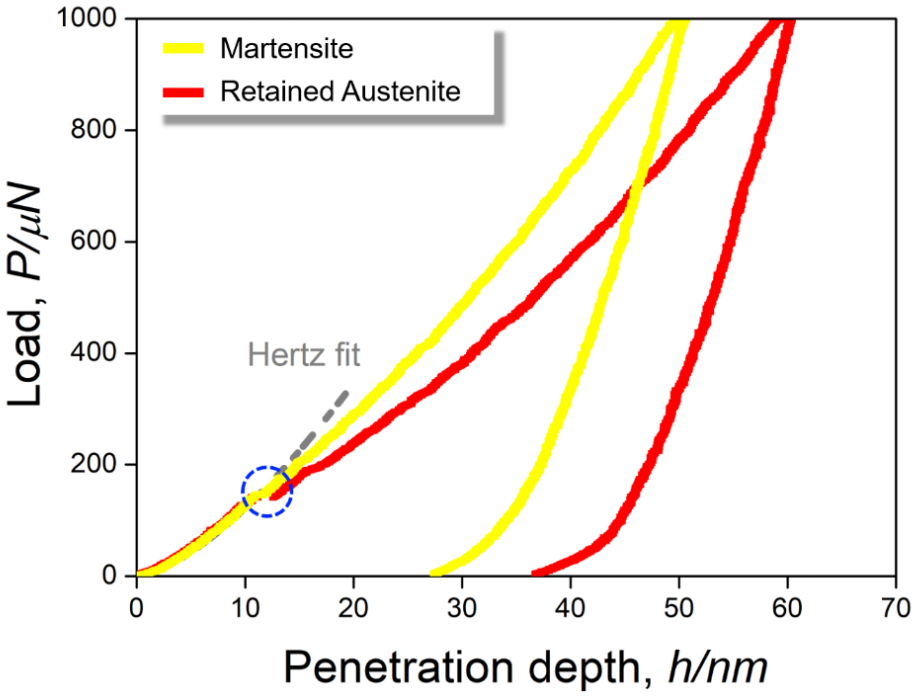

Figure 4.2 Typical load (*P*) versus penetration depth (*h*) curves for the martensite (yellow) and retained austenite phase (red).

The loading segment of *P/h* versus *h* plots converted from Fig. 4.2 are therefore depicted in Figs. 4.3(a) and 4.3(b) for the martensite and retained austenite phases, respectively, using the new evaluation method as described in section 2.3.1. As shown, the slope *a* for the martensite maintains relatively constant, thereby suggesting a single

deformation mode during the plastic deformation. Whereas, for the retained austenite, an anomaly is observed in the middle of the loading segment at $h \sim 35$ nm, which is defined as P_t (see an arrow in Fig. 4.3(b)), and it suggests double stages with a lower a value in stage I and a higher a value in stage II. It should be noted that the slope in stage II of the retained austenite (0.143 μN/nm^2) is relatively close to that of the martensite (0.194 μN/nm^2). The b values in Figs. 4.3(a) and 4.3(b) were estimated to be comparable, therefore, confirming that the accuracy of both the data and the analysis method are reasonable.

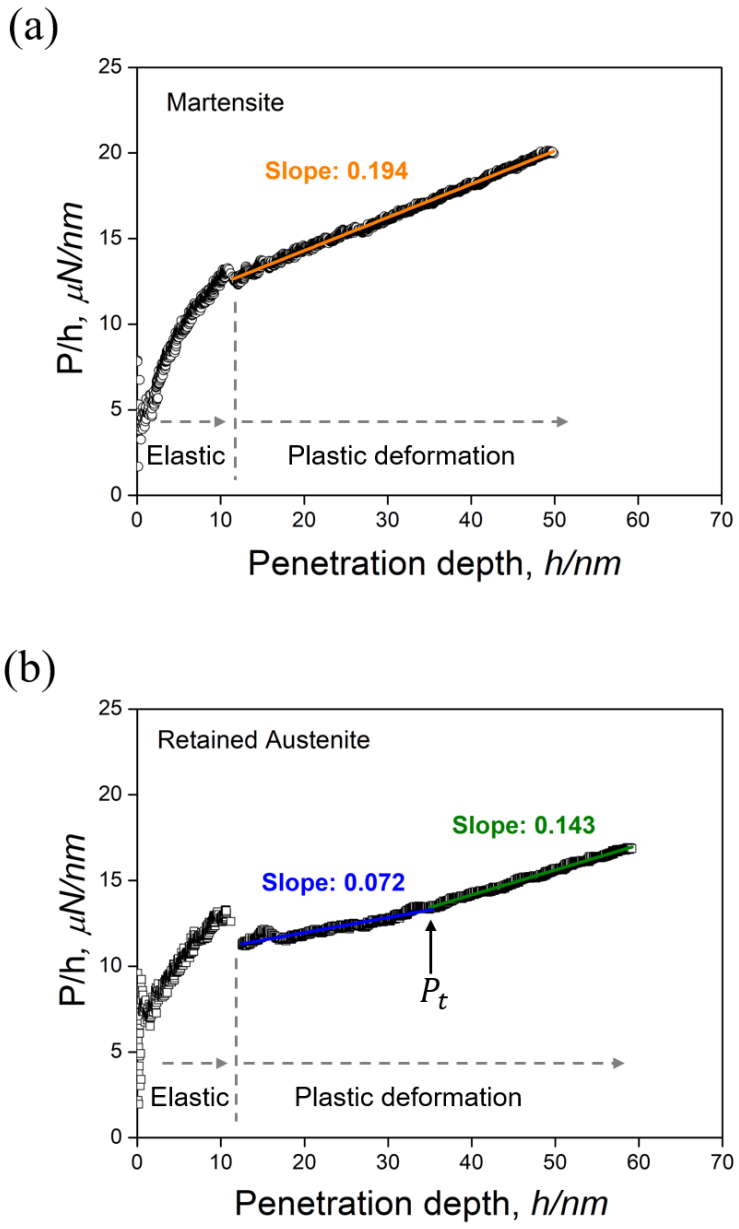

Figure 4.3 The *P/h* versus *h* plots for (a) the martensite and (b) the retained austenite.

It is shown in chapter 3 that the metastable austenite in the Fe-27Ni steel exhibits the double stage deformation, where the stage I with the low flow stress is dominated by stress-induced martensitic transformation and stage II with higher flow stress is governed by a dislocation glide motion in the transformed martensite. Furthermore, the martensite shows a single stage deformation, which is corresponding to dislocation movement mode. The nanoindentation results for the retained austenite and martensite in the Fe-1.4C-12Cr sample are in agreement with the results in the Fe-27Ni samples.

4.3.2 TEM observation of the microstructures underneath the indentation mark

The phase map and the SEM image of the austenite grain, which was subsequently employed for TEM observations of the microstructures below the indentation mark, are indicated in Figs. 4.4(a) and 4.4(b), respectively. It was confirmed that the indentation mark was penetrated inside the austenite grain (outlined by the dashed triangles), which was surrounded by the tempered martensite. The corresponding *P* versus *h* curve and converted *P/h* versus *h* plot obtained during the nanoindentation test with a peak load of 600 μN are shown in Figs. 4.4(c) and 4.4(d), respectively. Figure 4.4(d) shows that the loading segment of *P/h* versus *h* plot of the austenite grain also exhibited a change in the slope and double stages during the plastic deformation.

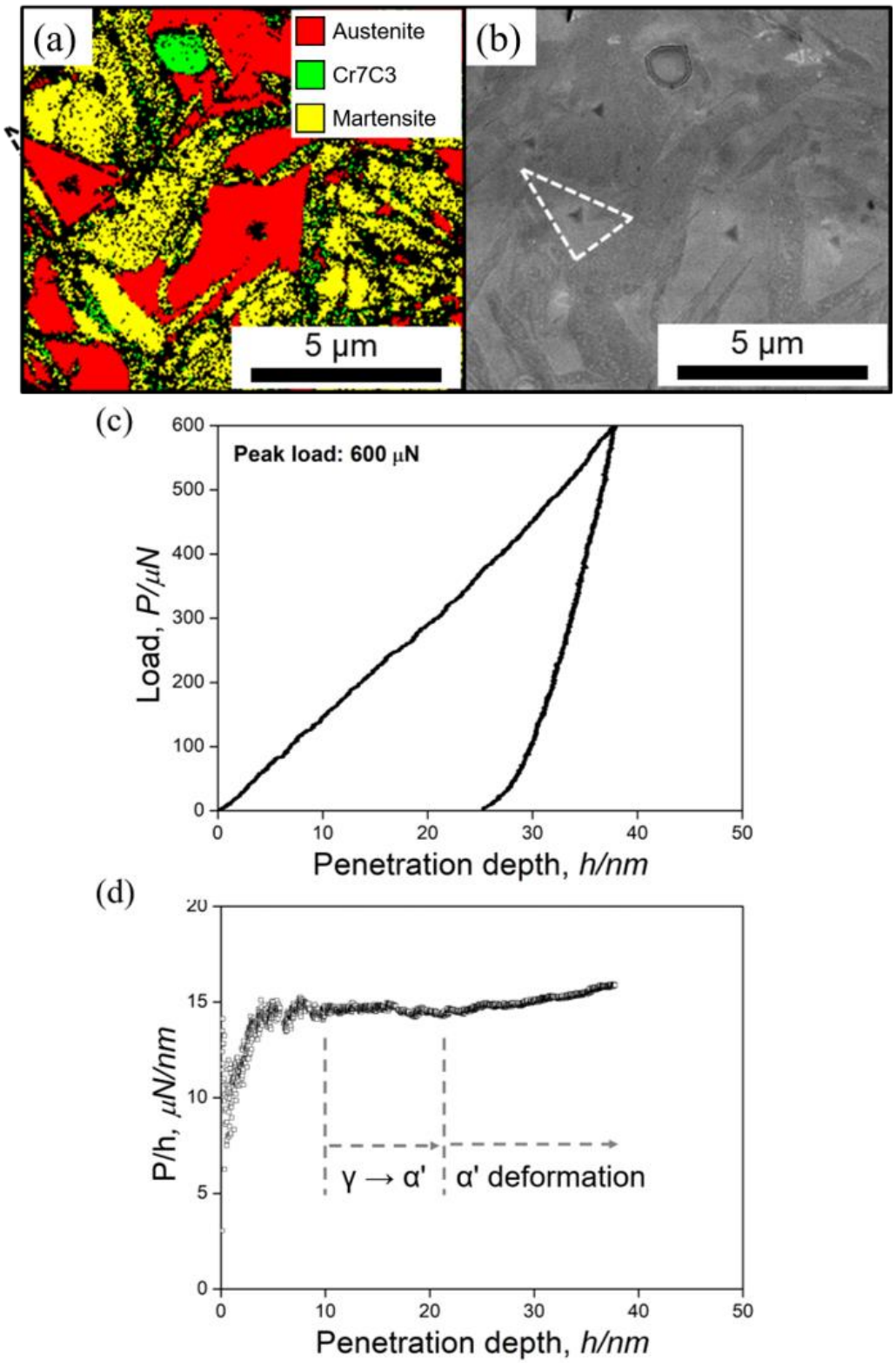

Figure 4.4 (a) Phase map and (b) SEM image of the sample surface showing an indentation mark on a retained austenite grain outlined by the dashed triangle, which was subsequently employed for TEM observations of the microstructures below the indentation mark in a cross-sectional view. (c) The corresponding *P* versus *h* curve and (d) loading segment of *P/h* versus *h* plot for the indentation mark.

Figure 4.5(a) exhibits a TEM BF image of a cross-sectional view of the microstructure below the indentation mark as presented in Fig. 4.4, where the retained austenite grain surrounded by the tempered martensite is observed. Figures 4.5(b) and 4.5(c) show DF images with SAED patterns corresponding to the region in the dashed square of Fig. 4.5(a), where parts 4.5(b) and 4.5(c) correspond to the selected regions of the white dashed circles 1 and 2 in Fig. 4.5(a), respectively. The SAED patterns taken respectively from the selected regions 1 and 2 suggest that the lattice structures are composed of the indentation-transformed martensite (transformed α' that is bct according to X-ray diffraction for the present steel [23] but regarded as bcc in this TEM analysis) and the original retained austenite (γ that is fcc), respectively. Dislocations are observed in the transformed martensite region. The DF image in Fig. 4.5(c) indicates that little retained austenite is also maintained in the transformed martensite region due to inhomogeneous formation of the transformed martensite underneath the indentation mark. Accordingly, the horizontal sharp line (indicated by a white arrow in Fig. 4.5(a)) with bcc {110} trace in the transformed martensite region can be considered as the habit plane [28]. However, the internal stresses at the interface between austenite and martensite are partially relaxed first by twinning at the mid-rib region and also through dislocations. Such a stress relaxation event renders the interface orientation different from the habit plane, and so the determination of the habit plane orientation is challenging. Figure 4.5(d) shows a schematic illustration of the cross-sectional view on the microstructure underneath the indentation mark, which is accord with the frame of Fig. 4.5(a).

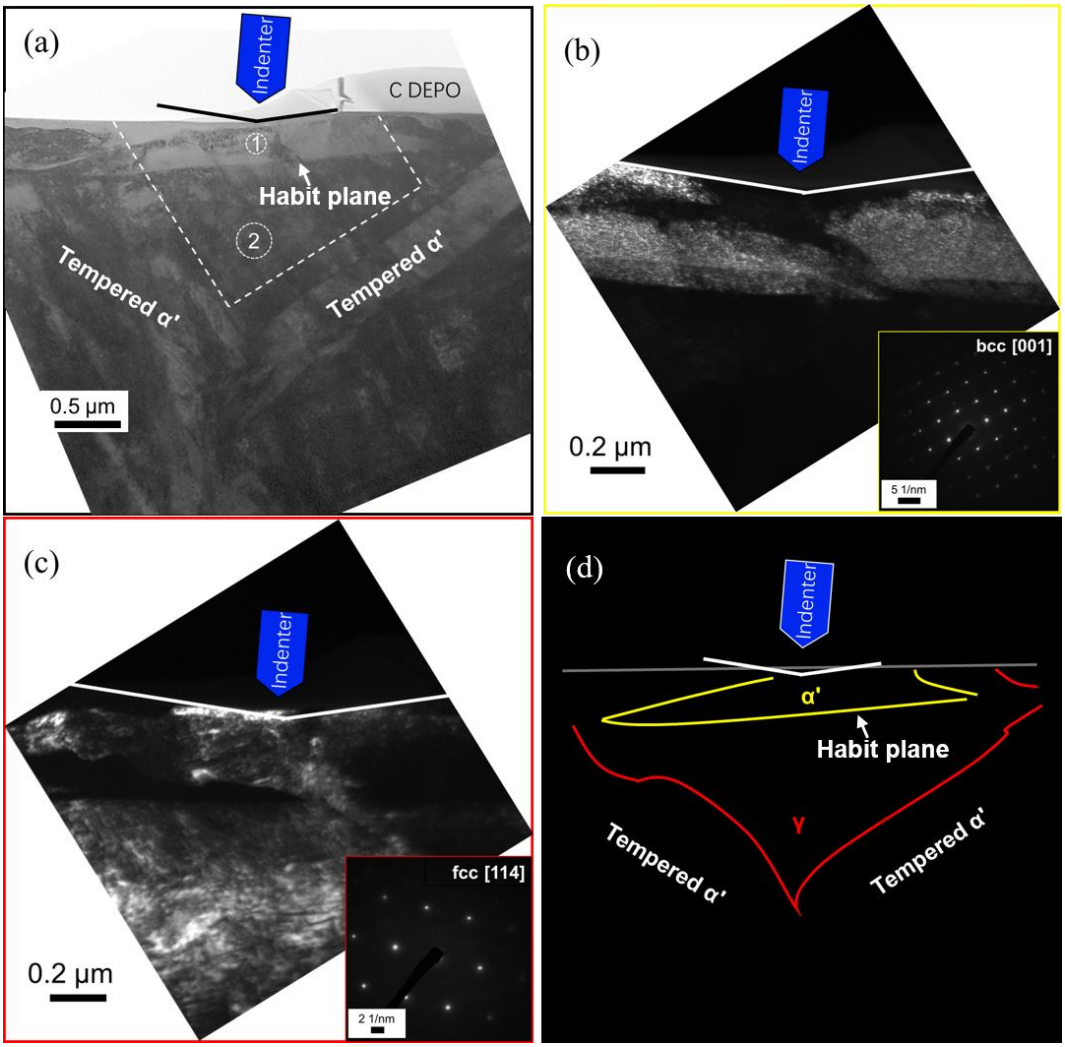

Figure 4.5 (a) TEM BF image of a cross-sectional view of the microstructure below the indentation mark showing the retained austenite grain surrounded by the tempered martensite. (b) and (c) DF images corresponding to the region outlined by the dashed square of (a), where parts (b) and (c) correspond to the selected regions of the dashed-circle 1 and 2 in (a), respectively. The corresponding SAED patterns are shown as inserts. (d) Schematic illustration showing a cross-sectional view of the microstructure below the indentation mark, which is coincident with the frame of (a).

4.3.3 Effect of grain size on the retained austenite mechanical stability

The phase maps and SPM images in Fig. 4.6 show that the indentation marks are settled inside three different sized austenite grains outlined by the dashed lines (1.55 μm, 2.76 μm, 5.38 μm), which are taken after nanoindentation tests with a peak load of 1000 μN.

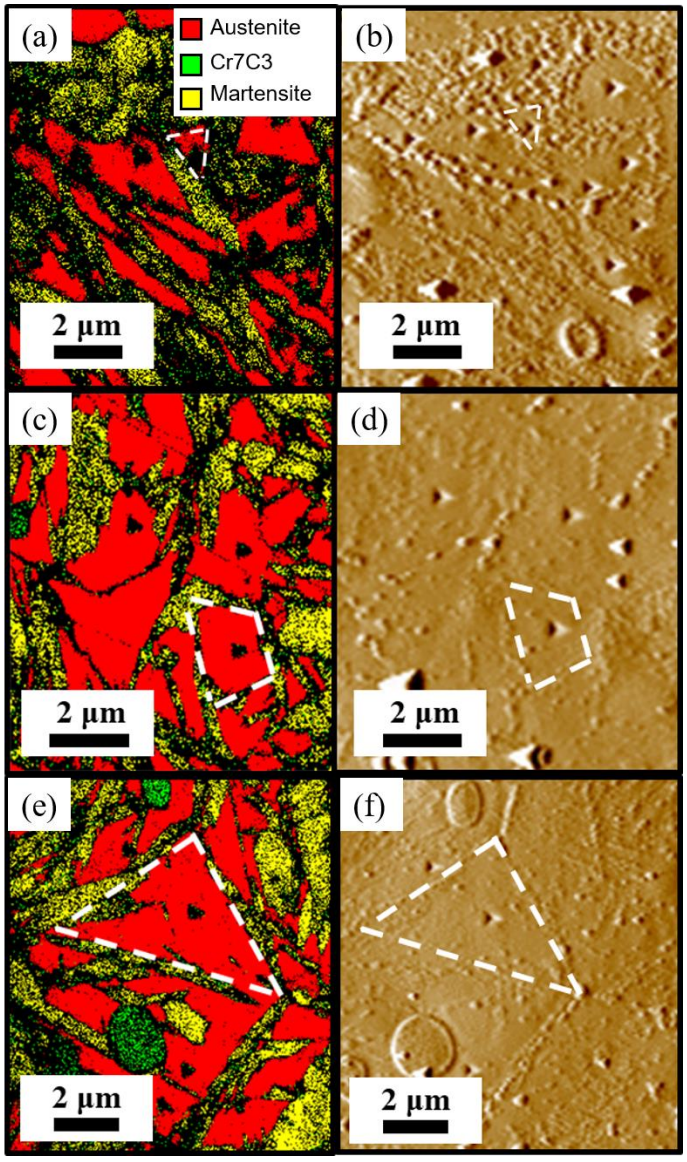

Figure 4.6 (a) Phase map and (b) SPM image showing the indentation mark inside retained austenite grain with a smaller size of 1.55 μm, (c), (d) a middle size of 2.76 μm, and (e), (f) a larger size of 5.38 μm respectively outlined by the dashed lines.

The corresponding loading segment of *P/h* versus *h* plots for the three grains with different sizes are indicated in Fig. 4.7. Interestingly, all *P/h* versus *h* plots for the three austenite grains show double stages during the plastic deformation, *i.e.*, a low value for the slope *a* in stage I, and a higher value in stage II. Besides, the stage I is longer and its slope *a* is higher for the small grains. Furthermore, the transition load P_t, which is determined by the change in the slope of the *P/h* versus *h* plot, was found to increase upon decreasing the austenite grain size. Indeed, the slope *a* in stage I is lower, and the P_t value is relatively clear for a large austenite grain. On the contrary, the *a* is larger in stage I, and it is relatively difficult to determine the P_t, for a small austenite grain.

For a reliable conclusion, the nanoindentation tests were repeated for 76 austenite grains with different sizes. Figs. 4.8(a) and 4.8(b) are the plots of the slope *a* in stage I and the P_t value, respectively, as a function of the austenite grain size *D*. As indicated, upon increasing the austenite grain size, both the slope *a* in stage I and the P_t value are decreased. Although some data show scattering due to the irregular shapes of the austenite grains, it was concluded that larger grain sizes gave a lower resistance to plastic deformation.

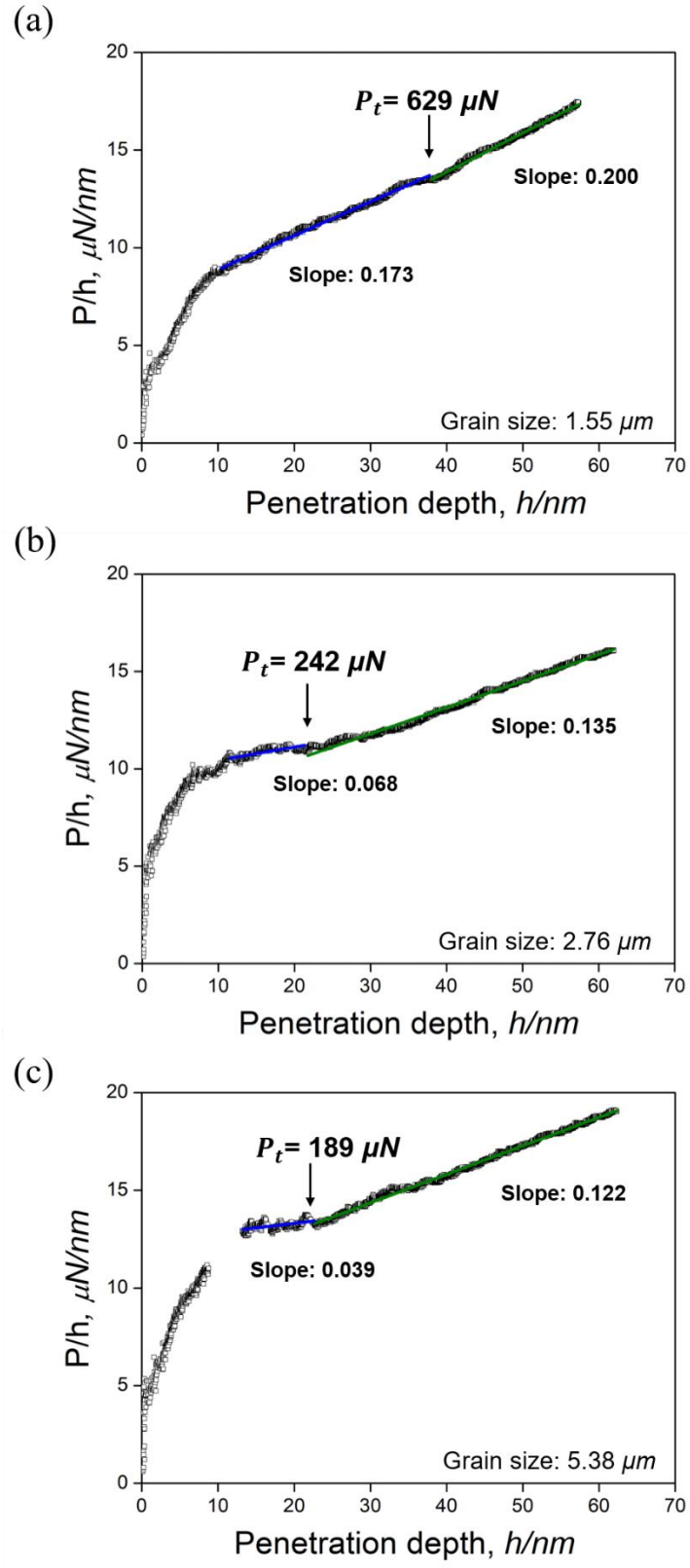

Figure 4.7 The loading segment of *P/h* versus *h* plots corresponding to the three grains with sizes of (a) 1.55 µm, (b) 2.76 µm, (c) 5.38 µm shown in Fig. 5.6. All the plots exhibit the two stages of I (blue) and II (green).

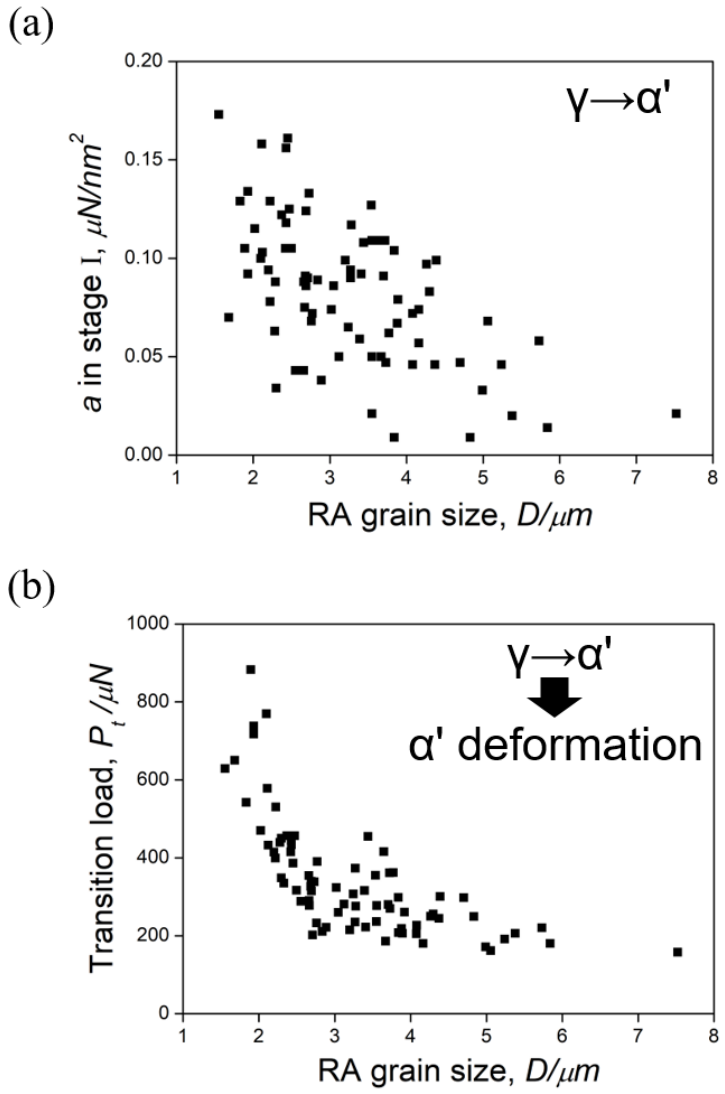

Figure 4.8 (a) The slope *a* in stage I and (b) the transition load P_t plotted as a function of the grain size *D* of the retained austenite phase.

4.4 Discussion

For the plastic deformation of retained austenite in the Fe-1.4C-12Cr, it is found that a change in the slope *a* of the *P/h* versus *h* plot is considered to be the consequence of a change in the deformation mode, corresponding to the stress-induced martensitic transformation of the metastable retained austenite to the dislocation motion in the transformed martensite. Many studies [21, 22, 27, 29-31] have been published that the first pop-in behavior is related to the dislocation nucleation. In the austenite phase, the first pop-in behavior is presumably corresponding to the dislocation nucleation rather than martensitic transformation because there is a high-stress zone underneath the indenter, which may inhibit a martensitic transformation with volume expansion. Therefore, the right before or quite an initial region in stage I might include dislocation deformation in the austenite phase. These two mechanisms must possibly take place competitively to relax the external stresses. From the present experimental results, it is believed that martensitic transformation occurred in stage I, but the intrusion of dislocation movement in austenite could not be denied. Furthermore, as well known, the appearance of the transformed martensite contributes to work hardening (hardening effect). Moreover, the *a* value in stage II is relatively close to that of the tempered martensite. It suggests that the stage II is hardening effect and compliance with the dislocation glide motion in the transformed martensite. This was presumed based on nanoindentation behavior measurements and the microstructural characterizations. Figure 4.9 shows a schematic illustration of the cross-sectional view of the deformation behavior during the indentation process for a retained austenite grain surrounded by the tempered martensite. As shown, in stage I, stress-induced martensitic transformation starts to take place, and the fresh martensite transformed by nanoindentation is extended from the free surface as the applied load *P* is increased. As a stress distribution exists below the indenter, the value of P_t is presumably dominated by a balance between the stress at the γ/α' interface and the stress immediately below the indenter for slip deformation in the transformed martensite. If the transformation at the interface is easier than the deformation in the transformed martensite, the martensitic transformation is

dominant. On further indentation, the stress immediately below the indenter increases, while the transformation stress at the interface is maintained. When the stress in the indentation-transformed martensite reaches a value high enough to deform the phase, the austenite to martensitic transformation reaches completion, which relates to the transition point P_t. Following P_t in stage II, the dominant deformation mode is change to slip deformation of the fresh martensite that transformed from the austenite phase in stage I. These results allow us to conclude that the *P/h* versus *h* plot for the retained austenite phase therefore confirms double plastic deformation stages, where stage I is dominated by stress-induced martensitic transformation and stage II is governed by slip deformation of the transformed martensite. This conclusion is in agreement with the TEM results, which confirmed the presence of the bcc (or bct) phase underneath the indentation mark.

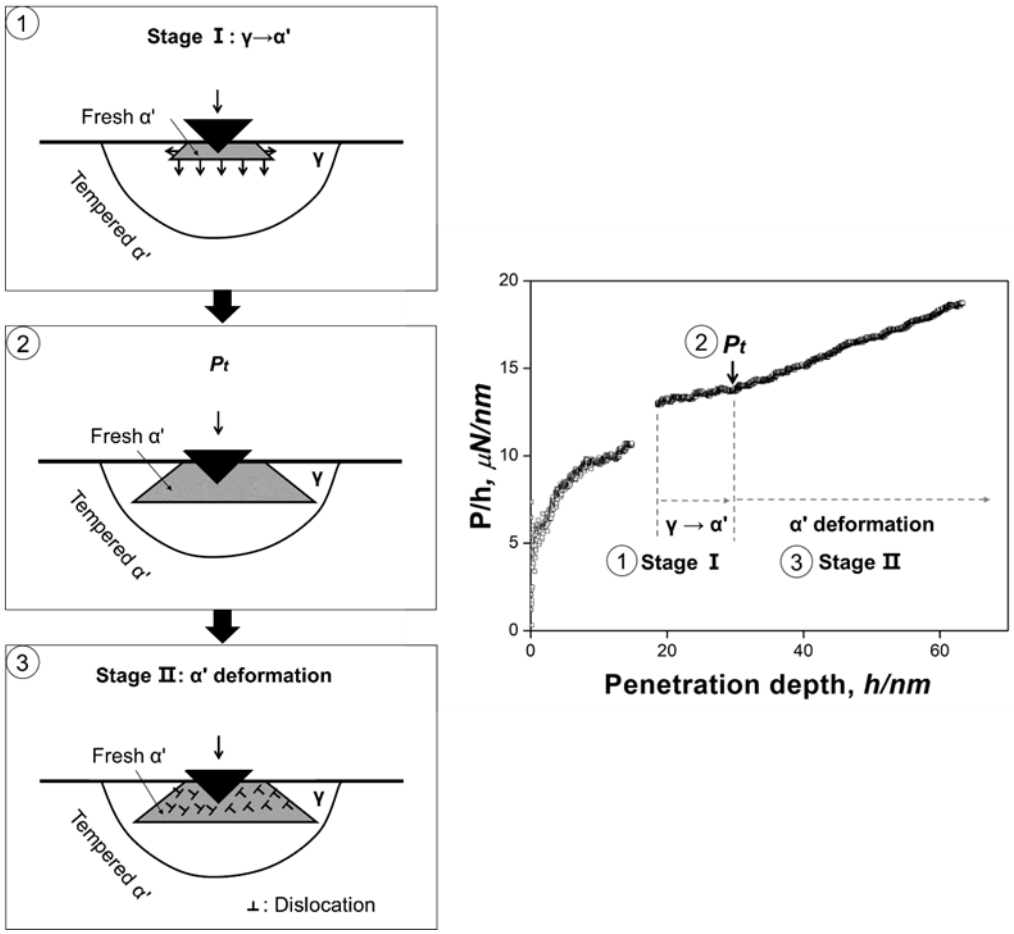

Figure 4.9 Schematic illustration of the cross-sectional view of the deformation behavior during indentation for a retained austenite grain surrounded by a tempered martensite combined with a loading segment of *P/h* versus *h* plot.

The nanoindentation results from all the grains show that both the slope *a* in stage I and the value of P_t increase with decreasing the austenite grain size, which indicates that mechanical stability of the retained austenite increases with decreasing in grain size. This suggests that the resistance against stress-induced martensitic transformation becomes higher in smaller-grained austenite. This could be attributed partly to a constraint by the surrounding tempered martensite. Since the tempered martensite is harder than the retained austenite phase as shown in Fig. 4.2, the austenite to martensitic transformation with volume expansion should be inhibited by the tempered martensite. This effect is more significant in a region close to the γ/α' interface as the volume expansion resulting from the martensitic transformation is subject to greater compressive stresses and space limitations from the interface in a smaller austenite grain. It is noted that the start of stage I in all grains generally occurs at an indentation depth of about 10 nm right after an onset of plasticity, in which the size of plastic zone reaches 100 nm in diameter of hemispherical approximation. The plastic zone with a size of 100 nm is much smaller than the smallest grain size of 1.5 μm. However, the elastic zone is much larger than the plastic zone and presumably affected by the grain boundary. The distribution of the compression stress underneath the indenter is inversely proportional to the depth from the load point, which is calculated based on the Hertz model. The stress does not reach zero even though the depth approaches infinite, so that all the grain boundary conditions are affected. It suggests that the grain boundary influences the stress at which the stress-induced martensitic transformation starts. Therefore, the mechanical stability of austenite depends on the grain size even at the start of stress-induced martensitic transformation [26]. Furthermore, the higher resistance against stress-induced martensitic transformation could also be explained by the microstructures present in the austenite phase close to the interface. More specifically, carbon atoms can diffuse into the austenite phase from the surrounding martensite during tempering, and so the carbon concentration is presumably higher in the vicinity of the interface. In addition, any dislocations would be locked by the carbon atoms during tempering due to the relatively low tempering temperature employed [32-34]. As such, the area close to the γ/α' interface of the present sample is speculated to

contain a high dislocation density in addition to carbon enrichment. It should be noted that the dislocations locked by carbon atoms hinder the stress-induced martensitic transformation. Furthermore, assuming that the thickness of such an interface layer is relatively constant, the finer austenite grains should become more stable compared to the coarser grains.

As shown in Figs. 4.8(a) and 4.8(b), the scatter diagrams may also suggest that additional influential factors exist in the Fe-1.4C-12Cr sample examined herein. More specifically, internal stresses are induced upon quenching due to transformation strains, and high local internal stresses should be partially relaxed by the generation of dislocations in the retained austenite phase. Besides, the internal stresses and dislocation density are believed to be higher in the vicinity of the γ/α' interface. Concerning the transformation internal stress distribution, many studies have discussed this factor [35-37]; however, it is expected only to impart a minor influence in this case, as the sample was tempered and the examination was carried out on the surface layer.

4.5 Conclusions

The deformation behaviors of the metastable retained austenite and tempered martensite in the Fe-1.4C-12Cr steel were investigated by the combination of nanoindentation tests and microstructural observations based on SEM/EBSD and TEM. More specifically, the effect of the austenite grain size on its mechanical stability was determined.

(1) In the *P/h* versus *h* plots obtained by nanoindentation, the martensite was found to exhibit a single plastic deformation stage during the loading process, on the contrary, the retained austenite phase showed double stages, with a lower flow stress in stage I, which is dominated by stress-induced martensitic transformation, and a higher flow stress in stage II, which is governed by a dislocation glide motion in the transformed martensite.

(2) The TEM results demonstrated that the transformed martensite existed immediately underneath the indentation mark inside the retained austenite grain, which is confirmed the results of the nanoindentation behavior.

(3) Fine retained austenite grains exhibited higher flow stress in stage I with a higher transition load P_t, which indicates that the mechanical stability of retained austenite increases with decreasing in grain size.

References

[1] B. C. De Cooman, Structure-properties relationship in TRIP steels containing carbide-free bainite, Curr. Opin. Solid State Mater. Sci., 8 (2004) 285-303.

[2] H. Aydin, E. Essadiqi, I. Jung, S. Yue, Development of 3rd generation AHSS with medium Mn content alloying compositions, Mater. Sci. Eng. A, 564 (2013) 501-508.

[3] W. Q. Cao, C. Wang, J. Shi, M. Q. Wang, W. J. Hui, H. Dong, Microstructure and mechanical properties of Fe-0.2C-5Mn steel processed by ART-annealing, Mater. Sci. Eng. A, 528 (2011) 6661-6666.

[4] S. Zaefferer, J. Ohlert, W. Bleck, A study of microstructure, transformation mechanisms and correlation between microstructure and mechanical properties of a low alloyed TRIP steel, Acta Mater., 52 (2004) 2765-2778.

[5] P. J. Jacques, Transformation-induced plasticity for high strength formable steels, Curr. Opin. Solid State Mater. Sci., 8 (2004) 259-265.

[6] V. F. Zackay, E. R. Parker, D. Fahr, R. Busch, The enhancement of ductility in high-strength steels, Trans. ASM, 60 (1967) 252-259.

[7] R. Blonde, E. Jimenez-Melero, L. Zhao, J. P. Wright, E. Bruck, S. V. D. Zwaag, N. H. V. Dijk, High-energy X-ray diffraction study on the temperature-dependent mechanical stability of retained austenite in low-alloyed TRIP steels, Acta Mater.,

60 (2012) 565-577.

[8] M. De Meyer, D. Vanderschueren, B. C. De Cooman, The influence of the substitution of Si by Al on the properties of cold rolled C-Mn-Si TRIP steels, ISIJ Int., 39 (1999) 813-822.

[9] J. Wang, S. V. D. Zwaag, Stabilization mechanisms of retained austenite in transformation-induced plasticity steel, Metall. Mater. Trans. A, 32 (2001) 1527-1539.

[10] J. Tobata, K. L. Ngo-Huynh, N. Nakada, T. Tsuchiyama, S. Takaki, Role of silicon in quenching and partitioning treatment of low-carbon martensitic stainless steel, ISIJ Int., 52 (2012) 1377-1382.

[11] K. Sugimoto, B. Yu, Y. Mukai, S. Ikeda, Microstructure and formability of aluminum bearing TRIP-aided steels with annealed martensite matrix, ISIJ Int., 45 (2005) 1194-1200.

[12] J. Chiang, J. D. Boyd, A. K. Pilkey, Effect of microstructure on retained austenite stability and tensile behavior in an aluminum-alloyed TRIP steel, Mater. Sci. Eng. A, 638 (2015) 132-142.

[13] K. Sugimoto, A. Kanda, R. Kikuchi, S. Hashimoto, T. Kashima, S. Ikeda, Ductility and formability of newly developed high strength low alloy TRIP-aided sheet steels with annealed martensite matrix, ISIJ Int., 42 (2002) 910-915.

[14] S. Cheng, X. Wang, Z. Feng, B. Clausen, H. Choo, P. K. Liaw, Probing the characteristic deformation behaviors of transformation-induced plasticity steels, Metall. Mater. Trans. A, 39 (2008) 3105-3112.

[15] J. H. Ryu, D. Kim, H. S. Kim, H. K. D. H. Bhadeshia, D. W. Suh, Strain partitioning and mechanical stability of retained austenite, Scripta Mater., 63 (2010) 297-299.

[16] P. J. Jacques, Q. Furnemont, F. Lani, T. Pardoen, F. Delannay, Multiscale mechanics of TRIP-assisted multiphase steels: I. Characterization and mechanical testing, Acta Mater., 55 (2007) 3681-3693.

[17] D. Q. Bai, A. Di Chiro, S. Yue, Stability of retained austenite in a Nb microalloyed Mn-Si TRIP steel, Mater. Sci. Forum, 284-286 (1998) 253-262.

[18] Y. Matsuoka, T. Iwasaki, N. Nakada, T. Tsuchiyama, S. Takaki, Effect of grain size on thermal and mechanical stability of austenite in metastable austenitic stainless steel, ISIJ Int., 53 (2013) 1224-1230.

[19] T. Ohmura, K. Tsuzaki, S. Matsuoka, Nanohardness measurement of high-purity Fe-C martensite, Scripta Mater., 45 (2001) 889-894.

[20] K. Sekido, T. Ohmura, L. Zhang, T. Hara, K. Tsuzaki, The effect of interstitial carbon on the initiation of plastic deformation of steels, Mater. Sci. Eng. A, 530 (2011) 396-401.

[21] L. Zhang, T. Ohmura, Plasticity initiation and evolution during nanoindentation of an iron-3% silicon crystal, Phys. Rev. Lett., 112 (2014) 145504.

[22] T. Ohmura, L. Zhang, K. Sekido, K. Tsuzaki, Effects of lattice defects on indentation-induced plasticity initiation behavior in metals, J. Mater. Res., 27 (2012) 13 1742-1749.

[23] S. He, Y. Tomota, Y. H. Su, W. Gong, S. Harjo, Z. Zhao, Unusual tempering behavior of Fe-Cr-C martensite, ISIJ Int., 55 (2015) 686-690.

[24] W. Dunham, Journey through Genius: The Great Theorems of Mathematics, Wiley, New York, (1990) 113-132.

[25] W. C. Oliver, G. M. Pharr, An improved technique for determining hardness and elastic modulus using load and displacement sensing indentation experiments, J. Mater. Res., 7 (1992) 6 1564-1583.

[26] K. L. Jonson, Contact Mechanics, Cambridge University Press, Cambridge, (1985) 84-106.

[27] A. Gouldstone, N. Chollacoop, M. Dao, J. Li, A. M. Minor, Y.-L. Shen, Indentation across size scales and disciplines: Recent developments in experimentation and

modeling, Acta Mater., 55 (2007) 4015-4039.

[28] A. Kelly, G. W. Groves, P. Kidd, Crystallography and Crystal Defects, Revised Edition, John Wiley & Sons, New York, (2000) 69.

[29] W. W. Gerberich, J. C. Nelson, E. T. Lilleodden, P. Anderson, J. T. Wyrobek, Indentation induced dislocation nucleation: The initial yield point, Acta Mater., 44 (1996) 3585-3598.

[30] T. Ohmura, K. Tsuzaki, F. Yin, Nanoindentation-induced deformation behavior in the vicinity of single grain boundary of interstitial-free steel, Mater. Trans., 46 (2005) 2026-2019.

[31] T. H. Ahn, C. S. Oh, D. H. Kim, K. H. Oh, H. Bei, E. P. George, H. N. Han, Investigation of strain-induced martensitic transformation in metastable austenite using nanoindentation, Scripta Mater., 63 (2010) 540-543.

[32] A. J. Clarke, J. G. Speer, M. K. Miller, R. E. Hackenberg, D. V. Edmonds, D. K. Matlock, F. C. Rizzo, K. D. Clarke, E. De Moor, Carbon partitioning to austenite from martensite or bainite during the quench and partition (Q&P) process: A critical assessment, Acta Mater., 56 (2008) 16-22.

[33] J. Speer, D. K. Matlock, B. C. De Cooman, J. G. Schroth, Carbon partitioning into austenite after martensite transformation, Acta Mater., 51 (2003) 2611-2622.

[34] E. J. Seo, L. Cho, Y. Estrin, B. C. De Cooman, Microstructure-mechanical properties relationships for quenching and partitioning (Q&P) processed steel, Acta Mater., 113 (2016) 124-139.

[35] M. Villa, F. B. Grumsen, K. Pantleon, M. A. J. Somers, Martensitic transformation and stress partitioning in a high-carbon steel, Scripta Mater., 67 (2012) 621-624.

[36] M. Villa, F. Niessen, M.A.J. Somers, *In situ* investigation of the evolution of lattice strain and stresses in austenite and martensite during quenching and tempering of steel, Metall. Mater. Trans. A, 49 (2018) 28-40.

[37] N. Nakada, Y. Ishibashi, T. Tsuchiyama and S. Takaki, Self-stabilization of untransformed austenite by hydrostatic pressure via martensitic transformation, Acta Mater., 110(2016), 95.

Chapter 5 Summary and conclusion

The primary objective of this study is the investigations of nanoindentation behaviors for single phases, such as metastable austenite, stable austenite, ferrite, and tempered martensite, as well as the mechanical stability of metastable austenite phase dependent on grain size and the understanding of the deformation modes.

An effective and powerful analytical method is proposed to characterize the mechanical behaviors of materials using the slope a of the derived P/h versus h plot obtained from a measured P versus h curve in chapter 2. The three typical microstructures in the Fe alloys, such as austenite, ferrite, and tempered martensite, were carried out to investigate the deformation behaviors to estimate the relationship between the slope a of the P/h versus h plot and the nanohardness H_n. The nanoindentation results suggest that the slope a increases proportionally as the nanohardness H_n, which is strongly affected by the deformation mechanisms.

The nanoindentation behaviors of metastable austenite, stable austenite, and martensite are investigated in the Fe-Ni steels. Also, the effect of grain boundary on the mechanical stability of metastable austenite in the Fe-27Ni steel is shown in chapter 3. The results of the P/h versus h plots suggest that the stable austenite and martensite exhibit a single plastic deformation stage, while the metastable austenite shows double stages, of the stress-induced martensitic transformation in stage I and dislocation glide motion in the transformed martensite in stage II. Besides, the nanoindentation results suggest that the austenite grain boundary and the γ/α' interface hold a higher slope a value in stage I with a higher transition load P_t than the austenite grain interior. Moreover, the transition load P_t increases inversely as the distance of the indentation mark from the austenite grain boundary, which indicates that the grain boundary strongly suppresses the martensitic transformation improving the mechanical stability of metastable austenite. TEM observations clearly show the presence of the indentation-transformed martensite underneath the indentation mark in the austenite grains, which corroborates that the dominant deformation mode in stage I is martensitic transformation. No martensite in the neighboring grain indicates the constraint by grain

boundary against stress-induced martensitic transformation, which is in concordance with the result of nanoindentation behaviors.

The nanoindentation behaviors and the microstructural characterizations of the metastable retained austenite and the tempered martensite are studied in the Fe-1.4C-12Cr steel. The effect of the retained austenite grain size on the mechanical stability is also determined in chapter 4. It is found that the martensite exhibits a single plastic deformation stage in the *P/h* versus *h* plot, whereas the retained austenite phase shows double stages that include martensitic transformation in stage I and dislocation glide motion in the transformed martensite in stage II, which is in agreement with the results of the metastable austenite in the Fe-27Ni steel. The TEM results also confirmed the presence of the transformed martensite underneath the indentation mark inside the retained austenite grain. The nanoindentation data show that the retained austenite with fine grains exhibit higher slope *a* value in stage I with a higher transition load P_t, which suggests that the mechanical stability increases with decreasing in austenite grain size.